OllscoilnahÉireann, Corcaigh

NATIONAL UNIVERSITY OF IRELAND, CORK

Growth of V_2O_5 Films for Electrochromic and Battery Applications

A Thesis Presented to
The National University of Ireland, Cork
For the Degree of Doctor of Philosophy
by

Igor I. Kazadojev B.Sc.

Department of Chemistry,
Tyndall National Institute,
University College Cork.

July 2018

Supervised by Dr. Ian M. Povey and Prof. Martyn E. Pemble

Table Of Contents:

DECLARATION

All work outlined in this thesis is the original work of the author and has not been submitted for any other degree or qualification.

Signature of the author:

_____

Date _____

ACKNOWLEDGEMENTS

I would like to extend my sincerest gratitude to my supervisors. Dr. Ian Povey for guiding me along my PhD, providing advice, for always being there when I needed a helping hand and offering support throughout the duration of my research. Dr. Shane O'Brien who I could come to consult in time of doubt and who provided a large input into the creation of this thesis. I would also like to thank Professor Martyn Pemble for putting his trust in me and providing the opportunity to conduct research at Tyndall National Institute.

Thanks to all the members of the Advanced Materials and Surfaces Group, who are with us or were with us in the pasts including Dr John Mullins, Melissa McCarthy, Louise Ryan, Dr. Dirk Hagen, Adrian Walsh, Barry Hutchinson, Jan Kegel, Dr. Simon Elliot, Dr. Richard Winfield and Dr. Brendan Sheehan who have all made my time spent at Tyndall fun and memorable.

Thanks to Dr. Patrick Carolyn and Vince Lodge for the microscopy work**.** A special thanks to Dr. Mircea Modreanu for his work on RAMAN and XPS spectroscopy. Thanks to all who provided assistance in various ways during my studies.

I would like to especially thank my wife Darya and my family for the patience, love and support that they have provided during the course of this work.

ABSTRACT

Vanadium pentoxide (V_2O_5) is an electrochromic material. Research into electrochromic devices has become more popular with the renewed interest in environmentally-friendly 'green' technologies. Particular interest is in the production of electrochromic coated windows for energy saving purposes. Over the past year's scientists have struggled to develop electrochromic coated windows which would be of low cost, acceptable optical characteristics, long-term durability and at the same time uniformly coated without pin-holes or gaps. Vanadium pentoxide has also shown potential as a cathode material in electrochemical power sources such as lithium ion batteries, which becomes more significant with the ever-growing demand for portable electronic devices. A large amount of work is being done to develop high performance, reliable and ecologically friendly lithium ion batteries. This research aims to address these requirements.

The first part of the thesis describes the growth of V_2O_5 thin films grown by Aerosol Assisted Chemical Vapour Deposition (AACVD) on fluorine doped tin oxide substrates using vanadyl acetylacetonate ($VO(acac)_2$) as the precursor. It was found that the optimal growth conditions for the films to be used as a cathode material for lithium ion batteries was 400°C for the duration of 1 hour with a post annealing step for 3 hours at 600°C to promote crystallization of the films. Even though the films showed promising electrochemical properties, they suffered from non-uniformity at lower growth temperatures, electrochemical stability issues and poor optical transmittance hence a step to improve these properties was made in the form of doping. Silver was chosen as a metal to dope the V_2O_5 films using silver trifluoroacetate (AgO_2CCF_3) as the doping precursor. It was found that 450°C was the new optimal temperature for the growth and that an increase in crystallinity and a change in preferred orientation and morphology was observed. Higher percentages of silver doping improved the electrochemical properties such as the specific capacity, stability and reversibility of the material over 500 cycles. Even though silver doping improved the electrical properties of the films there were still concerns associated with the uniformity and optical transparency.

In order to solve these shortcomings, it was decided to change both the growth method and the substrate. Atomic Layer Deposition (ALD) was employed with Vanadium(IV) Tetrakis(DimethylAmide) ($V(NMe_2)_4$) as the vanadium source and indium doped tin oxide glass (ITO) as the new substrate. Films were grown using both thermal and plasma ALD for 400 cycles, growth temperature was found to be optimal outside of the ALD window hence the process included a significant chemical vapour deposition (CVD) component. Improvements in the electrical, optical and morphological film quality were observed with ALD when compared to the AACVD grown films. Even though the electrochemical properties of the film were drastically improved the cycling stability still remained an issue. In an effort to solve this and possibly further improve the electrochemical properties silver doping was performed in the ALD mode. The silver precursor, 2,2,6,6 tetramethyl-3,5-heptadionato silver (I) ($AgC_{11}H_{19}O_2$) was added in a super-cycle ALD mode so as to give nominally 5% and 10% silver doped V_2O_5 films. The electrochemical properties of the films were significantly improved in terms of performance and cycling stability.

A detailed comparison between the two growth techniques, the effects of doping and the subsequent properties of the films are presented in this thesis.

Chapter 1: Introduction

1.1 Motivation

Unique structural, optical and electrical properties and a variety of possible applications have made vanadium a subject of much study over the past several decades. Its uses as a catalyst, steel additive and in the aerospace industry are well known.[1] Vanadium oxide based catalysts are used in a variety of different processes as shown in table 1[2-5], but the most well-known ones would be the production of sulfuric acid[6] which is heavily used in industry and in the reduction of environmental pollution by reaction with nitrogen oxide gases which are a by-product in power plants. The importance of using vanadium in metal oxide catalysis can be observed in figure 1.1[1] where it is shown to be the most used metal in the period 1967-2000.

Industrial Process	Catalyst Material
Oxidation of SO_2 to SO_3 in the production of sulfuric acid	V_2O_5
Oxidation of benzene to maleic anhydride	V_2O_5
Oxidation of naphthalene to phthalic anhydride	V, Mo oxides
Oxidation of butane to phthalic anhydride	V, P oxides
Oxidation of *o*-xylene to phthalic anhydride	V, Ti oxides
Selective reduction of NO_x with NH_3	$V_2O_5/WO_3/TiO_2$

Table 1: Industrial catalytic processes using vanadium oxides[1]

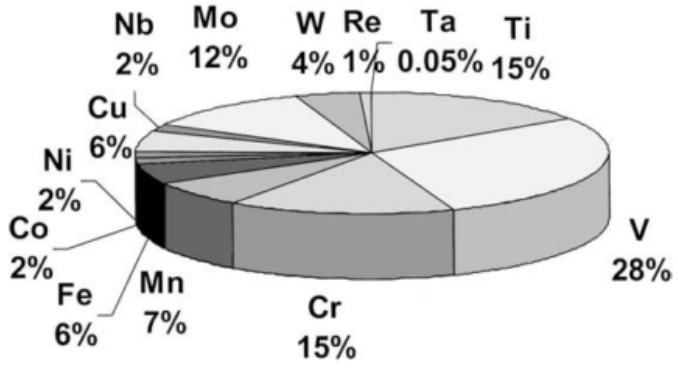

Figure 1.1: Overview of importance of vanadium in supported metal oxide catalysis as observed for the period of 1967-2000.[1]

Another curious property of vanadium oxides lies in the fact that vanadium dioxide and vanadium pentoxide undergo reversible semiconductor-to-metal phase transformations at specific temperatures of 68°C and 257°C respectively. This structural transformation leads to a large change in both electrical and optical properties.[7] This will be examined in more detail later on in the chapter.

Vanadium pentoxide particularly is of interest due to its electrochromic properties. Electrochromic materials have the ability to vary their optical transparency and reflectivity as a response to the application of an electric field, which causes the reversible movement of conductive ions such as Li^+ or H^+ in an electrolyte[8]. Electrochromic materials have the potential to be used for the development of smart windows. An example of a possible schematic of a smart window can be seen in figure 1.2 as proposed by Granqvist[9]. The device should consist of a transparent electrolyte, a thin electrochromic film, a substrate that possesses electrical conducting properties e.g. indium doped tin oxide (ITO), and electrical contacts through which a voltage can be applied. The smart window should in concept act like a battery with a cathode and an anode which would control the flow of charge and depending on the charge would in turn control the optical transparency of the material. It is important that the electrochromic material is stable for long lengths of time and over many operation cycles of switching between bleached and coloured states. As a consequence, this thesis

will emphasise the importance of not only the quality of growth of V_2O_5 films and their electrochromic properties but also their cycling stability.

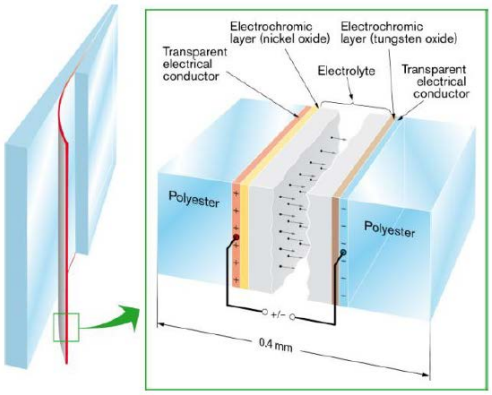

Figure 1.2: Cross-section view of an electrochromic foil-type device implemented as a laminate between glass panes.[10]

As was mentioned above, the electrochromic material should act like a battery. Hence work was done towards considering the use of vanadium pentoxide as a cathode material for lithium ion batteries. V_2O_5 has the potential for efficient electrical storage due to a flexible layered structure where the layers of VO_5 square pyramids are bound together by weak electrostatic interactions with interstitial sites available for intercalation. The flexibility allows vanadium pentoxide to undergo specific phase transformations. These transformations occur when an increasing amount of lithium ions are intercalated into the structure of V_2O_5 and, depending on the amount, can cause either reversible or irreversible structural and electrical changes. The phase transformations will be discussed in more detail in other chapters. Vanadium pentoxide based cathode materials were also found to be cheaper, less toxic and have a higher theoretical capacity than $LiCoO_2$ which is commonly used in industry[11,12]. This will be discussed later on in this chapter.

1.2 Oxides of Vanadium

Since their discovery in the early 19th century, vanadium oxides have been of interest to chemists due to their coloured appearance. These different colours correspond to the

primary oxides of vanadium which range from +2 to +5 with the corresponding colours: VO (violet), V_2O_3 (green), VO_2 (blue), and V_2O_5 (yellow) respectively. Other oxides with mixed valence oxidation states like V_6O_{13} where both V^{5+} and V^{4+} are present are also possible along with oxides with stoichiometry between VO_2 and V_2O_3 where V^{4+} and V^{3+} are present. These mixed valence oxides are possible due to oxygen vacancy defects. If enough vacancies are present, they can band together along a lattice plane by reorganising the V-O coordination units. This results in mixed oxides with related stoichiometries that can take the form of Magnéli phases (V_nO_{2n-1}) and Wadsley phases ($V_{2n}O_{5n-1}$).[13,14,15] The wide range of possible primary and mixed oxides and their associated formation temperatures can be seen in the phase diagram in figure 1.3.

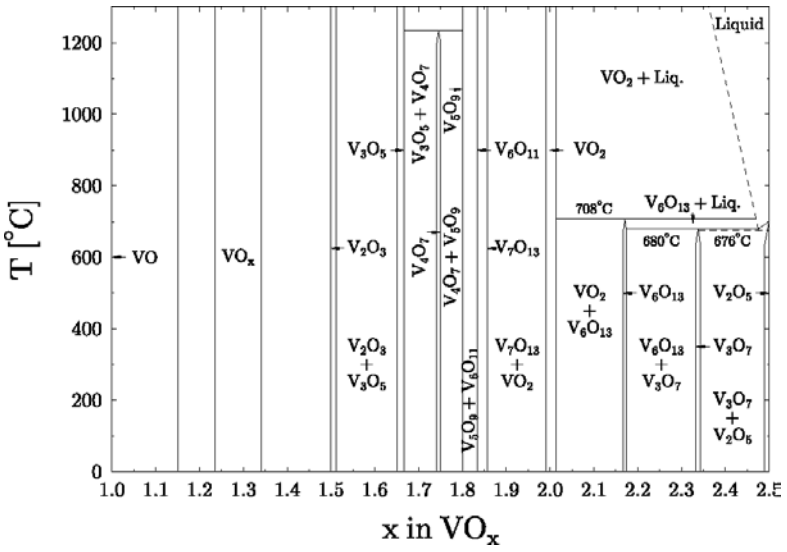

Figure 1.3: Phase diagram of the VO_x system[15-16]

An Ellingham diagram is presented in figure 1.4. It depicts the thermodynamic data for the principle oxides of vanadium. As can be observed from the diagram V_2O_5 is stable across the entire temperature range at oxygen partial pressures which would correspond to air. Such behaviour is indicative of very good thermal stability which is observed for lower oxides only at increased temperatures and decreased pressures.[18]

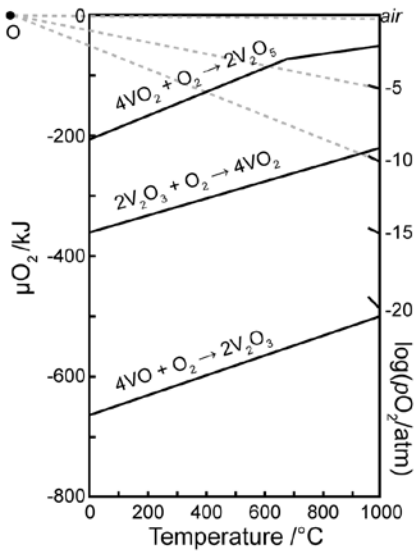

Figure 1.4: The Ellingham Diagram for the V-O system[17,18]

1.3 V_2O_5 Electrical and Optical Properties

Out of all of the oxides V_2O_5 stands out as the most promising from the perspective of electrochromism[19].Vanadium pentoxide (V_2O_5) has the highest oxidation state and is the most stable of all the oxides. It has a layered orthorhombic unit cell structure belonging to the P_{mnm} space group with lattice parameters a=11.150 Å, b=3.563 Å and c=4.370Å.[20] The V_2O_5 layered structure is made up of chains of edge sharing VO_5 square pyramids whose chains are linked together via corner sharing[20] as seen in figure 2.

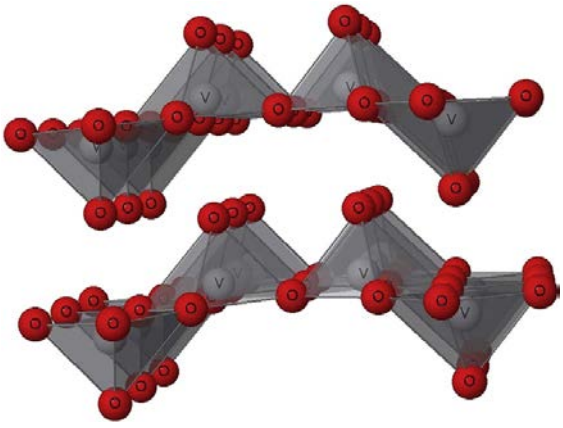

Figure 2: Perspective view of two layers of V_2O_5, V atoms are grey balls, O atoms are red balls, weak van der Waals bonds are omitted for clarity[13]

In 1960 Bachmann et al.[21] made corrections to the V_2O_5 crystal structure that had been initially proposed by Ketelaar[22] and by Byström, Wilhelmi and Brotzen[23]. It was proposed that its structure consisted of trigonal bipyramidal coordinated polyhedra of oxygen bound to vanadium. On the edges the oxygen-vanadium bonds along the [001] plane form zigzag double chains, these then are cross-bound along the [100] plane through mutual corners forming sheets along the x-z plane[24]. Enjalbert and Galy[25] in 1986 made further corrections to the work by Bachmann et al., demonstrating that the VO_5 polyhedra are square pyramids and not trigonal bipyramids. This conclusion was supported by calculations based on the previous work of Galy et al.[26]

V_2O_5 has a distinct yellow colour and it undergoes the same semiconductor-to-metal transition as mentioned previously at 257°C with a significant change in electrical and optical properties. The electrical properties and the unique structure of V_2O_5 have led to extensive research on the potential use of V_2O_5 as a cathode material. For example, when compared to $LiCoO_2$ which is a commercial cathode it offers a larger capacity (294 $mAhg^{-1}$ vs 272$mAhg^{-1}$), moderate voltage, low cost and wide availability.[27] The potential for efficient electrical storage is due to the structure where the layers of VO_5 square pyramids that were mentioned previously are bound together by weak electrostatic interactions with interstitial sites available for intercalation. Due to this the vanadium oxide structures can undergo phase transformations which in turn allows for the intercalation of mobile guest species while still retaining the essential structure.[28] Li-ions are an example of mobile guest species that cause phase transformations once enough are introduced. The process occurs together with compensating electrons leading to the formation of vanadium bronzes in the form of $V_2O_5 + xLi + xe^- \leftrightarrow Li_xV_2O_5$.[29] The phases associated with the insertion of lithium are: α-phase, ε-phase, and δ-phase, γ-phase and the ω-phase. The phases associated with specific amounts of lithium intercalated are as follows: α-V_2O_5 ($x<0.1$) to ε-V_2O_5 ($0.35<x<0.7$) to δ-V_2O_5 ($0.9<x<1$) to γ-V_2O_5 ($x=2$) and to ω-V_2O_5 ($x=3$) where x is the amount of lithium ions intercalated. The formation of the α, ε and δ-phases allows for the structure of the V_2O_5 layers to be more or less preserved. The only changes that are observed are the minute puckering of

the vanadium oxide layers observed for the ε-phase and a slight increase of interlayer spacing and decrease of cell potential for the δ-phase.[30] For the irreversible transformation to the γ-phase, an inversion of half of the square pyramids is observed and a change of the Li-ion coordination environment from orthorhombic to tetrahedral. Also a new potential plateau appears around 2.4 V which is characteristic of the γ-phase.[31] The insertion of more than x=3 lithium ions into the vanadium pentoxide structure at a voltage smaller than 1.9 V leads to the irreversible formation of the ω-phase. This happens due to the formation of a disordered structure as a result of a slight redistribution of vanadium within the oxygen array in order to reduce the electrostatic repulsions. [32]

As mentioned previously in section 1.1, the electrochromic properties of V_2O_5 have made it a major target for scientific research for the purpose of creating smart windows. The viability of electrochromic materials does not just depend on the electrical properties but also on the change in optical properties such as the optical density (OD) and the coloration efficiency (CE), each of which is a function of materials parameters. For example, OD is calculated by using equation 1.0

$$\Delta OD_\lambda = \log(\frac{T_{b\lambda}}{T_{c\lambda}}) \quad \text{(Equation 1.0)}$$

where $T_{b\lambda}$ is the transmittance of the bleached state and $T_{c\lambda}$ is the transmittance in the coloured state. The CE on the other hand is defined as the ratio of change of optical density at corresponding injected/ejected charge density per unit area (Q_{in}) as seen in equation 1.1, where Q_{in} is found using equation 1.2 and where *S* is the area.[33]

$$\eta = \Delta OD_\lambda / Q_{in} \quad \text{(Equation 1.1)}$$

$$Q_{in} = \int idt/\mathrm{S} \quad \text{(Equation 1.2)}$$

Having discussed the motivation for this study and the two major areas of possible application of V_2O_5 it is now important to look at the work that has been previously reported in the literature by other researchers.

References:

1) B.M. Weckhuysen, D.E. Keller, *Catal. Today*, **2003**,78,25-46
2) J.M. Herrmann, J. Disdier, G. Deo, I.E. Wachs, *J. Chem. Soc.*, **1997**, 93, 1655-1660
3) G. Ertl, H. Knözinger, J. Weitkamp, *Handbook of Heterogeneous Catalysis*, **1997**
4) G.C. Bond, S.F. Tahir, *Appl, Catal.*, **1991**, 71, 1-31
5) D. Bushev, *J. Catal.*, **2002**, 205, 115-122
6) N.G. Ashar, K.R. Golwalkar, *A Practical Guide to the Manufacture of Sulfuric Acid, Oleums, and Sulfonating Agents*, Chapter 2: Processes of Manufacture of Sulfuric Acid, Springer International Publishing, **2013**
7) E.E. Chain, *Appl. Opt.*, **1991**, 30, 2782-2787
8) A.D. Kuypers, C.I.M.A. Spee, J.L. Linden, G. Kirchner, J.F. Forsyth, A. Mackor, *Surf. Coatings Technol.*, **1995**, 75, 1033-1037
9) C.G. Granqvist, *Mater. Today Proc.*, **2016**, 3, S2-S11
10) C.G. Granqvist, *J. Vac. Sci. Technol, B*, **2014**, 32, 60801
11) A. Sakunthala, M. V. Reddy, S. Selvasekaparapandian, B. V. R. Chowdari, P. Christopher Selvin, *Energy Environ. Sci.*, **2011**, 4, 1712
12) J-G. Zhang, P. Liu, J. A. Turner, C. E. Tracy, D. K. Benson, *J. Electrochem. Soc.*, **1998**, 145, 6, 1889-1892
13) S. Beke, *Thin Solid Films*, **2011**, 519, 1761-1771
14) H. Katzke, P. Tolèdano, W. Depmeier, *Phys. Rev. B*, **2003**, 68, 1-7
15) S. Andersson, *J. Phys. Chem. Solids*, **1967**, 28, 1613-1621
16) D. Wruck, *Thin Solid Films*, **1989**, 182, 79-85
17) I. Yamaguchi, T. Manabe, T. Tsuchiya, T. Nakajima, M.Sohma, T. Kumagai, *Jpn. J. Appl. Phys.*, **2008**, 47, 1022-1027
18) A.J. Bergerud, *Phase Stability and Transformations in Vanadium Oxide Nanocrystals*, **2016**, University of California, Berkley (Thesis)
19) C.V. Ramana, O.M. Hussain, B. Srinivasulu Naida, C. Julien, M. Balkanski, *Mater. Sci. Eng. B*, **1998**, 52, 32-39
20) A.A. Akl, *Appl. Surf. Sci.*, **2007**, 253, 7094-7099

21) H.G. Bachman, *Z. Kristallogr.*, **1961**, 115, 110-131

22) J.A.A. Ketelaar, *Z. Kristallogr.*, **1936**, 95, 9-27

23) A. Byström, K.A. Wilhelmi, O. Brotzen, *Acta Chem. Scand*, **1950**, 4, 1119-1130

24) P.P. Division, *Z. Kristallogr. Bd*, **1961**, 115, 110-131

25) R. Enjalbert, J. Galy, *Acta Cryst.*, **1986**, C42, 1467-1469

26) J. Galy, *J. Solid State. Chem.*, **1992**, 100, 229-245

27) X. Dai, A. Zhou, J. Xu, Y. Lu, L. Wang, C. Fan, J. Li, *J. Phys. Chem. C*, **2016**, 120. 422-430

28) P.M. Marley, G.A. Horrocks, K.E. Pelcher, S. Banerjee, *Chem. Commun.*, **2015**, 51, 5181-5198

29) D. McNulty, D.N. Buckley, C. O'Dwyer, *J. Power Sources*, **2014**, 267, 831-873

30) C.R. Walk, N. Margalit, *J. Power Sources*, **1997**, 68, 723-725

31) N.A. Chernova, M. Ropollo, A.C. Dillin, M.S. Whittingham, *J. Mater. Chem.*, **2009**, 19, 2526

32) C. Delmas, H. Cognac-Auradou, J.M. Cocciantelly, M. Mènètrier, J.P. Doumerc, *Solid State Ionics*, **1994**, 69, 257-264

33) L. Yang, D. Ge, J. Zhao, Y. Ding, X. Kong, Y. Li, *Sol. Energy Mater. Sol. Cell*, **2012**, 100, 251-257

Chapter 2: VO_x growth: A review

This chapter will discuss the work that has been done previously on the growth of VO_x by both aerosol assisted chemical vapour deposition (AACVD) and atomic layer deposition (ALD) and on the application of V_2O_5 as a battery material. Vanadium oxide films have been previously grown by other growth methods as well, such as: pulsed laser deposition[1,2,3,4], E-beam evaporation[5,6,7], magnetron sputtering[8,9,10], anodic deposition into colloidal spheres[11], spray pyrolysis[12,13,14], colloidal microspheres[15], electrospinning[16], sol-gel[17,18,19,20] and spin coating[21,22]. In this thesis AACVD was chosen as the primary deposition method, to ease precursor handling, lower the precursor cost and enable growth at atmospheric pressure. Subsequently, ALD was employed to allow greater control of thickness and uniformity. Both growth systems will be discussed in detail in Chapter 3 and 4. The structure and characteristics of the vanadium oxide films grown in this thesis will also be discussed in detail in chapters 6, 7, 8 and 9. Since this work focuses on fabrication of high quality electrochromic films and better working electrode materials, observed properties and prior studies relevant to these applications are discussed with emphasis on cycling stability, capacity fading, morphological changes and reliability[23,24,25].

2.2 VO_x CVD literature summary

Previous studies of VO_x growth using CVD variants are presented in table 2, from which some general trends can be highlighted.

Author	Precursor	Deposition Temperature	Oxide Phase	Temperature of Phase formation	Thickness	Year
Maruyama and Ikuta[26]	$V(acac^*)_3$	500°C	VO_2	500°C	20-590nm	1993
Kuypers et al.[27]	$VO[O(C_3H_7)^i]_3 + O_2$	250-380°C 205-370°C	V_2O_5 $W_{25}O_{73}$ $WO3+W_{24}O_{68}$	206-371°C 339 °C 389°C	0.1-1 μmh^{-1}	1995
Barreca et al.[28]	$VO(hfa^*)_2 \cdot H_2O$, $VO(acac^*)_2$ $VO(dpm^*)_2$, $VO(fod^*)_2$	380°C 380°C	V_2O_5** VO_2**	380°C 380°C	40-270nm	1999
Barreca et al.[29]	$VO(hfa^*)_2 \cdot H_2O$	150-370°C	VO_2 + sub-oxides	500°C	50-178nm	2000
Field and Parkin[30]	$VCl_4/VOCl_3 + H_2O$	300-600°C	V_2O_5	350-600/450-600°C	700-1000nm	2000
Manning et al.[31]	$VCl_4 + H_2O$	400-450°C	V_2O_5*** VO_2*** V_6O_{13}***	450-475°C 500-550°C 550°C	0.5-1.5µm	2002
Sahana et al.[32]	$VO(acac^*)_2$	300-600°C	VO_2	370-520°C	1.1-4µm	2002
Manning et al.[33]	$VCl_4 + H_2O$ and $W(OC_2H_5)_6$	500-600°C	$V_2O_5/V_6O_{13}+VO_2$***	500-600°C	400-600nm	2004
Manning and Parkin[34]	$VOCl_3 + H_2O$	350-650°C	VO_2	350-650°C	500nm	2004

Author	Precursor	Deposition Temperature	Oxide Phase	Temperature of Phase formation	Thickness	Year
Vernardou et al.[35]	$VO(acac^*)_2$	375-450°C	VO_2/ VO_2+ V_2O_5/	450°C	n/a	2004
Vernardou et al.[36]	VCl_4 +H_2O/ $VO(acac^*)_2$	450-600/500-575°C	V_2O_5*** V_2O_3/VO_2/V_2O_5***	450/450 450-600°C	n/a	2006
Piccirillo et al.[37]	$VO(acac^*)_2$/$V(acac^*)_3$	500-600°C	V_2O_3/VO_2/V_2O_5***	500-600°C	400-700nm	2007
Piccirillo et al.[38]	$VO(acac^*)_2$ + $Nb(OEt)_5$	500°C	VO_2	500°C	n/a	2007
Piccirillo et al.[39]	$VO(acac^*)_2$ + $W(OC_2H_5)_5$	550°C	VO_2	550°C	n/a	2007
Binions et al.[40]	$VO(acac^*)_2$ + WCl_6	350-600°C	VO_2	475-550°C	n/a	2007
Mathur et al.[41]	$VO[O(C_3H_7)^i]_3$	400-700°C	V_2O_5 + V_3O_7 V_2O_5	450°C 500°C	0.3µm.min^{-1}	2007
Binions et al.[42]	$VO(acac^*)_2$ + $HAuCl_4$	525°C	VO_2+Au+V_2O_5 VO_2 +Au***	150°C	100-300nm	2008
Su et al.[43]	$VO(acac^*)_2$	500°C,450-250°C,150°C	VO_2, V_2O_5	500°C	n/a	2008
Beardslee et al.[44]	$VO(NO_3)_3$ / $VO[O(C_3H_7)^i]_3$	250-700°C, 300-500°C	V_2O_5 + V_3O_7	350-400°C	n/a	2010
Nandakumar et al.[45]	$VO(OC_3H_7)_3$ +H_2O	100-300°C	V_2O_5	180-300°C	30-200nm	2011
Warwick et al.[46]	$VO(acac^*)_2$	530°C	VO_2+ V_2O_5	530°C ****	200-1580nm	2013

*(hfa=1, 1, 1, 5, 5, 5-hexafluoro-2,4-pentanedione) *(acac=$C_5H_7O_2$), (dmp*=2,2-6,6-tetramethyl-3,5-heptanedione), (fod*=2,2-dimethyl-6,6,7,7,8,8,8-heptafluoro-3,5-dionato), (**Phases were pressure dependent, see paper, (***Phase were dependant on precursor ratios, see paper) (****Phase depended on voltage, see paper)

Table 2.0: Summary of previously reported VO_x growths by CVD

It was found that vanadyl acetylacetonate and chlorine based vanadium precursors were the most widely used for the growth of both VO_2 and V_2O_5 films. These precursors were chosen because of their price, availability and ease of use. On average deposition temperatures varied from 300-600°C, but in some cases they were as low as 100°C and as high as 700°C. The temperatures of phase formation were different however. Vanadium pentoxide films were deposited in the temperature range of 350-600°C with the lowest being reported by Nandakumar et al.[45]; this was reported to be due to the precursor reacting with water which acted as the oxidizing agent thus allowing for a lower growth temperature. Plasma-enhanced chemical vapour deposition also allowed for lower deposition temperatures as seen by Barreca et al.[29]and Kuypers et al.[27]. Overall the main aspect required for the formation of V_2O_5 films was the presence of an oxygen rich atmosphere.

Vanadium dioxide was mostly formed at higher temperatures of 500°C but some variations were observed, as in the case of Barrecca et al.[29] where PE-CVD was used and Su et al.[43] who showed the possibility to grow VO_2 at 150-250°C using vanadyl acetylacetonate. As was mentioned previously, the atmosphere at which the growth was carried out was important and VO_2 films grew better in an oxygen deficient atmosphere. Intermediate growth temperatures gave rise to mixed oxidation states which contained both V_2O_5 and VO_2 as well as other sub-oxides such as V_2O_3, V_6O_{13} and V_7O_{13}.

The growth rates of both types of oxide films varied from paper to paper but in general it was found that V_2O_5 films were thicker than VO_2 films with the same growth durations. Properties of the films were also affected by the thickness. Thermochromic phase transitions occurred at ~68°C for VO_2 and ~257°C for V_2O_5, the nature of which were influenced by the thickness[27]. Gas flow rates, precursor ratios and concentrations were also found to influence the rate of growth and type of oxide grown. For example, Barecca et al.[28] found that at higher oxygen flow rates, films grown using PE-CVD suffered from a decrease in crystallinity and an increase of the surface roughness due to increased ion bombardment. In most cases a post annealing step was vital when V_2O_5 was required, as in the cases of Beardslee et al.[44] and Nandakumar et al.[45]. A post

annealing step was also required to produce specific phases, as in Sahana et al.[32] where annealing in argon was required to produce rutile VO_2 (R) from monoclinic VO_2 (B). Overall it can be seen that the growth of specific vanadium oxides requires the consideration of many factors that might influence the deposition and formation of the oxides.

2.3 VO_x ALD literature summary

ALD is a finely controlled growth technique that can produce conformal layers on the sub nanometre thickness scale at both low temperatures and high complexity 3D structures[47,48,49,50]. Previous ALD growth studies are summarised and tabulated in table 2.1 [51,52,53,54]

Author	Precursor	Deposition Temperature	Growth Product	Temperature of Phase formation	Thickness	Year
Musschoot et al.[52]	$VO[O(C_3H_7)^i]_3+H_2O/O_2$	200-300°C	V_2O_5	150°C	650-800nm	2009
Blanquart et al.[53]	$V(NEtMe)_4$	75-250°C	VO_2	700°C* 700°C	20-50nm	2013
Niskanen et al.[54]	$Ag(O_2C^tBu)(PEt_3)$** Ag(fod)***	140°C	Ag	140°C	40nm	2007
Kariniemi et al.[55]	$Ag(fod)(PEt_3)$***	120-150°C	Ag	120-140°C	17-30nm	2011

*(Annealed under O_2 and N_2 atmospheres respectively), **$Ag(O_2C^tBu)(PEt_3)$ - (2,2-dimethylpropionato)silver(I)(triethylphosphine), (fod***=2,2-dimethyl-6,6,7,7,8,8,8-heptafluoro-3,5-dionato)

Table 2.1: Summary of the reported ALD growths of VO_x and Ag

Musschoot[57] studied the growth of V_2O_5 thin films using both plasma and thermal ALD and a combination of vanadium(V) oxytriisopropoxide and water and oxygen as the oxidising agents. It was shown that the deposition rate depends not only on the choice of

the deposition method but also on the type of oxidising agent used. The understanding of these processes allowed Musschoot to achieve a much higher growth rate for V_2O_5, than previously reported for thermal water ALD processes[56]. Blanquart et al.[53] did further research on the subject of how the choice of an oxidising agent can strongly influence the film deposition rate. It was found that depending on whether ozone or water is used as the oxidising agent the mechanism of film deposition and deposition rate would differ. The use of ozone allowed for a combustion process and a steady increase in the growth rate at higher temperatures due to precursor degradation and CVD type growth. On the other hand, the use of water allowed for steady self-limiting growth due to the presence of an ALD window. It was also observed that the atmosphere in which the films are annealed can play a key role in what type of oxide that is formed with an oxygen rich atmosphere required to form V_2O_5.

Growth studies of silver thin films by ALD are not common due to precursor instability and the inability to transfer CVD chemistry to the self-limiting ALD regime. In order to implement silver doping to ALD grown films an understanding of the processes of silver growth and the types of precursors used was required. A review of the two main studies that have investigated silver growth by ALD done by Niskanen et al.[54] and Kariniemi et al[55] was carried out.

This study by Niskanen et al.[54] showed the successful growth of silver thin films by radical-enchanced ALD using (2,2dimethylpropionato)silver(I)triethylphosphine as the precursor, giving stable, uniform and conformal films that showed high purity when compared to other films produced by well-established REALD recipes. Kariniemi et al.[55] further expanded on the topic of ALD grown silver films by using Plasma-Enhanced ALD. Films were deposited using Ag(fod), Ag(thd)(PEt_3), Ag(fod)(PEt_3), Ag(Piv) and Ag(Piv)(PEt_3), where fod is (2,2-dimethyl-6,6,7,7,8,8,8-heptafluorooctane-3,5-dianato), thd is (2,2,6,6-tetramethyl-heptane-3,5-dianato) and Piv is (2,2-dimethylpropianato) which were synthesised in house. A hydrogen plasma was used as the co-reagent to reduce the silver. Ag(fod)(PEt_3) was found to be the best precursor for the ALD process as it left only a small percentage of residue according to the TGA studies when compared to other precursors.

2.4 V_2O_5 for battery applications literature summary

As mentioned previously in chapter 1.3 vanadium pentoxide has the potential to be used in lithium ion battery applications. A significant number of studies have aimed to develop thin films with the correct stoichiometry and macro and micro structures required for efficient battery electrodes. Doping has also been utilized for the purpose of improving the electrical properties of the films as will be seen later in both this chapter and in chapters 7 and 9.

Author	Precursor	Growth Technique	Structure Design	Thickness	Electrolyte	Current Density (mAg^{-1})	Discharge Capacity ($mAhg^{-1}$)	Year
Nam et al.[57]	n/a	Mag.Sput	Thin films	1.4µm	LIPON*	50 µAh/cm^2	80 µAhcm^{-2}	2001
Mantoux et al.[58]	[VO(OC_3H_7)$^i_3$]	CVD	Thin films	240,400, 1600 nm	$LiClO_4$PC**	n/a	245	2004
Hwang et al.[59]	V + Ag metal	Mag.Sput	Thin films	n/a	LIPON	n/a	80 µAhcm^{-2}-um	2004
Lee et al.[23]	V_2O_5 powder	Sol-gel	Thin films, Platelets, Fibrillar	20-30nm particles	$LiClO_4$PC**	0.27A/g	1240,720,25	200
Van et al.[60]	[VO(OC_3H_7)$_3$]	ALCVD	Thin films	200, 450 nm	$LiClO_4$PC**	n/a	455,275	2006
Murugan et al.[61]	V_2O_5 + PEDOT	Microwave	Nanoribbons	n/a	$LiPF_6$	15	n/a	2007
Groult et al.[62]	VO[O(C_3H_7)^i]$_3$	CVD	Thin films	1.8µm, 3.5µm	$LiClO_4$PC**	n/a	220,160,105	2007

Author	Precursor	Growth Technique	Structure Design	Thickness	Electrolyte	Current Density (mAg^{-1})	Discharge Capacity ($mAhg^{-1}$)	Year
Chou et al.[63]	V_2O_5 powder	Hydrothermal Method	Nanoribbons Nanowires microflakes	n/a	$(C_3mpyr)[NTf_2]$ + $LiNTf_2$ $LiPF_6$	n/a	115, 82, 47, 430, 427, 347, 255	2008
Zhu et al.[15]	$VO(acac)_2$ + $Cu(acac)_2$	Self-assembly	Microspheres	n/a	$LiPF_6$/EC/DEC	80, 400	319 (Un-doped) 328 (Doped)	2008
Pan et al.[64]	V_2O_5 + $H_2C_2O_4$	Thermal Dec	Nanoparticles	n/a	$LiPF_6$	n/a	270/198	2010
Liu et al.[25]	V_2O_5 + H_2O_2	Cathodic Deposition	Thin-films	600nm	$LiClO_4$PC**	200	274 402	2011
Sakunthala et al.[65]	NH_4VO_3	Polymer precursor	Thin Films	n/a	$LiPF_6$/EC/DMC	120	261, 250	2011
Rubloff et al.[50]	$[VO(OC_3H_7)_3]$	CVD, ALD	Nanostructure Sponge	2mm	$LiPF_6$/EC/DEC	1,1, 5.6, 27.9, 55.9	1248µAhcm^{-2}	2012
Chen et al.[51]	$[VO(OC_3H_7)^i_3$	ALD	Thin film	30nm	(EC:DEC)^	147,294,441^	321,283,230, 198	2013

*LIPON- lithium phosphorus oxynitride,**1M $LiClO_4$-propylene Carbonate, ^^lithium perchlorate in propylene carbonate, ^(Ethylene carbonate/diethyl carbonate), *(for 1Li/V_2O_5, 2Li/V_2O_5 and 3Li/V_2O_5), *(for 10,30,60 and 120 nm thicknesses), PEDOT- poly(3,4-ethylenedioxythiophene),

Table 2.2: Summary of the reported growths of V_2O_5 for battery applications

Previous studies for the growth of V_2O_5 for battery applications are summarised in table 2.2, from which behavioural trends can be observed. Nam et al.[57] and Zhu et al.[15] concluded that the incorporation of a dopant metal such as copper enhanced the electrical properties of V_2O_5 film by increasing the current density and discharge capacity values due to changes in copper oxidation during the cycling.[66,67] The dopant metals niobium and tantalum were considered by Sakuntala et al.[65] and were shown to influence the morphology and electrochemical properties of V_2O_5 films improving the

current density and cycling stability of the battery material. Groult et al.[62] investigated the effect that deposition on different substrates such as platinum, titanium, stainless steel, FTO, glass, mica and Si substrates might have on the electrochemical properties of V_2O_5 films. It was found that when tested in a small potential window, films grown on stainless steel substrates proved to be the most efficient and stable while others would suffer from poor stability and constantly diminishing current density. Mantoux et al.[58] and Lee.et al[15] investigated the effects of growth time and temperature and found that these parameters not only strongly influence the type of oxide deposited but also the surface morphology. Depending on the structure type at the surface it was shown that the electrical properties either improved or worsened. When a comparison between planar, platelet and fibrillary-structures of V_2O_5 was carried out it was found that the platelet-type structures had the best overall performance. Pan et al.[64], Liu et al.[25] and Murugan et al.[61] carried out further research into the matter and found that the size of the surface structures also played a key role in determining the efficiency of a battery material. V_2O_5 nanostructures were shown to be more efficient due to increased surface area and more efficient lithium ion transport. Many growth methods have been used for the purpose of growing V_2O_5 structures for battery applications, as summarised in table 2.2, however it is the CVD and ALD work of Chen[50] and Rubloff et al.[51] that are key to this work. In these studies, they observed that thin films deposited using CVD and ALD were able to perform very efficiently as battery materials possessing large current density and discharge capacity values while also being stable over a large number of cycles.

References:

1) X.D. Wu, S.R. Foltyn, R.C. Dye, A.R. Garcia, N.S. Nogar, R.E. Muenchausen, *Thin Solid Films*, **1992**, 218, 310-315
2) J. Zhang, J. Mcgraw, J. Turner, D. Ginley, *J. Electrochem. Soc*., **1997**, 5, 144, 1630-1634
3) S. Beke, S. Giorgio, L. Korosi, L. Nanai, W. Marine, *Thin Solid Films*, **2008**, 516, 4659-4664
4) Y. Iida, Y. Kanno, *J. Mater. Process. Technol*., **2009**, 209, 2421-2427
5) C.V. Ramana, O.M. Hussain, B.S. Naidu, P.J. Reddy, *Mater. Sci. Eng. B*, **1998**, *52*, 32–39.
6) C.V. Ramana, O.M. Hussain, B.S. Naidu, P.J. Reddy, *Thin Solid Films*, **1997**, 305, 219–226.
7) A. Kumar, P. Singh, N. Kulkarni, D. Kaur, *Thin Solid Films*., **2008**, 516, 912–918.
8) H. Cui, V. Teixeira, L. Meng, R. Wang, J.Gao, E. Fortunato, *Thin Solid Films*, **2008**, 516, 1484–1488.
9) M.S.B. de Castro, C.L. Ferreira, R.R. de Avillez, *Infrared Phys. Technol*., **2013**, 60, 103–107.
10) L-J. Meng, R.A. Silva, H-N. Cui, V. Teixeira, M.P. dos Santos, Z. Xu, *Thin Solid Films*, **2006**, 515, 195–200.
11) Z. Tong, J. Hao, K. Zhang, J. Zhao, B-L. Su, Y. Li, *J. Mater. Chem. C*, **2014**, 2, 3651.
12) L. Boudaoud, N. Benramdane, R. Desfeux, B. Khelifa, C. Mathieu, *Catal. Today*, **2006**, 113, 230–234.
13) B. Wang, K. Konstantinov, D. Wexler, H. Liu, G. Wang, *Electrochim. Acta*, **2009**, 54, 1420–1425.
14) A. Bouzidi, N. Benramdane, A. Nakrela, C. Mathieu, B. Khelifia, R. Desfeux, A. Da Costa, *Mater. Sci. Eng. B*, **2002**, 95, 141–147.
15) D. Zhu, H. Liu, L. Lv, Y.D. Yao, W.Z. Yang, *Scr. Mater*., **2008**, 59, 642–645.
16) P. Viswanathamurthi, N. Bhattarai, H.Y. Kim, D.R. Lee, *Scr. Mater*., **2003**, *49*, 577–581

17) Z.S. El Mandouh, M.S. Selim, *Thin Solid Films*, **2000**, 371, 259-263
18) A. Jin, W.Chen, Q. Zhu, Y. Yang, V.L. Volkov, G.S. Zakharova, *Thin Solid Films*, **2009**, 517, 2023–2028.
19) D. McNulty, D.N. Buckley, C. O'Dwyer, *J. Power Sources*, **2014**, 267, 831–873.
20) H. Li, P. He, Y. Wang, E. Hosono, H. Zhou, *J. Mater. Chem*., **2011**, 21, 10999.
21) Z. Wang, J. Chen, X. Hu, *Thin Solid Films*, **2000**, 375, 238–241.
22) K. Jeyalakshmi, K.K. Purushothaman, G. Muralidharan, *Philos. Mag*., **2013**, 93, 1490–1499.
23) K. Lee, Y. Wang, G. Cao, *J.Phys. Chem. B*, **2005**, 109, 16700–16704.
24) E. Østeng, K.B. Gandrud, Y. Hu, O. Nilsen, H. Fjellvåg, *J. Mater. Chem. A*, **2014**, 2, 15044–15051.
25) Y. Liu, M. Clark, Q. Zhang, D. Yu, D. Liu, J. Liu, G. Cao, *Adv. Energy Mater*., **2011**, 1, 194–202.
26) T. Maruyama, Y. Ikuta, *J. Mater. Sci*., **1993**, 28, 5073–5078.
27) A.D. Kuypers, C.I.M.A. Spee, J.L. Linden, G. Kirchner, J.F. Forsyth, A. Mackor, *Surf. Coatings Technol*., **1995**, 75, 1033–1037.
28) D. Barreca, L.E. Depero, E. Franzato, G.A. Rizzi, L. Sangaletti, E. Tondello, U. Vettori, *J. Electrochem. Soc*., **1999**, 146 (2), 551–558.
29) D. Barreca, L. Armelao, F. Caccavale, V. Di Noto, A. Gregori, G.A. Rizzi, E. Tondello, *Chem. Mater*., **2000**, 12, 98-103
30) M.N. Field, I.P. Parkin, *J. Mater. Chem*., **2000**, *10*, 1863–1866.
31) T.D. Manning, I.P. Parkin, R.J.H. Clark, D.Sheel, M.E.Pemble, D. Vernardou, *J. Mater. Chem*., **2002**, 12, 2936–2939.
32) M.B.Sahana, G.N. Subbanna, S.A. Shivashankar, *J. Appl. Phys*., **2002**, 92, 6495–6504.
33) T.D. Manning, I.P. Parkin, *Chem.Mater*., **2004**, 23, 744–749.
34) T.D. Manning, I.P. Parkin, *Polyhedron*, **2004**, 23, 3087–3095.
35) D. Vernardou, M.E.Pemble, D.Sheel, *Surf. Coatings Technol*., **2004**, 188–189, 250–254.
36) D. Vernardou, M.E.Pemble, D.Sheel, *Chem. Vap. Deposition*, **2006**, *12*, 263–274.
37) C. Piccirillo, R. Binions, I.P. Parkin, *Chem. Vap. Deposition*, **2007**, 13, 145–151.

38) C. Piccirillo, R. Binions, I.P. Parkin, *Eur. J. Inorg. Chem*., **2007**, 4050–4055.
39) C. Piccirillo, R. Binions, I.P. Parkin, *Thin Solid Films*, **2008**, 516, 1992–1997.
40) R. Binions, C. Piccirillo, I.P. Parkin, *Surf. Coatings Technol*., **2007**, *201*, 9369–9372.
41) R. Binions, C. Piccirillo, R.G. Palgrave, I.P. Parkin, *Chem. Vap. Deposition*, **2008**, 14, 33–39.
42) S. Mathur, T. Ruegamer, I. Grobelsek, *Chem. Vap. Deposition*, **2007**, 13, 42–47.
43) Q.Su, C.K, Huang, Y, Wang, Y.C. Fan, B.A. Lu, W. Lan, Y.Y. Wang, X.Q. Liu, *J. Alloys Compd*., **2009**, 475, 518–523.
44) J.A. Beardslee, A.K. Mebust, A.S. Chaimowitz, C.R. Davis-VanAtta, H.Leonard, T.L. Moersch, M. Y. Afridi, C.J. Taylor, *Chem. Vap. Deposition*, **2010**, 16, 206–210.
45) N. K. Nandakumar, E.G. Seebauer, *Thin Solid Films*, **2011**, 519, 3663–3668.
46) M.E.A. Warwick, I. Ridley, R. Binions, *Surf. Coatings Technol*., **2013**, 230, 163–167.
47) V. Miikkulainen, M. Leskelä, M. Ritala, R.L. Puurunen, *J. Appl. Phys*., **2013**, 113, 021301(1)-021301(101).
48) M. Leskelä, M. Ritala, *Thin Solid Films*, **2002**, 409, 138–146.
49) A. C. Jones, M. L. Hitchman, *Chemical Vapour Deposition: Precursors, Processes and Applications*, *Chapter 4: Atomic Layer Deposition*, First Ed, RSC, 2009.
50) X. Chen, E. Pomerantseva, K. Gregorczyk, R. Ghodssi, G. Rubloff, *RSC Adv.*, **2013**, 3, 4294-4302
51) X. Chen, E. Pomerantseva, P. Banerjeem, K. Gregorczyk, R. Ghodssi, G. Rubloff, *Chem. Mater.,* **2012**, 24, 1255–1261.
52) J. Musschoot, D. Deduytsche, H. Poelman, J. Harmers, R.L. Van Meirhaeghe, S. Van Den Berghe, C. Detavernier, *J. Electrochem. Soc.,* **2009**, 156 (7), 122-126
53) T. Blanquart, J. Niinistö, M. Gavagnin, V. Longo, M. Heikkilä, E. Puukilainen, V.R. Pallem, C. Dussarrat, M. Ritala, M. Leskelä, *RSC Adv.,* **2013**, 3, 1179-1185.
54) A. Niskanen, T. Hatanpää, K. Arstila, M. Leskelä, M. Ritala, *Chem. Vap. Deposition,* **2007**, 13, 408–413.

55) M. Kariniemi, J. Ninistö, T. Hatanpää, M. Kemell, T. Sajavaara, M. Ritala, M. Leskelä, *Chem. Mater.*, **2011**, 23, 2901–2907.

56) J.C. Badot, S. Ribes, E.B. Yousfi, V. Vivier, J.P. Pereira-Ramos, N. Baffier, D. Lincot, *Electrochem. Solid-State Lett.*, **2000**, 3, 485–488.

57) S.C. Nam, Y.C. Lim, H.Y. Park, E.J.Jeon, Y.S. Yoon, W.I. Cho, B.W.Cho, K.S.Yu, *Korean J.Chem.Eng.*, **2001**, 18, 673–678.

58) A. Mantoux, H. Groult, E. Balnois, P. Doppelt, L. Gueroudji, *J. Electrochem. Soc.*, **2004**, 151, A368-A373

59) H.S. Hwang, S.H. Oh, H.S. Kim, W.I. Cho, B.W. Cho, D.Y. Lee, *Electrochim. Acta*, **2004**, 50, 485–489.

60) K.Le Van, H. Groult, A. Mantoux, L. Perrigaud, F. Lantelme, R. Lindström, R. Badour-Hadjean, S. Zanna, D. Lincot, *J. Power Sources*, **2006**, 160, 592–601.

61) A. Vadivel, M.V. Reddy, G. Campet, K. Vijayamohanan, *J. Electroanal. Chem.*, **2007**, 603, 287–296.

62) H. Groult, K.Le Van, A. Mantoux, L. Perrigaud, P. Doppelt, *J. Power Sources*, **2007**, 174, 312–320.

63) S-L. Chou, J-Z. Wang, J-Z. Sun, D.Wexler, M. Forsyth, H-K. Liu, D.R. MacFarlane, S-X. Dou, *Chem. Mater.*, **2008**, 20, 7044–7051.

64) A.Pan, J-G. Zhang, Z. Nie, G. Cao, B.W. Arey, G. Li, S. Liang, J.Liu, *J. Mater. Chem.*, **2010**, *20*, 9193.

65) A. Sakunthala, M.V. Reddy, S. Selvasekarapandian, B.V.R. Chowdari, P.C. Selvin, *Energy Environ. Sci.*, **2011**, 4, 1712-1725

66) Y. Takeda, K. Itoh, R. Kanno, T. Icikawa, N. Imanishi, O. Yamamoto, *J. Electrochem. Soc.*, **1991**, 138, 2566–2571.

67) E. Andrukaitis, *J. Power Sources*, **1997**, 68, 656–659.

Chapter 3: Introduction to Chemical Vapour Deposition

Having looked at potential uses of VOx films and the work previously carried out in the literature, it is paramount to look at the historical, theoretical and practical aspects of chemical vapour deposition to gain a better understanding of the processes taking place.

3.1 Historical aspects of CVD:

The development of CVD has been very rapid due to the many difficulties that other film deposition technologies have encountered when tasked with dealing with issues such as large scale production of functional glass coatings or the growth of multiple layer high quality films that are required for the rapidly growing semiconductor industry.[1] The earliest mention of the CVD process in scientific literature was by R. W. Bunsen[2] in 1852 when he observed the condensation of iron oxide from volcanic gases that contained hydrogen chloride[3]. Several years later Wöhler[4] used WCl_6 in a hydrogen carrier gas for the deposition of tungsten metal in a heated glass tube. This was followed by L. Mond[5] in 1890 when he synthesised nickel tetracarbonyl $Ni(CO)_4$ which thermally decomposed to produce pure nickel, a process that was used for the refinement of nickel ore.[2,6,7,8] John Howarth was one of the first to patent a CVD procedure, which was designed for the production of "carbon black" in a process where a natural-gas flame was made to impinge on a water-cooled soapstone block. The product of the reaction was used as a pigment back in 1870, after which the reaction was improved and is still used today.[2,6] Ten years later a patent was issued to Sawyer and Mann[9] for a process for the production of improved carbon fibre filaments by depositing so-called pyrolytic carbon, which due to defects has covalent bonding between the graphene sheets making it extra durable. The process was carried out by heating the filaments in a hydrocarbon rich atmosphere and then cooling and allowing for crystallisation of the pyrolytic carbon to occur. This improved the lifetime of carbon filament bulbs, which had been invented by Edison.[2] Glass production was also revolutionised by the implementation of "on-

line" CVD architectural coatings by Pilkington[10]. This process involved the use of atmospheric pressure CVD at the very large scale of a float glass production line. Most significant was the CVD production of fluorine-doped tin oxide, which proved to be more economically viable and could be produced at increased scale compared to "off-line" deposition processes such as sputtering.

In a broader sense CVD involves formation of a thin solid film on a surface via a chemical reaction of vapour phase precursors. It is therefore distinct from physical adsorption of atomic or molecular species on a surface and from solution-based methods of thin film formation.[10] The 1960's was a major time for breakthroughs in Metal-Organic CVD processes and during that time the first III-V materials were made using CVD by Didchenko et al.[11] This was done by heating a mixture of Me_3In and PH_3 in a closed tube to form InP. A similar process was used in 1962 to produce InSb and GaAs. In 1965 Monstanto claimed that methods for deposition of III-V materials on semiconductors had been achieved.[12,13,14] The actual term Metal-Organic Chemical Vapour Deposition (MOCVD) was only mentioned in 1968. During that year, Manasevit in the Rockwell Corporation published a process for the deposition of GaAs by heating a mixture of [Et_3Ga] and [AsH_3] in an open tube system with H_2 as the carrier gas. This process was given as an example of a metal-organic reaction of III-V materials when Manasevit patented the MOCVD process for a range of III-V materials and wide band-gap semiconductors.[15, 16] MOCVD was taken up with renewed effort in the mid 1980's with the discovery of superconducting oxides and efforts to grow thin films of these oxides. Liquid injection MOCVD was also introduced at that stage in order to overcome issues associated with the transport of low volatility metal precursors.[17, 18]

Metal oxide thin films are used in applications ranging from protective coatings to functional layers and sensors. Particular applications have acted as the motivation for development of a wide range of deposition techniques, including physical methods (sputtering, evaporation), solution methods (sol-gel, chemical solution deposition) and chemical vapour methods (CVD, ALD). The main advantage of vapour methods is that they can be used to coat large areas uniformly at relatively low cost. An example of this would be that they have been used to coat window glass for enhanced energy

conservation since 2000.[19] With the use of high-k dielectrics in integrated circuits on silicon, there has been increased demand for methods to deposit thin films of oxides. It was found that PVD was not suitable due to lack of desired control over film growth and thickness.

CVD differs from PVD because thin film deposition takes place via a chemical reaction of two species and not by physical methods like sputtering, physical evaporation or sublimation. As a result, CVD has certain advantages:

- It is a non-line-of-sight process which ensures uniform thickness of coating.
- Extensive range of precursors to choose from, such as halides, hydrides, organometallics, nitrides, oxides, sulfides.
- Deposition of materials can be carried out at temperatures which are much lower than their melting temperatures.
- Stoichiometry, surface morphology, crystal structure and orientation of CVD products can be controlled.
- Deposition rate can be easily adjusted through process control.

However, there are some disadvantages associated with CVD as well:

- CVD can require precursors that can be toxic and hazardous to health.
- Precursors can be expensive.
- It can be hard to control and fine-tune the process so as to get desired film properties.[20]

Consequently, CVD processes continue to be examined and developed so as to provide a solution to these problems, along with the parallel development of ALD.[21, 22]

There are a large number of acronyms used to describe specific CVD variants, including Plasma-Enhanced CVD (PECVD), Low Pressure CVD (LPCVD) and Aerosol Assisted CVD (AACVD). They are grouped by primary parameters in figure 3.0.

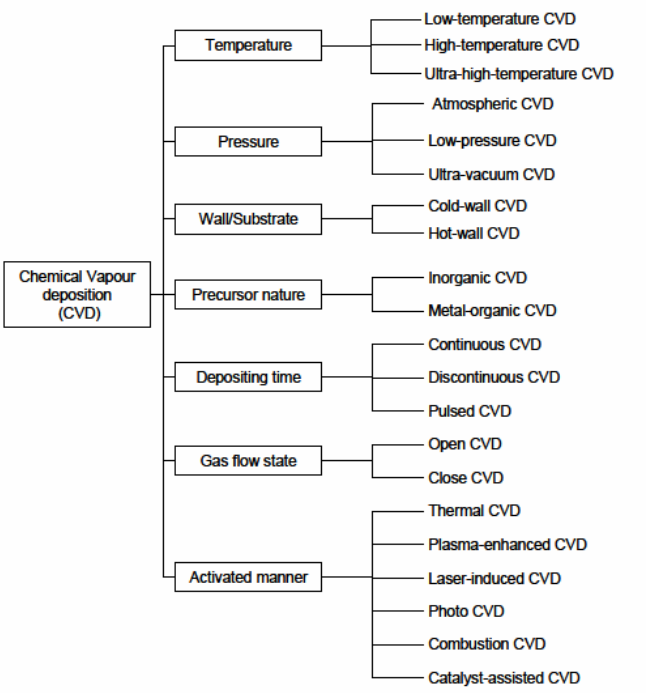

Figure 3.0: Classification of CVD methods[23]

For example, low pressure CVD is used when superior conformal step coverage and better film homogeneity is needed, whereas plasma-enhanced CVD is used when low temperatures are required.[24] Each of these methods is unique and is important for different applications relying on the different factors such as temperature and pressure for activation.

In this thesis we will focus on a specific type of chemical vapour deposition, namely aerosol assisted chemical vapour deposition (AACVD). Many different variants of AACVD have been developed such as aerosol assisted metal-organic CVD (AAMO-CVD), aerosol assisted plasma CVD (AA-PCVD), flame-assisted chemical vapour deposition (AACCVD), electrostatic-assisted chemical vapour deposition (ESAVD) and electrostatic-assisted aerosol jet deposition (EAAJD).[25] The most significant feature of AACVD is that the precursor being used is not required to be highly volatile, rather it needs to have a high solubility in a solvent. An aerosol can be generated from the precursor solution by using the inverse piezoelectric effect (in the form of a sonicator), electrostratic aerosol generator, atomization or electrospraying method. After this the aerosol can be easily transported into the reaction chamber by a carrier gas. Due to these

qualities AACVD has certain advantages over other standard CVD methods. These advantages include cost and availability, opportunity for industrial size scaling, ease of precursor handling and delivery, high deposition rate and the possibility to run at atmospheric or low pressures. These particular advantages have led to an increase of interest in this particular type of CVD and have allowed for its widespread use in both laboratory and industrial scale processes.[25]

3.2 Principles and Kinetics of CVD

Chemical vapour deposition involves the transfer of precursor molecules which are either liquid or gaseous to a reaction chamber in the vapour phase by a carrier gas which is inert. Chemical vapour deposition involves the transfer of precursor molecules which are either liquid or gaseous to a reaction chamber in the vapour phase by a carrier gas which is inert. It is imperative that the carrier gas is inert under transport conditions so that the precursor does not undergo any side reactions while it travels to the reaction chamber. Nitrogen and argon are most commonly used for this. Precursor molecules can then react either in the gas phase or on the surface of a substrate eventually forming a stable, solid product on the surface of the substrate.

An activation factor is required for the reaction to kick-start, which is usually in the form of heat, light or plasma. Most commonly it takes the form of heat. The heating is facilitated by using either a hot or cold wall reactor.[20,26,27] As was stated earlier, the reactions can take place either in the gas phase near the surface or on the surface of a heated substrate. A reaction in the gas phase is said to be of a homogeneous nature whereas the latter is heterogeneous.[26] CVD is an additive process, where new layers of a material are added to the substrate surface. The process does not rely on any other complementary techniques for a strong bond to form between the layer and substrate, since the reaction occurs on the atomic level. It should be noted that it is assumed that gases at normal pressures which are used in CVD (Ar, He, H_2, CH_4 etc.) behave as ideal gases.[20]

Chemically, CVD growth consists of a set of complex phenomena[28] which are divided into several steps and should be considered as seen in figure 3.1. These phenomena are 1) First gas-phase phenomena which take into account the homogeneous reactions between gases in the reactor; 2) Surface phenomena which account for heterogeneous reactions which take place on the substrate surface and the process of mass transport of gaseous precursors; 3) Second gas-phase phenomena which describe the desorption, removal and transfer of gaseous by-products from the surface to the boundary layer. These are described in detail further on. The overall deposition rate is limited by the slowest of the steps.[29]

First Gas-phase phenomena: (steps 1 and 2)

Homogeneous chemical reactions occur in the bulk gas and in the boundary layer, which is represented by step 1. These reactions can lead to the formation of intermediate species which along with any un-reacted precursor molecules are transported within the boundary layer to the substrate surface which is represented by step 2.

Surface phenomena**:** (steps 3, 4, 5)

Reactant and intermediate species are deposited onto the surface of the substrate as seen in step 3. These species will then migrate to other preferential sites along the surface as shown in step 4. Heterogeneous reactions will then take place and film deposition will occur as illustrated in step 5.

Second Gas-phase phenomena: (steps 6 and 7)

In the final stages of CVD growth, the gaseous by-products of the reaction are desorbed from the substrate surface as indicated by step 6, after which they cross the boundary layer and are expelled through the exhaust as in step 7. These can be collected and re-cycled for further use or just disposed of, depending on the viability of such a process. It should be noted that the homogeneous chemical reactions take place completely in the gas phase, as seen in steps 1-3, whereas heterogeneous reactions take place on the substrate surface, which is illustrated in steps 4 and 5.[28]

Considering the complexity of a CVD system and reactor design, fluid flow must also be accounted for and this is done via the Reynolds (Re) number. The Reynolds number is usually expressed as $Re = \frac{\rho u}{\mu}$ where ρ=mass density, u= flow density and μ= viscosity and is closely associated with the boundary layer. The boundary layer is defined as a thin fluid film which forms on the surface of a solid body moving through a viscous liquid. As the Reynolds number increases the boundary layer becomes thinner, thus affecting the mass transport of the system.[26,29]

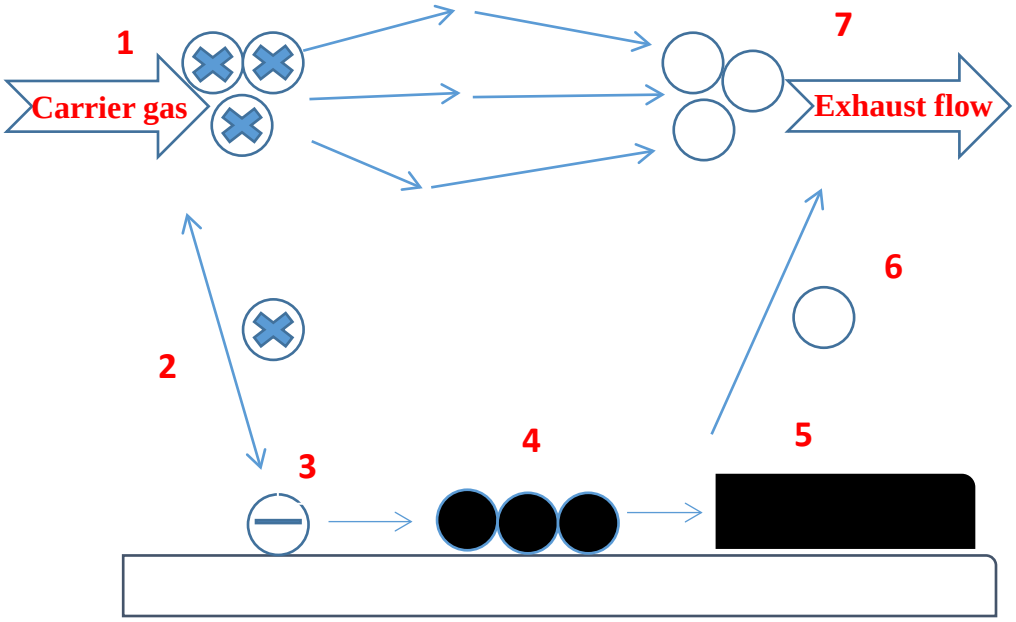

Figure 3.1: Diagram of processes involved in Chemical vapour deposition

1-Homogeneous reactions take place in the bulk gas and binary layer, 2- Transport of the above mentioned species though the boundary layer to the substrate surface, 3-Deposition of species onto substrate surface, 4-Migration to preferential sites on the surface, 5-Heterogeneous reactions and formation of film, 6-Desorption from the surface and movement through the boundary layer, 7-Expelling of by-product into the exhaust

3.3 CVD kit design and operation

Regardless of what type of CVD system is required, the following key components need to be present in the system: 1) Precursor and carrier gas delivery system 2) Reaction chamber 3) Exhaust system

3.3.1 Conventional CVD design

Precursor and carrier gas delivery system:

Precursor selection is very important, as it is the first step in designing CVD experiments. There are different criteria that should be considered when choosing a precursor. A good precursor will have a low vaporization temperature and good volatility since this will allow for easy vaporization and transfer of the precursor if it is in liquid or solid form and will prevent it sticking to the walls of the piping while it is transferred to the reaction chamber. Precursor stability is another factor which should be taken into consideration, as it is vital for the precursor to reach the reaction chamber without undergoing any side chemical reactions during the transfer. Precursor toxicity is important when possible scaling of the process to industrial level can take place, as it is not desirable to use toxic and polluting chemicals in fear of health and safety issues.

Cost of the precursor can also be an issue when running large batch processes. It is sometimes key to the feasibility of using a process in an industrial context.

An adequately designed precursor delivery system as seen in figure 3.2 is also key to ensure efficient precursor transfer and prevent condensation or side-reactions. Usually the precursor delivery system is composed of several things. First of all, a carrier gas source which is usually an inert gas like nitrogen (N_2) or argon (Ar) that will ensure no secondary reaction takes place with the precursor. Secondly, proper piping of a non-reactive material, which is usually stainless steel tubing. A mass flow controller is also required to control the flow of gas in the system. The precursor vessel is typically in the form of a bubbler containing a liquid or solid precursor, which can be heated to allow evaporation to take place. This sealed vessel is connected to the gas supply and allows

the carrier gas to take the precursor to the reaction chamber. Alternatively, it can be a simple container which is connected to the gas supply and holds a liquid precursor in a solvent, from which an aerosol can be generated, as in the case of Aerosol assisted chemical vapour deposition (AACVD).[30]

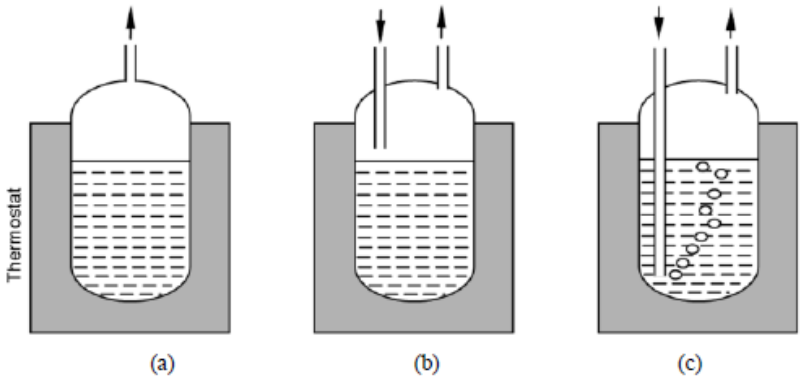

Figure 3.2: Different types of liquid precursor delivery: a) direct vaporization b) carrier gas sweeping c) bubbling method[23]

Reaction chamber:

There are two types of CVD reactors: a hot-wall reactor and a cold-wall reactor as seen in figure 3.3. These can be fabricated with a range of geometries, for example: horizontal, vertical, semi-pancake, barrel and multiple wafer chamber are all in common use as seen in figure 3.4. All of them share structural features such as a load lock system to allow for transport and isolation of substrates from the atmosphere, a stage or a holder for said substrates and some form of a heating system to heat either the walls of the reactor, the substrate holder or the actual substrate. The difference between the hot and cold wall reactors is in the way the substrate is heated. A hot-wall reactor uses indirect heating of the substrate via a furnace; this enables a uniform and accurate temperature maintenance, though it suffers from the coating of the interior of the reactor, which can hinder future deposition and cause lower quality results. A cold-wall reactor uses direct heating of the substrate which removes the problem of the deposition on the walls of the reactor and allows for a more controlled growth to occur, though it can sometimes suffer from non-uniform coating due to a concentration gradient of the reactive species.[31]

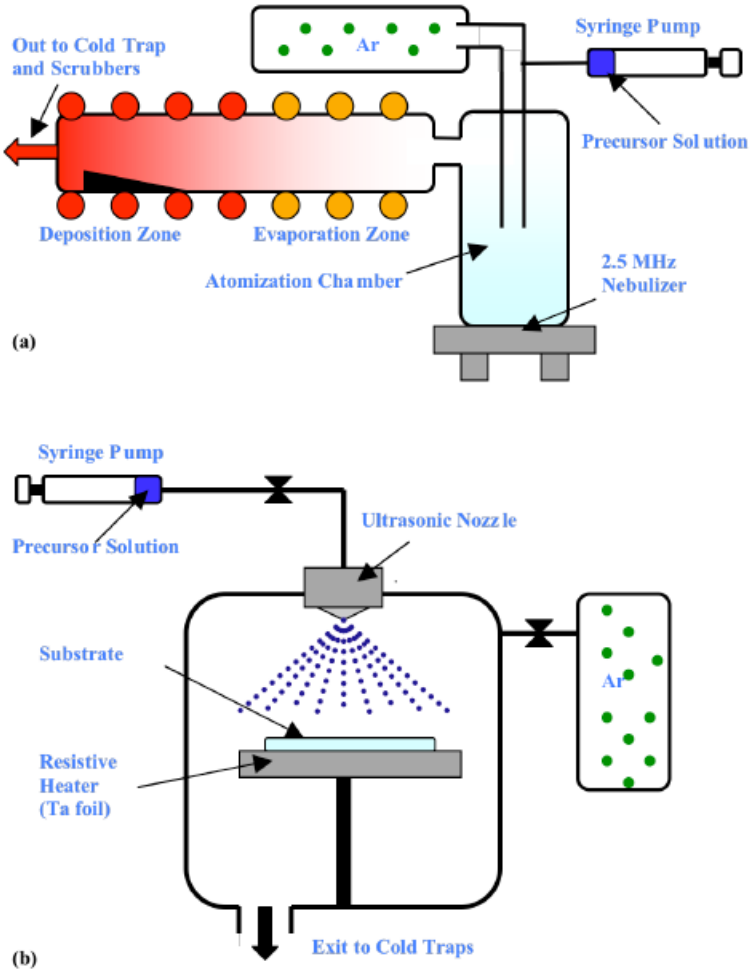

Figure 3.3: Example of two types of atmospheric pressure CVD reactors: a) Hot-wall horizontal reactor b) Cold-wall vertical reactor[32]

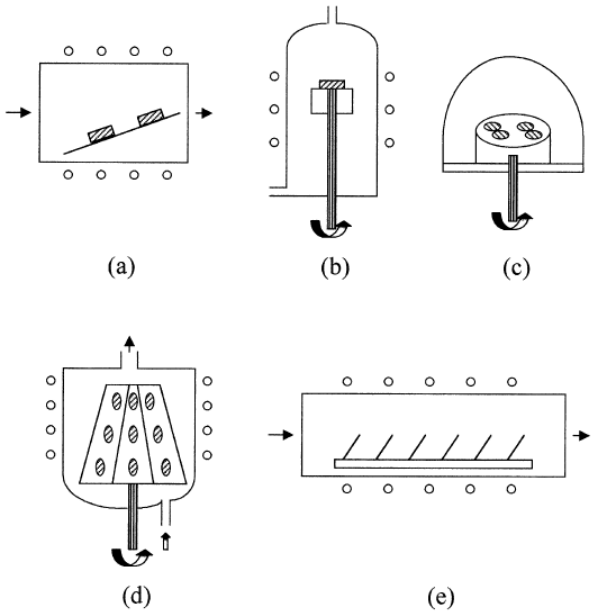

Figure 3.4: CVD reactor configurations: a) Horizontal, b) Vertical, c) semi-pancake, d) barrel, e) multiple wafer.[26]

Exhaust system:

A specialized exhaust system may be required if the CVD system is using precursors which are highly toxic or very expensive. An efficient filter system would be necessary when dealing with toxic, poisonous or corrosive precursors which cannot be simply vented off into the atmosphere, whereas a precursor recovery system might only be used if recovering a precursor. A cold trap which takes the form of a liquid nitrogen trap can be used for these purposes as seen in figure 3.5.

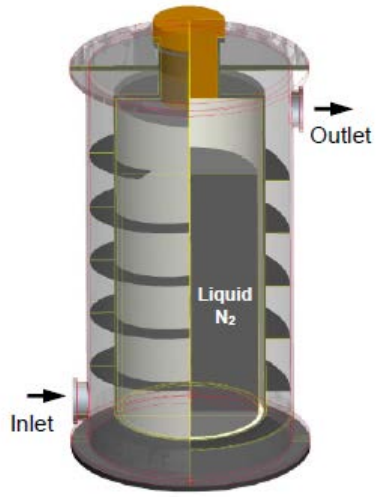

Figure 3.5: Schematic of liquid nitrogen cold trap[23]

3.3.2 Aerosol-Assisted CVD

Aerosol-Assisted Chemical Vapour Deposition (AACVD) is a variant of the conventional CVD growth process which uses small droplets in the form of an aerosol vapour generated from a liquid precursor. The aerosol is transported into the reaction chamber by an inert carrier gas. An example of an apparatus used for AACVD can be seen in figure 3.6. A particular advantage of this type of process is that the precursor does not need to be highly volatile, but rather must be soluble in the solvent from which the aerosol is generated. This broadens the choice of precursors so as to include some that would otherwise be unusable with other CVD growth techniques. Along with a wider choice of precursors, the technique is capable of a high deposition rate which originates from the high mass transport rate of the precursor. AACVD can also operate under low pressure, atmospheric pressure or even in an open atmosphere, which makes it a versatile technique for a large number of a processes[33,27,34,26]. These and other advantages have made AACVD a very popular growth technique which is still actively being used nowadays in both research and industrial environments.

There are many sub-variants of AACVD which were mentioned in chapter 3.1, but the standard AACVD growth process can be seen in figure 3.7. The process starts off with the atomization and generation of an aerosol of the precursor or mixture of precursors

dissolved in a solvent. This can be done by using either ultrasonic aerosol generation, pneumatic aerosol jet or electrostatic aerosol atomization techniques. An inert carrier gas such as N_2 or Ar is used to carry the aerosol into the reaction chamber where the solvent is evaporated and the vaporization of the precursor takes place. It is paramount that complete vaporization of the precursor takes place in the gas phase before reaching the substrate surface as otherwise the deposition technique will take on the form of spray pyrolysis rather than CVD. During the vaporization partial decomposition of the precursor can take place. The precursor along with intermediate species will be adsorbed onto the substrate surface, where they will undergo migration and heterogeneous reactions leading to the formation of the desired film, which is similar to what was presented in Chapter 3.2. Homogeneous reactions in the gaseous phase can also take place if the deposition temperature is too high. Such reactions can lead to the formation of fine particles which can either be adsorbed onto the surface and form porous films through subsequent heterogeneous reactions or can be collected in the form of powders from the gas phase. Even though the deposition mechanism is similar to that of conventional CVD, the model for AACVD processes is more complex and not as well understood. The deposition process is sensitive to contamination and residue as they may directly impact the deposition rate and the film quality.[25]

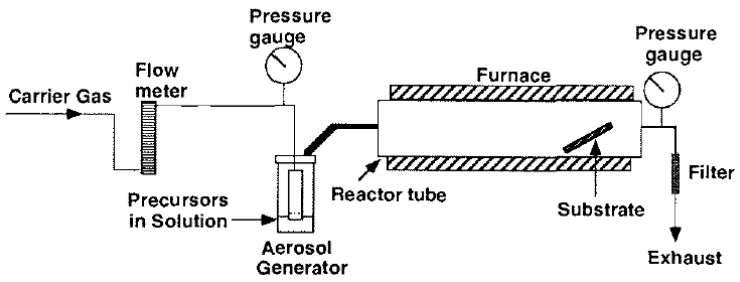

Figure 3.6: Schematic of an AACVD kit used for film growth.[35]

The need to efficiently atomize the precursor has led to the development of different atomization approaches, but as mentioned before three stand out in particular: ultrasonic aerosol generation, pneumatic aerosol jet or electrostatic aerosol atomization. Each atomizes the precursor differently with different droplet sizes, size distributions and atomization rates.[35]

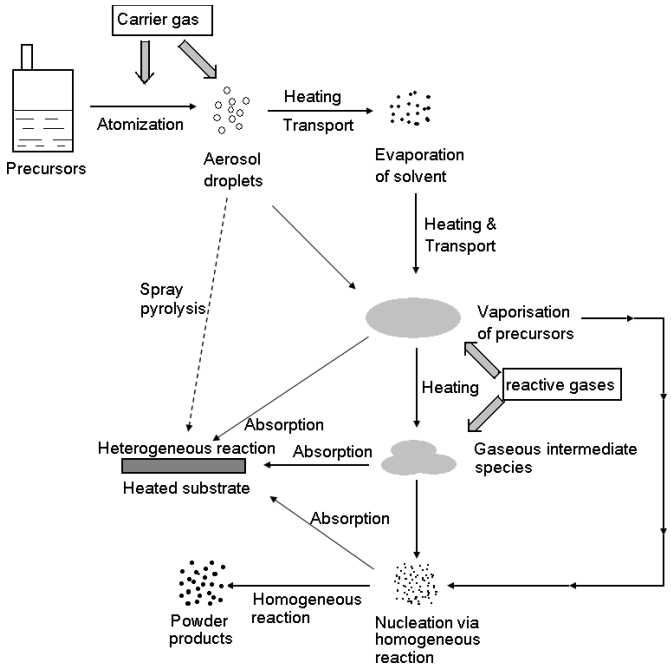

Figure 3.7: Schematic diagram for AACVD growth process.[25]

Ultrasonic aerosol generation is one of the most commonly used methods and also the method that was used in this thesis. It is based on the use of an ultrasonic nebulizer that utilizes a piezoelectric effect under the influence of high-frequency electric field. The nebulizer is placed underneath the precursor vessel immersed in a coupling liquid, which in the case of this work was water. An electric field is applied and vibrations take place which in turn lead to a process known as cavitation, where the formation and collapse of cavities takes place. These cavities excite capillary waves on the surface of the liquid that eventually become unstable and break up, leading to the formation of aerosol droplets. The amount produced can be controlled by varying the power of the nebulizer and the flow rate of the carrier gas.[36,25] A formula for the calculation of particle size produced during the aerosol generation can be seen in equation 2[37,25] where d is the diameter of droplets, k is a constant, ρ is the density of the liquid, γ is the surface tension of the liquid and f is the ultrasonic frequency. This equation suggests that when the physical characteristics of the liquid are known it is quite easy to calculate the diameter of the droplets from the ultrasonic frequency.

$$d = k\left(\frac{2\pi\gamma}{\rho f^2}\right)^{\frac{1}{3}} \quad \text{Equation 2.0}^{37}$$

The experimental set-up and the process for the growth of AACVD films in this thesis will be further discussed in chapter 6.1.

References:

1) M. L.Hitchman, K. F. Jensen, *Chemical Vapour Deposition, Chapter 1*, First Ed, Academic Press, New York, **1989**.
2) M. Allendorf, *Electrochem. Soc. Interface*, **1998**, 1–3.
3) *R. L. Moon, Y. M. Houng, Chemical Vapour Deposition, Chapter 6,* First Ed, Academic Press, New York, **1989**
4) F. Wöhler, L. Uslar, Lieb. Ann, 1855, 94, 255 (Patent).
5) L. Mond, C. Langer, F. Quincke, *J. Chem. Soc.*, **1890**, 57 , 749.
6) J. F. Gallie, *Petroleum. Refiner*., **1944**, 23, 176.
7) L. Mond, *U.S Patent* **1891**, 455,230,
8) L.Mond, *Chem.Ind.*, **1930**, 49T, 371 (Patent).
9) W. E. Sawyer, A. Mann, *U.S Patent,* **1880,** 229, 335,
10) A. C. Jones, M. L. Hitchman, *Chemical Vapour Deposition: Precursors, Processes and Applications, Chapter 1,* First Ed, RCS, **2009**.
11) R. Didchenko, J. D. Alix, R. H. Toeniskoettler, *J. Inorg. Chem.*, **1960**, 4, 35.
12) B. Harrison, E. H. Tomkins, *Inorg. Chem.*, **1962**, 1, 951.
13) Monsanto Co. U.S Patent Applications, **1961**, 113,108, 129, 919.
14) Monsanto Co. UK Patent, **1965**, 1,011,979.
15) H. M. Manasevit, U.S. Patent, **1983**, 4, 368,098C.
16) H. M. Manasevit, *Appl. Phys. Lett.*, **1968**, 12, 156.
17) A. D. Berry, D. K. Gaskill, R. T. Holm, E. J. Cukauskas, R. Kaplan, R. L. Henry, *Appl. Phys. Lett.,* **1988**, 52, 1743.
18) D. Christen, J. Narayan, L. Scneemeyer, *Mater. Res. Soc. Symp. Proc.*, **1990**, 169
19) R. G. Gordon, *MRS Bull.,* **2000**, 52–57.
20) X. T.Yan, Y. Xu, *Chemical Vapour Deposition An Integrated Engineering Design for Advanced Materials, Chapter 1,* First Ed, Springer-Verlag London, **2010**.
21) T. Suntola, *Mater. Sci. Rep.,* **1989**, 4, 261

22) T. Suntola, J. Antson, U.S Patent, **1977**, 4,085, 430

23) X. T. Yan, Y. Xu. *Chemical Vapour Deposition An Integrated Engineering Design for Advanced Materials, Chapter 3,* First Ed, Springer-Verlag London, **2010**.

24) A. R. Barron, *Adv. Mater. Opt. Electron.*, **1996**, 6, 101–114.

25) X. Hou, K. L. Choy, *Chem. Vap. Deposition*, **2006**, 12, 583–596.

26) K. Choy, *Prog. Mater. Sci.,* **2003**, 48, 57–170.

27) P. Marchand, I. A. Hassan, I. P. Parkin, C. J. Carmalt, *Dalton Trans.,* **2013**, 42, 9406–9422.

28) X. T. Yan, Y. Xu. *Thermodynamics and Kinetics of Chemical Vapour Deposition, Chapter 4*, First Ed, Springer-Verlag London, **2010**.

29) X. T. Yan, Y. Xu. *Physical Fundamentals of Chemical Vapour Deposition Gas Laws and Kinetic Theory, Chapter 2*, First Ed, Springer-Verlag London, **2010**.

30) A. Bouzidi, N. Benramdane, A. Nakrela, C. Mathieu, B.Khelifa, R. Desfeux, A. Da Costa. *Mater. Sci. Eng. B*, **2002**, 95, 141–147.

31) A. Jin, W. Chen, Q. Zhu, Y. Yang, V. L. Volkov, G. S. Zakharova. *Thin Solid Films*, **2009**, 517, 2023–2028.

32) A. F. Hepp, J. S. McNatt, J. E. Dickman,; M. H. C. Jin, K. K. Banger, C. V. Kelly, A. R. A. Gonzalez, A. A. Rockett. *Fourth Int. Energy Convers. Eng. Conf. Exhib.,* **2006**, 1–15.

33) C. Piccirillo, R. Binions, I. P. Parkin. *Eur. J. Inorg. Chem.,* **2007**, 4050–4055.

34) M.Saeli, R. Binions, C.Piccirillo, G. Hyett, I. P. Parkin. *Polyhedron*, **2009**, 28, 2233–2239.

35) A. Gurav. T. Kodas, T. Pluym, Y. Xiong. *Aerosol Sci. Technol.,* **1993**, 19, 411–452

36) M. Kerker. *Adv. Colloid Interface Sci.,* **1975**, 5, 105–172.

37) J. N. Antonevich. *IRE. Trans. Ultrason. Eng.,* **1959**, Vol- PGUE-7, 6–15.

Chapter 4: Introduction to Atomic Layer Deposition (ALD)

4.1 Historical perspectives of ALD:

Atomic layer deposition (ALD) is a sub-set of Chemical Vapour Deposition (CVD). CVD describes all deposition methods in which deposition and film growth is based on chemical reactions involving vapour phase reactants. In the case of ALD, the deposition and film growth process is structured around alternation of pulses of precursor gases and co-reagent gases separated by purges of an inert gas or vacuum. These precursors and co-reagents undergo sequential self-limiting chemical reactions on the surface of the substrate. As a deposition method ALD is unique because as it can produce conformal material layers down to just several nanometers in thickness and is able to coat complex 3-D structures with a high degree of uniformity.[1,2,3]

The theory of Atomic Layering (as ALD was originally named) was first reported in early 1960 by a joint team of Prof. V. B Aleksovskii and Prof. S. I. Kol'tsov. The theory was based on Prof. V. B. Aleskovskii's "skeleton hypothesis" which he proposed in his work in 1952.[4] The theory proposes that all solids can be considered as consisting of a skeleton that is made up of covalent structures, which are surrounded by groups that functionalize the broken surface bonds. Chemical assembly on the surface can proceed either by reactions on the surface or by reactions of the functionalizing groups with chemicals being introduced into the system.[5] The work of Aleksovskii centred around the study of chemical reactions on silica and alumina surfaces.[6]

Subsequently ALE (Atomic layer Epitaxy), was developed and patented in Finland by T. Suntola and co-workers in the 1970's. The original outline of the apparatus that was patented consisted of: a source of two precursors which would be used to grow thin films by alternating pulses of the precursors and purges of a vacuum. The thin films that

were mentioned in the patent were ZnS, SnO_2 and GaP and these were deposited on glass substrates with the intention to create thin film electroluminescent displays.[7]

In the 1980's and 1990's work was mainly focused on the growth of polycrystalline and amorphous II/VI and III/V materials such as ZnSe/ZnTe[8] and GaAs/AlGaAs/InGaAs[9] respectively using ALE. A variety of modified ALE methods were developed such as flow-rate modulation epitaxy (FME), gas source high vacuum ALE or molecular layer epitaxy ALE (MLE) and migration enhanced epitaxy (MEE) as seen in the review by Herman et al.[10] Some of the primary work on ALE of II/VI and III/V materials was carried out by George et al.[11], Nishizawa et al.[9], Usui and Watanabe et al.[12] Suntola et al.[13], Goodman et al.[14] and Pessa et al.[15]. The considerable interest in II/VI materials was because of their possible use in electroluminescent displays,[14] whereas III/V materials were proposed to be used in high-speed electronic devices and semiconductor lasers[13]. Even though much work has been carried out on the growth of these materials, problems related to low throughput, purity and complicated surface chemistry came in the way of a massive breakthrough that was initially expected.[17,14]

The use of the term atomic layer deposition (ALD) instead of atomic layer epitaxy (ALE) has appeared due to the growing amount of films that were no longer deposited epitaxially.[11] Atomic layer deposition was revitalized because of the demand for coating high aspect structures and for growing metal oxides for the rapidly developing miniaturization of semiconductor technologies. The required thickness of films decreased to sub-hundred nanometers and lately to as small as a few nanometers for integrated circuits.[18,19] This practically eliminated the problem of the low deposition rate that was hindering the ALD technique from wider application.[2] In nanoelectronics ALD is used in the production of complementary metal-oxide-semiconductor (CMOS) devices, metal-oxide-semiconductor field-effect transistors (MOSFETS) and dynamic random access memory (DRAM) where very thin films of high-k dielectrics such as Al_2O_3, ZrO_2 and HfO_2 play a crucial role (k is the permittivity)[20]. Initially silicon oxide (SiO_2) was used as a gate dielectric in MOSFETs, but the constantly decreasing size of the transistors led to the problem of unacceptably high tunnelling currents through the very thin SiO_2 layer. The problem was solved by replacing SiO_2 with physically thicker

high-k oxides deposited by ALD[21]. Besides being used in the nanoelectronics industry, ALD is also used for the coating of optical waveguides[22], batteries[23,24] and nanoparticles[25].

4.2 Principles and Kinetics of ALD

Atomic layer deposition (ALD) can be summarised as a technique for the growth of uniform and conformal thin films which is based on the sequential use of gas-solid reactions that are self-limiting in nature. The processes which take place during an ALD reaction cycle can be seen in figure 4. First heat treatment is applied to remove any physisorbed species on the substrate to allow for chemisorption of reacting species to occur. The first gaseous precursor is introduced into the reaction chamber and the chemisorption of this precursor on to the surface of the substrate occurs. This is known as the first "half-cycle". This is followed by purge step, which involves either the introduction of a vacuum or an inert carrier gas, with the purpose of removing any unreacted species in the system and preventing uncontrolled growth. A second gaseous precursor or other gaseous co-reactant is introduced into the reaction chamber and the system undergoes a gas-solid reaction in the second "half-cycle". The system is then again purged of any unreacted species. This then completes an entire sequence also known as an "ALD cycle" which ideally results in the growth of a "monolayer" but this is rarely the case. The amount of material deposited in one ALD cycle (growth per cycle) depends on how the reactions of each half-cycle self-limit. The thickness of the grown film will depend on the growth rate and the amount of ALD cycles completed. [1,26,27,28]

Different types of adsorption are possible during ALD growth as seen in figure 4.1. The dashed vertical line is indicative of the end of the first pulse step and the start of the purge step. For characteristic ALD growth to take place i.e. to be conformal over large areas and self-limiting, irreversible saturating adsorption has to take place and it has to be allowed to fully saturate as seen in figure 4.1 (a).[1] Saturation can take place if the reactant of the gas-solid reactions does not physisorb or decompose on the surface at the set temperature.[26]

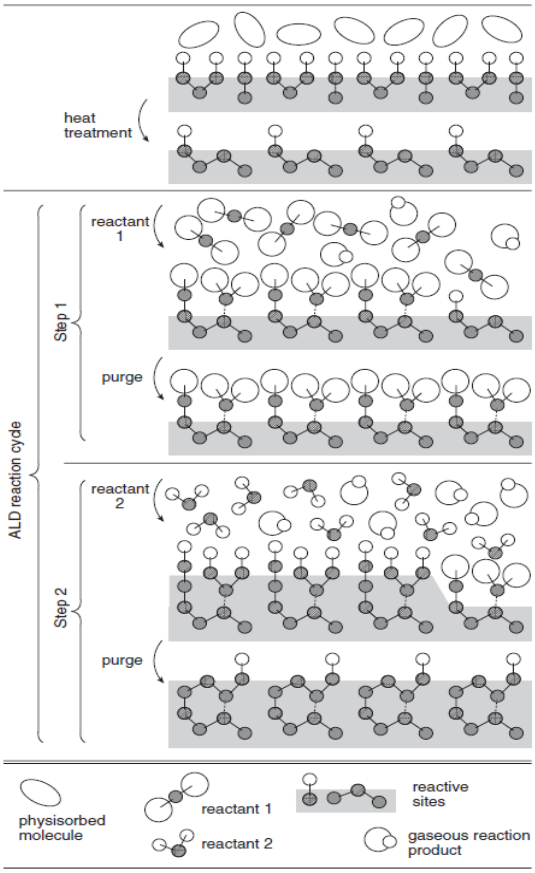

Figure 4**:** A schematic of an ALD reaction cycle[26]

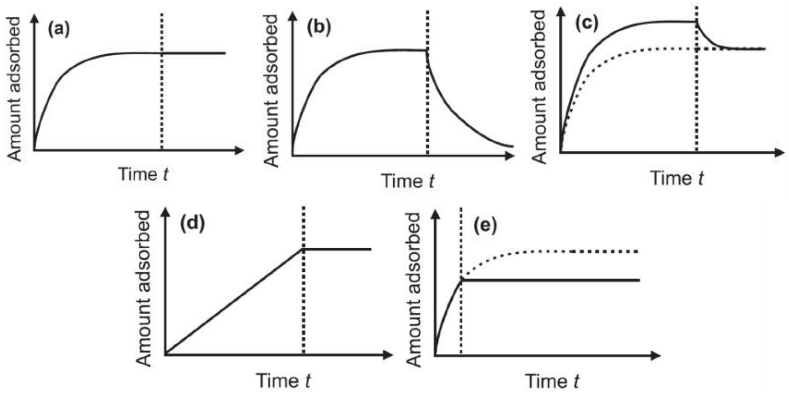

As Figure 4.1: Schematic illustration of different types of adsorption: a) irreversible saturating adsorption, b) reversible saturating adsorption, c) combined reversible and irreversible saturating adsorption, d) irreversible non-saturating adsorption, e) irreversible saturating adsorption not allowed to saturate.[1]

Saturation of the surface reactions is crucial for ALD and is related to the type of adsorption that is taking place: physisorption or chemisorption, where the difference lies in how adsorbed molecules interact with the surface of the substrate. Physisorption is based on weak attractive forces such as van der Waals forces between the adsorbing molecules and the surface and does not involve bond forming or breaking. Physisorption is not specific to the molecule-surface pair interaction and hence can result in multilayers. Chemisorption relies on the formation of or breaking of chemical bonds. This also involves a change in the electronic structure and often requires an activation energy to be overcome; therefore, it cannot be easily reversed. The formation of a chemical bond takes place between the surface and the adsorbing molecule, i.e the reacting species. In a well-behaved ALD system, the surface can accommodate only one layer of the adsorbing species at a time.[28]

With the knowledge of the ALD reaction cycle also came the need to find out the fraction of a monolayer of target material that can be produced during a pulse. Goodman and Peesa[15] in 1986 proposed that for the growth of a monolayer in an ideal ALE mode, as the number of reactive sites gets smaller, then the number of atoms (molecules) that are being adsorbed onto the surface of the substrate will be equal to the number of atoms (molecules) that are being re-evaporated from the surface and only the species that are chemisorbed will remain on the surface after the chamber is purged from any by-products or excess atoms (molecules). This theory though working for ALE is not suitable for ALD as the growth of less than a monolayer per cycle is common as in the case of the growth of Al_2O_3 where the growth during a single cycle is less than a monolayer[27]. This is due to such effects as steric hindrance and filling of reactive sites. These processes are explained by the following mechanism.

There are three different ways or three different mechanisms by which chemisorption can take place as seen in figure 4.2[26]:

1) Ligand Exchange mechanism
2) Dissociation mechanism
3) Association mechanism

1) <u>Ligand Exchange mechanism</u>:

In this type of mechanism, the adsorbing molecular species (ML_n) is adsorbed onto the surface of the substrate (||-S) in such a way that the molecular species (ML_n) is split and loses a ligand L which is combined with the surface group on top of the substrate (||-S) to make the following gaseous species $SL_{(g)}$. Here (||)- is the substrate surface, (-S)- is the surface functional group and (L)- is a ligand.

$$(1)\ ML_{n\,(g)} + ||\text{-}S \longrightarrow\ ||\text{-}ML_{n-1} + LS_{(g)}$$

2) <u>Dissociation mechanism:</u>

This type of chemisorption mechanism is different from (1) in that the reacting molecular species (ML_n) during the adsorption process is split into two parts both of which bind to the reacting sites (||M'-Z||). No gaseous by-product is formed in this reaction. Here (||M'-Z||) are two reactive sites on the surface. An example would be the reaction of $TiCl_4$ with H_2O on silica[29]

$$(2)\ ML_{n\,(g)} + ||M'\text{-}Z|| \longrightarrow\ ||M'L + ||Z\text{-}ML_{n-1}$$

3) <u>Association mechanism:</u>

What makes this mechanism different from (1) and (2) is that there is no splitting of the reacting molecular species or loss of ligands. Instead a bond is formed with the reactive site on the substrate surface. An example would be the reaction of $TiCl_4$ with H_2O on substrates other than silica[30]

$$(3)\ ML_{n\,(g)} + || \longrightarrow\ ||\text{---}ML_n$$

Out of the three, the Ligand Exchange mechanism (1) is most common and favoured, because the equilibrium can be driven towards the products by removing gaseous reaction products. It should also be noted that saturation of a surface during chemisorption is limited by the effects of steric hindrance and the number of accessible reactive sites of the substrate surface.[26]

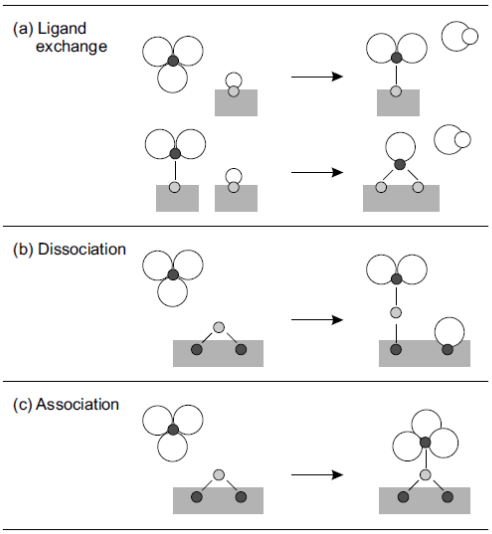

Figure 4.2: Illustration for three types of chemisorption mechanisms: A) Ligand exchange, b) Dissociation, c) Association.[28]

Since it was shown that the initial theory by Goodman and Peesa[15] was incorrect, several models have been proposed improve to the initial theory proposed in relation to the calculation of the growth of a monolayer per cycle (GPC).

The most widely used model for calculation of GPC was based on the size and number of the adsorbed ligands on the surface which was proposed by Siimon & Aarik[31] and Puurunen[26] who developed similar models independently of each other. In their model the amount of ligands that can be adsorbed is dictated either by the size (in which case steric hindrance comes into play) or by the concentration of adsorption sites (which dictates the amount of ML_z species that can be adsorbed onto the surface and hence the amount of ligands which would be present).

The effects of temperature on ALD growth should also be considered. Figure 4.3 demonstrates the temperature range for constant deposition/saturation, known as the "ALD window". In this temperature window, self-limiting growth is observed. The surface controlled mechanism is independent of the precursor pulse length, but only when the pulse length duration is sufficient to ensure saturation of the surface. When the temperature is below that required for the ALD window the precursor can condense on the surface or undergo incomplete surface reactions leading to a lower GPC. At higher

temperatures the decomposition of the precursor is possible and CVD like growth will be observed with a subsequent uncontrolled increase of the GPC. At high enough temperatures desorption of the surface species will take place with the subsequent inability for further reactions, thus lowering the GPC. In the ALD window, growth will have the required self-limiting behaviour[27,32,33]. An example of a system that displays non-ideal ALD behaviour is the growth of TiN using tetrakisdimethylaminotitanium (TDMAT) and NH_3. This happens due to incomplete surface reactions, impurities and increased porosity of the films and a change of precursor to $TiCl_4$ solves these shortcomings.[34,35,36]

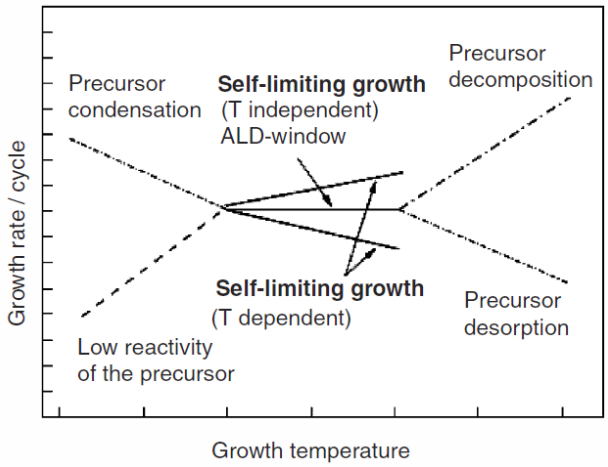

Figure 4.3: Illustration of an ALD window and the effects of temperature on the precursor reactions[3]

4.3 ALD reactor design and operation

Two types of ALD reactors are possible depending on the needs and modifications that have been carried out in the process of their construction. These two types are 1) Thermal ALD reactors and 2) Plasma-enhanced ALD reactors. A Plasma-enhanced ALD reactor was used in our study and hence will be discussed.

Thermal ALD reactors are usually separated into two types. The first is a “cross-flow” reactor, where the precursor flows horizontally through the reactor chamber. The second type is a “shower head” type reactor where the precursor is supplied through a shower

head above the sample holder. Precursors can be supplied either via evaporation from an open boat that would be present directly in the reactor or via transport of a gaseous precursor from a sealed and heated bubbler via a series of heated gas lines. The heating of the gas lines is required to prevent condensation of the precursor during transport into the reaction chamber. As in CVD there are also two variation of reactors possible, they can be either cold-wall reactors or hot-wall reactors depending on how the substrate heating is carried out. In a cold-wall reactor the substrate holder is directly heated whereas in a hot-wall reactor the heating of the reactor chamber walls is undertaken by external heating sources. The former allows for better purging times and faster cycling times whereas the latter allows for the use of precursors with a lower deposition chamber but involve longer purge times and have a larger risk of having a CVD-like component during the growth.[3]

Plasma enhanced atomic layer deposition (PEALD) or radical enhanced atomic layer deposition (REALD) is a deposition technique that is based on the production of a plasma using an applied electric field. A RF coil is used for the generation of a plasma and the creation of radicals. Plasmas are usually generated in oxygen (O_2), nitrogen (N_2) and hydrogen (H_2) gases or a combination of these. The uses of these types of plasmas allows for the replacement of the ligand-exchange reactions that are typical of the 'thermal' reagents H_2O and NH_3 used for the deposition of a variety of metal, metal nitride and metal oxide films.[37] PEALD is recognised for having the substrate either inside the plasma discharge or near it, allowing for a large flux of radicals which is an advantage. Such a close proximity to the plasma also is beneficial for the rate of the surface forming reactions as well as the surface mobility of the species due to the high ionic energies from the plasma. On the other hand, such a close proximity can lead to surface damage and contamination.

The substrate in REALD is placed further away from the plasma source so only radicals can reach the surface. This has a number of advantages and disadvantages associated with it. The advantages are related to the ability to maintain a high plasma density with low ionisation energy which minimises the surface damage and contamination as seen with PEALD. However, the energetic ion and electron bombardment which is observed

for PEALD and which provides additional energy for surface forming reactions and mobility of surface species is no longer observed and therefore the rate-forming reactions are determined by precursor reactivities and by-product desorption as seen in thermal ALD.[38]

References:

1) V. Miikkulainen, M. Leskelä, M. Ritala, R. L. Puurunen, *J. Appl. Phys*., **2013**, 113, 21301.
2) M. Leskelä, M. Ritala, *Thin Solid Films*, **2002**, 409, 138–146.
3) A. C. Jones, M. L. Hitchman, *Chemical Vapour Deposition: Precursors, Processes and Applications*, *Chapter 4: Atomic Layer Deposition*, First Ed, RSC, **2009**.
4) T. D. Manning, I. P. Parkin, *Polyhedron*, **2004**, 23, 3087–3095.
5) A. A. Malygin, S. D. Dubrovenskii, *Russ. J. Gen. Chem*., **2010**, 80, 643–657.
6) A.A Malygin, *J. Ind. Eng. Chem*., **2005**, 12, 1–11.
7) T. Suntola, J. Antson, U.S. Patent No. 4,058,430, **1977**, 15.
8) J. K. Furdyna, R. L. Aggarwal, S. von Molnar, *Mat. Res. Soc. Symp. Proc*., **1995**, Vol 89
9) J. Nishizawa, *Surf. Sci*., **1987**, 185, 249–268.
10) M. A. Herman, *Vacuum*, **1991**, 42, 61–66.
11) S. M. George, A. W. Ott, J. W. Klaus, *J. Phys. Chem*., **1996**, 100, 13121–13131.
12) J. Nishizawa, *Surf. Sci*., **1987**, 185, 249–268.
13) A. Usui, H.Watanabe, *Annu. Rev. Mater. Sci*., **1991**, 21, 185–219.
14) T. Suntola, *Mater. Sci. Reports*, **1989**, 4, 261–312.
15) C. H. L. Goodman, M. V. Pessa, *J. Appl. Phys*., **1986**, 60, R65.
16) M. Pessa, P. Huttunen, M. A. Herman, *J. Appl. Phys*., **1983**, 54, 6047–6050.
17) M. Ritala, M. Leskelä, *Nanotechnology*, **1999**, 10, 19–24.
18) K. Xu, D. Chen, F. Yang, Z. Wang, L. Yin, F. Wang, R. Cheng, K. Liu, J. Xiong, Q. Liu, *Nano. Lett*., **2017**,
19) M. Leong, B. Doris, J. Kedzierski, K. Rim, M. Yang, *Science*, **2004**, *306*, 2057–2060.

20) F. Zaera, *J. Mater. Chem*., **2008**, 18, 3521.
21) M. Leskelä, M. Ritala, *Angew. Chem. Int. Ed. Engl*., **2003**, *42*, 5548–5554.
22) T. Alasaarela, T. Saastamoinen, J. Hiltunen, A. Säynätjoki, A. Tervonen, P. Stenberg, M. Kuittinen, S.Honkanen, *Appl. Opt*., **2010**, 49, 4321–4325.
23) E. Østreng, K. B. Gandrud, Y. Hu, O. Nilsen, H. Fjellvåg. *J. Mater. Chem. A*, 2014, 2, 15044–15051.
24) X. Chen, H. Zhu, Y. Chen, Y. Shang, A. Cao, L. Hu, G. W. Rubloff, *ACS Nano*, **2012**, 6, 7948–7955.
25) H. Kim, H. B. R. Lee, W.J. Maeng, *Thin Solid Films*, **2009**, 517, 2563–2580.
26) R. L. Puurunen, *Chem. Vap. Deposition*, **2003**, 9, 249–257.
27) S. M. George, *Chem. Rev.*, **2010**, 110, 111–131.
28) R. L. Puurunen, *J. Appl. Phys*., **2005**, 97, 121301–121301.
29) J. Aarik, A. Aidla, H. Mändar, T. Uustare, *Appl. Surf. Sci.*, **2000**, 172, 148-158
30) R. L. Puurunen, *Chem. Vap. Deposition*, 2005, 11, 79-90
31) J. Aarik, H. Siimon, *J. Phys. D: Appl. Phys*., **1997**, 30, 1725–1728.
32) T. Suntola, *Appl. Surf. Sci*., **1996**, 100/101, 391–398
33) L. Niinisto, M. Nieminen, J. Paivasaari, J. Niinisto, M. Putkonen, *Phys. Status. Solidi*., **2004**, 201, 1443–1452.
34) J.-S. Min, Y.-W. Son, W.-G. Kang, S.-S. Chun, S.-W. Kang, *Jpn. J. Appl. Phys*., **1998**, 37, 4999–5004.
35) J.-W. Lim, H.-S. Park, S.-W. Kang, *J. Electrochem. Soc*., **2001**, *148*, C403–C408.
36) M. Ritala, E. Rauhala, *J. Electrochem. Soc*., **1995**, 142, 2731–2737.
37) H. B. Profijt, S. E. Potts, M. C. M. van de Sanden, W. M. M. Kessels, *J. Vac. Sci. Technol. A*, **2011**, 29, 50801.
38) A. Niskanen, *Radical Enhanced Atomic Layer Deposition of Metals and Oxides*, **2006**, University of Helsinki (Thesis)

Chapter 5: Analytical Methods

5.1 Scanning Electron Microscopy

Generally, scanning electron microscopy (SEM) imaging is used materials science for rapid morphological and topographical characterization of samples. In order to avoid charging and therefore obtain good quality, high resolution images samples must be electrically conductive. Non-conductive samples are typically sputtered with gold to facilitate image collection. A schematic of a typical scanning electron microscope is presented in figure 5.0

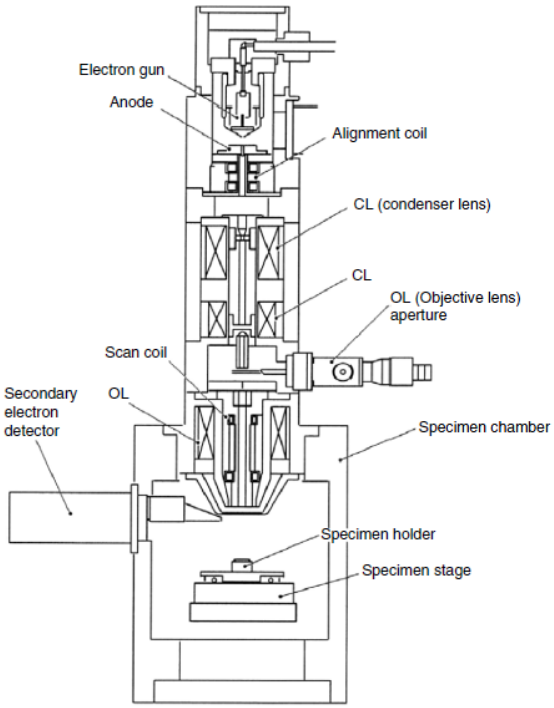

Figure 5.0: Diagram of scanning electron microscope (an FEI Quanta 650 FEG SEM was used in the analysis).[1]

The system operates in the following manner: A filament on top of the system, which is also known as the electron gun, is heated. It is located on top of the microscope column and it generates primary (1°) electrons by thermionic emission, which are used for the

actual sample imaging. The electron beam then passes through a series of electromagnetic lenses and coils which control the size, shape and position of the primary electrons. The primary electrons enter the specimen and eventually hit the nucleus of a particle in the specimen and scattering will occur. When this occurs a reaction vessel in the form of a tear drop is formed where scattering effects take place as shown in figure 5.1. The size of the vessel depends on the accelerating voltage, atomic density and surface topography.

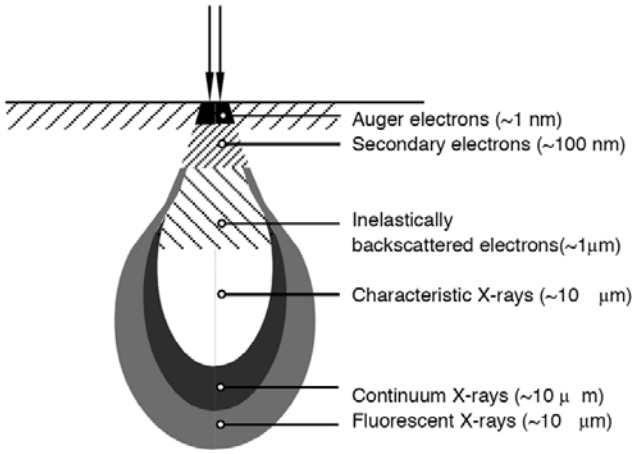

Figure 5.1: Diagram of the processes happening in the reaction vessel[2]

The following events occur in the reaction vessel as seen in figure 5.1.1:

First of all, backscattered electrons are produced. These are the original primary electrons that have been scattered in such a way that they do not go through the specimen and retain much of their energy. Secondary electrons (2°) are produced when an electron is removed from the specimen by primary electrons. These are very low energy and can only be detected near the surface. X-rays and Auger electrons are generated when inner shell electrons are ejected by primal electrons and an electron from a higher energy state drops down to the vacant energy level. Excess energy is given off in the form of x-rays or it kicks out an outer shell electron to give Auger electrons. X-rays can give data about the elemental composition.

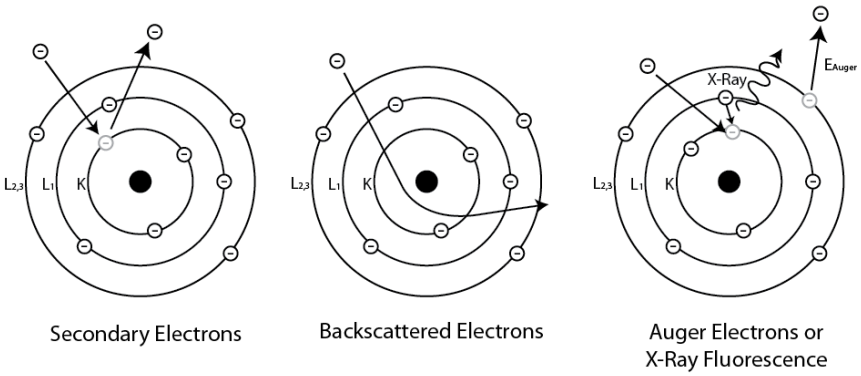

Figure 5.1.1: Electron and X-ray emission model[2]

The stage on which the specimen lies is adjustable and can be rotated, moved and tilted in the x, y and z directions to allow viewing from different perspectives. There are several detectors present which allow for the detection of different energy emissions or particle emissions. The entire system is kept under vacuum to prevent oxidation and to prevent primary electrons interacting with other particles. Sometimes during the analysis of a non-conductive or poorly conductive sample the electrons with which the sample is illuminated will collect on the surface and cause it to glow in the SEM - this is a phenomena known as “charge-up” which will cause problems with contrast and image deformation. In such cases a sample must be coated with a conductive metal like gold before analysing the sample.[1,3] An FEI Quanta 650 FEG SEM was used in the analysis.

5.2 X-Ray Diffraction

Röntgen’s discovery of X-rays in 1895 changed the way analysis is done in many fields of modern day life, from medicine to chemistry and the importance of X-rays cannot be doubted. In solid state and materials chemistry X-rays have allowed scientists to utilise a method for the fingerprint characterisation of crystalline materials and determination of their structure.[4]

It has been known from a very early stage that radiation can undergo diffraction if it is scattered coherently from a periodic array of objects. Max Von Laue, a famous German physicist, was the first to mention the diffraction of X-rays. Sometime later in 1913 William Henry Bragg and his son William Lawrence Bragg developed what is nowadays known as Braggs Law, which explained why cleavage faces of crystals appear

to reflect X-ray beams at certain angles of incidence. It allowed for the development of X-ray diffraction which works on the basis of a sample being irradiated by X-ray beams. The beams mostly pass through or are reflected by a sample, but at times beams are reflected in phase from two planes in which (as dictated by Snell's law) the angle of incidence is the same as the angle of reflection. While being in phase the wave in the second plane will have to travel a distance which is ABC further than the top plane and similarly for the third plane as shown in figure 5.2. Hence the waves in the second and third planes will be phase retarded with respect to the first, causing interference. For constructive interference to occur the distance ABC will have to be equal to one wavelength (λ) and hence DEF will be equal to (2λ). This in turn allows all the reflections to emerge in phase and be visible as diffraction.[5]

This is proposed by Bragg's Law and is described by Equation 3.0: [6]

$$n\lambda = 2dsin\theta \quad \text{(Equation 3.0)}$$

where *n* is an integer, λ is the wavelength of the incident X-ray beam, *d* is the distance between the atomic layers in a crystal and θ is the angle of incidence.

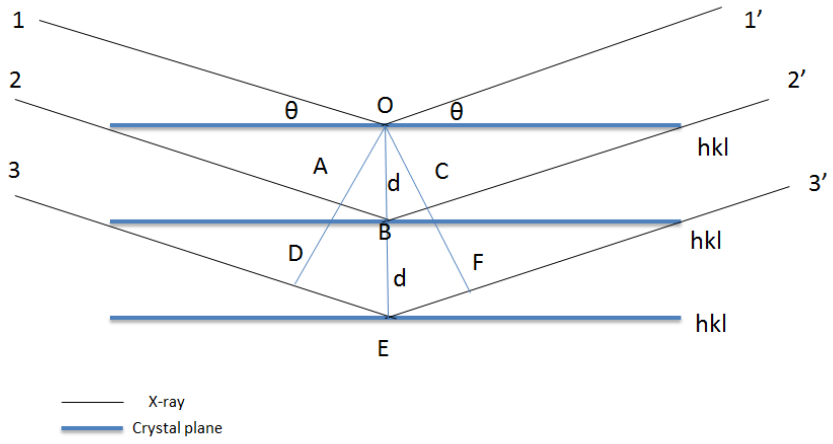

Figure 5.2**:** Illustration of the Bragg equation

5.3 Raman spectroscopy

Raman spectroscopy is an analytical technique used for structural characterisation on an atomic level of a material utilizing the principle of interaction of light and matter. Photons of light come in contact with a molecule with a chance of either absorption or scattering to occur. For infrared absorption to occur several conditions are required. The incident photon has to have an energy equal to the energy difference between the ground and excitation states of a molecule and a change of dipole moment must occur during the transition between the two states. If these conditions are not fulfilled the photon will be scattered. Several types of scattering are possible. If a photon is scattered elastically in a way that energies of the photon and molecule are the same, it is considered to be Rayleigh scattering. If this is not the case and if molecular vibrational motion occurs, it will lead to an energy transfer between the photon and the molecule which in turn means that the energies of the two would no longer be the same. This leads to inelastic scattering which is also known as Raman scattering. There are two types of Raman scattering known as Stokes and anti-Stokes. Both involve the transfer of energy and excitation to a virtual state which is lower in energy than a real electronic transition. The two types of scattering differ on whether energy is lost or gained in regard to the incident photon. In the case of Stokes scattering the energy is transferred from the incident photon to the molecule and hence the photon will be of a lower energy and have a longer wavelength. In the case of the anti-stokes the energy is transferred from the molecule to the photon and hence it would be of greater energy. Both phenomena are portrayed in Figure 5.3.

A typical Raman spectrum is usually plotted as the Raman shift which is the difference versus the intensity.

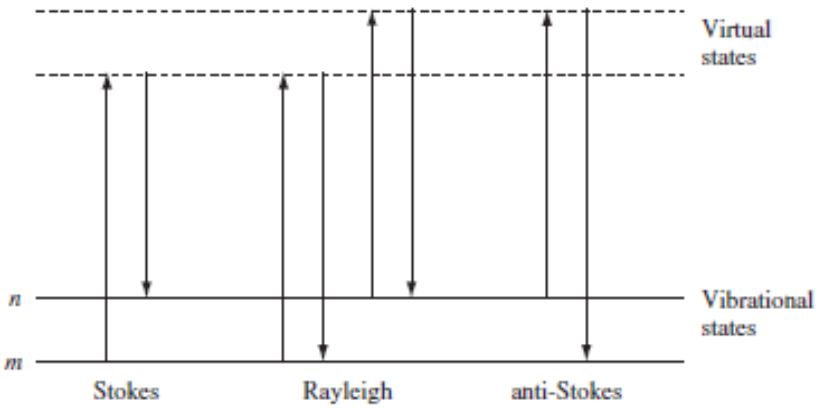

Figure 5.3: Energy level diagram depicting Rayleigh scattering and Stokes/Anti Stokes Raman scattering.[7]

5.4 X-ray photoelectron spectroscopy

X-ray photoelectron spectroscopy (XPS) is a surface analytical technique which is based on the photoelectric effect. It is used to determine the composition of the surface of a material as well as the oxidation states of individual atoms. It is used because it has a high detection limit, it can detect all elements except hydrogen and helium, it is able to analyse insulators, define the empirical formula and is a non-destructive technique. Although it is non-destructive some ion milling is required to remove surface contaminants and oxides which can cause some surface degradation.[8]

Typical XPS equipment consists of an X-ray source, a lens system to focus and transfer the ejected photoelectrons, an electron energy analyser which measures the energy of the ejected photoelectrons and an electron multiplier detector. XPS works on the basis that X-ray photons (hv) are used to induce the excitation of atoms on the surface of the analysed sample to a depth of up to 12 nm and the ejected photoelectrons are then detected as seen in figure 5.4. The photoelectrons are ejected from the inner orbitals around the nuclei of the atoms and are characteristic of the corresponding species. The ejected photoelectrons have a combination of the kinetic energy of the X-ray and the kinetic energy of the ionised atom at the final state. Once the core electron has been

removed a vacancy is formed which is filled by an electron from a higher energy level which is accompanied by a release of energy in the form of an Auger electron. The detector measures all of the kinetic energy that both photoelectrons and Auger electrons contain once they are ejected from the surface after excitation.

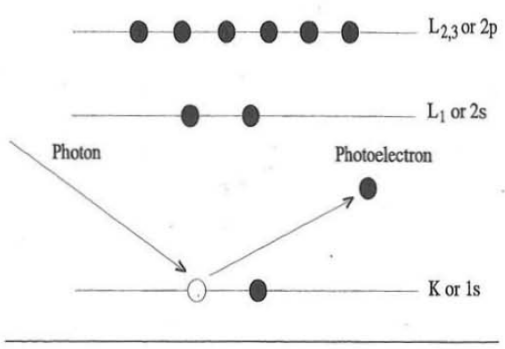

Figure 5.4: Example of excitation of an atom using a photon leading to the ejection of a photoelectron from the valence band.[8]

The kinetic energy can be calculated from the following equation:

$$KE = hv - BE - \Phi_{spec}$$ (Equation 3.1)

where KE = electron kinetic energy, hv = x-ray photon, BE= electron binding energy, Φ_{spec} = spectrometer work function.

Spectral lines observed in the XPS are identified according to the binding energies of specific electron orbitals that are specific for different atoms. The electron binding energy (BE) is part of equation 3.2 mentioned above and is the measure of the amount of energy that is required to dislodge a photoelectron from the orbital of an atom. The binding energy strongly depends on the elements analysed, the type of orbital from which the electron originates and the chemical environment of an atom. The BE can be calculated using the following formula:

$$BE = hv - KE - \Phi_{spec} - E_{ch}$$ (Equation 3.2)

where E_{ch} is the surface charge energy which can be determined by electrically calibrating the instrument to a spectral feature of C1s or $Au4f_{7/2}$.

The change in the binding energy of the core electron of an element is known as a chemical shift[9] and can happen due to change in chemical bonding, electrostatic shielding and withdrawal/addition of valence electron charge. Determining the chemical shifts allows establishing the functional groups and oxidation states of analysed materials. There are however some limitations when using XPS, including a very small analysis area, long scan time and the maximum detection limit of only 100ppm.

5.5 Cyclic Voltammetry

The analysis of electrochemical properties of different materials can be carried out in several ways. During one, the measurement of potential across two electrodes is carried out and during the other the flowing current is measured - these are known as potentiometry and amperometry respectively. In the case of the potentiometric measurement the current is very low, a reaction between a working electrode and the electrolyte will take place and a reference electrode will have a fixed potential. In the case of the latter, a potential applied to the working electrode is swept at a constant sweep rate and the current is measured as a function of potential – this is known as voltammetry. Voltammetric experiments can be used to obtain information about concentrations, redox potentials, equilibrium constants and rate constants in systems where redox chemistry takes place.[10]

Cyclic voltammetry as an analytical technique was first mentioned in a publication by B. Randles in 1947[11]. In cyclic voltammetry a linear voltage is swept to a maximum and a minimum voltage limit across a working electrode at a specific known rate, giving rise to a triangular potential waveform as seen in figure 5.5. As can be seen from the image, as soon as a maximum voltage limit (Forward Scan) is reached it is reversed and swept back to the minimum (Reverse Scan). This is done while the potentiostat measures the electrode current which is results from the applied potential and a voltammagram is then generated as seen in figure 5.5.1.[12]

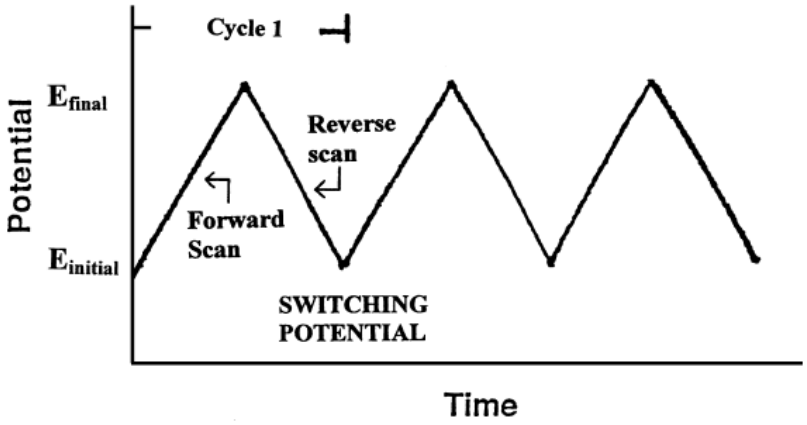

Figure 5.5: Cyclic Voltammetry potential waveform observed upon cycling.[13]

The reactions that take place can be redox reactions and can be reversible or irreversible. The formation of irreversible phases is accompanied by loss of current and leads to the working electrode being no longer usable. The current will also vary with variable scan rate, as can be seen in figure 5.5.1, which can also influence the reversibility/irreversibility of the redox reaction.[14]

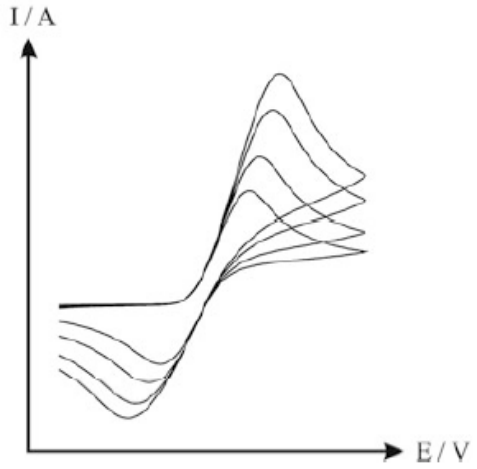

Figure 5.5.1: Example of effect of varying scan rates on cyclic voltammograms peak potential.[12]

References:

1) W. Zhou, R. P. Apkarian, Z. L. Wang, D. Joy, *Scanning Microscopy for Nanotechnology: Fundamentals of Scanning Electron Microscopy*, *Chapter 1*, Springer-Verlag, **2007**

2) M. Dewar, *Characterization and Evaluation of Aged 20Cr32Ni1Nb Stainless Steels*, **2013**. University of Alberta, (Msc Thesis)

3) J. Goldstein, D. Newbury, D. Joy, C. Lyman, P. Echlin, E. Lifshin, L. Sawyer, J. Michael. *Scanning Electron Microscopy and X-Ray Microanalysis*, *Chapter 12*, 3rd Ed, **2007**.

4) J. J. Friel. *X-Ray And Image Analysis In Electron Microscopy*, 2nd Ed, **2003**.

5) R. Jenkins, R. Snyder, *Introduction to X-Ray Powder Diffractometry*, Wiley, **2012**.

6) C. G. Pope, *J. Chem. Edu.*, **1997**, 74, 1, 129-131

7) E. Smith, G. Dent, *Modern Raman Spectoscopy - A Practical Approach*, *Chapter 1*, John Wiley & Sons, **2005**.

8) J. F. Moulder, W. F. Stickle, P. E. Sobol, K. D. Bomben, *Handbook of X-ray Photoelectron Spectroscopy*, *Chapter 1*, Perkin-Elmer, **1992**

9) S. Tougaard, *Surface Analysis – X-Ray Photoelectron Spectroscopy*, Encyclopedia of Analytical Science, 2nd Ed, **2005**, 446-456

10) A. B. Bocarsly, *Cyclic Voltammetry Characterization of Materials*, **2012**, 1–14

11) J. E. Randles, *Chem. Insp. Dep. Minsitry Supply*, **1947**, 322–327. (Patent).

12) D. A. C. Brownson, C. E. Banks, The Handbook of Graphene Electrochemistry, Chapter 2, Springer-Verlag London, **2014**

13) J. Wang, *Analytical Electrochemistry*, *Chapter 2*, 2nd Ed, **2000**.

14) G. A. Mabboil, *J. Chem. Edu.*, **1983**, 60, 697–702.

Chapter 6: Evaluation of un-doped V_2O_5 films grown by CVD

As mentioned previously in chapter 1, much work has been done on the study of vanadium pentoxide because of its electrochromic properties and potential for battery materials. The work in this chapter focuses on the development of a method for the growth of high quality nominally un-doped vanadium pentoxide films using aerosol-assisted chemical vapour deposition (AACVD) using vanadyl acetylacetonate as the precursor. The effects of growth temperature and duration on the quality and properties of the films were studied. Film morphology, crystallinity, electrical and optical properties are discussed and compared.

6.1 Material growth

The growth of V_2O_5 was carried out using a home built AACVD reactor a schematic of which is illustrated in figure 6. The 0.1 mol dm^{-3} precursor solution used for film deposition was made up from 98% vanadyl(IV)acetylacetonate ($VO(acac)_2$) (Sigma-Aldrich) in methanol. A polypropylene laboratory bottle acted as a bubbler after modification with stainless steel fittings, which enabled the connection of the gas supply and reaction chamber. A sonicator plate was used as the aerosol generator with a gas handling system to regulate the flow of the carrier gas, which in this case was nitrogen. The above mentioned system consisted of a carrier gas source, flow meter and a control unit for the flow meter. The use of these allowed for precise and easy control of carrier gas flow. The aerosol was swept into the reaction chamber using the nitrogen carrier gas at 5 dm^3min^{-1}, which was heated by a hot-wall furnace. Films were deposited on fluorine doped tin oxide (FTO) coated plate glass with sheet resistance 8-10 Ωsq^{-1} (Sigma-Aldrich). Any unreacted precursor was removed via the exhaust. A series of films were prepared by varying the temperature and time of growth.

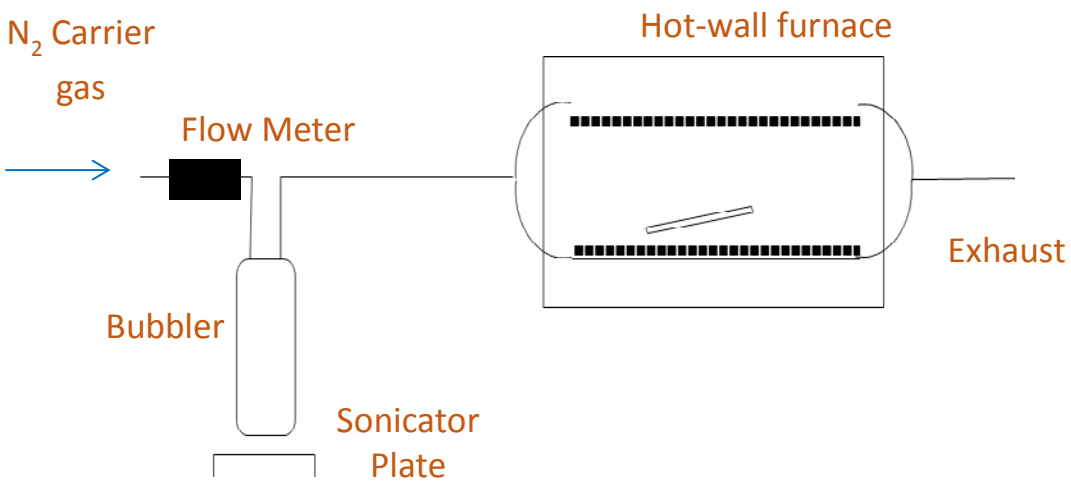

Figure 6: AACVD deposition apparatus consisted of: N_2 carrier gas source, Flow Meter, Bubbler containing the precursor, Sonicator plate, Reactor tube, Hot-wall Furnace and Exhaust.

From the literature and preliminary growth tests it was established that the most suitable growth temperature was 400°C. Growth at this temperature avoided solvent droplets reaching the substrate and particle formation. A post annealing step for three hours at 600°C in air was also employed to improve sample crystallization and remove sub-oxides as only partial oxidation could be achieved due to the influence of the solvent breakdown and nitrogen flow rate[1,2,3]. For all subsequent experiments the temperature was kept constant and the growth time varied from 15-60 minutes. Examples of annealed films can be seen in figure 6.1. The samples were of a yellow colour when annealed and passed the Scotch tape test. They were found to be resistant to the electrolyte solution ($LiClO_4$/propylene carbonate) and in the case of the 60-minute sample, with an anneal, properties were retained after six months indicating long term stability of the films. As can be seen, samples with lower growth times suffered from incomplete and non-uniform surface coverage, which had a direct impact on the electrical and optical properties of the films. More detailed explanation of results and analytical techniques can be found in the following sections.

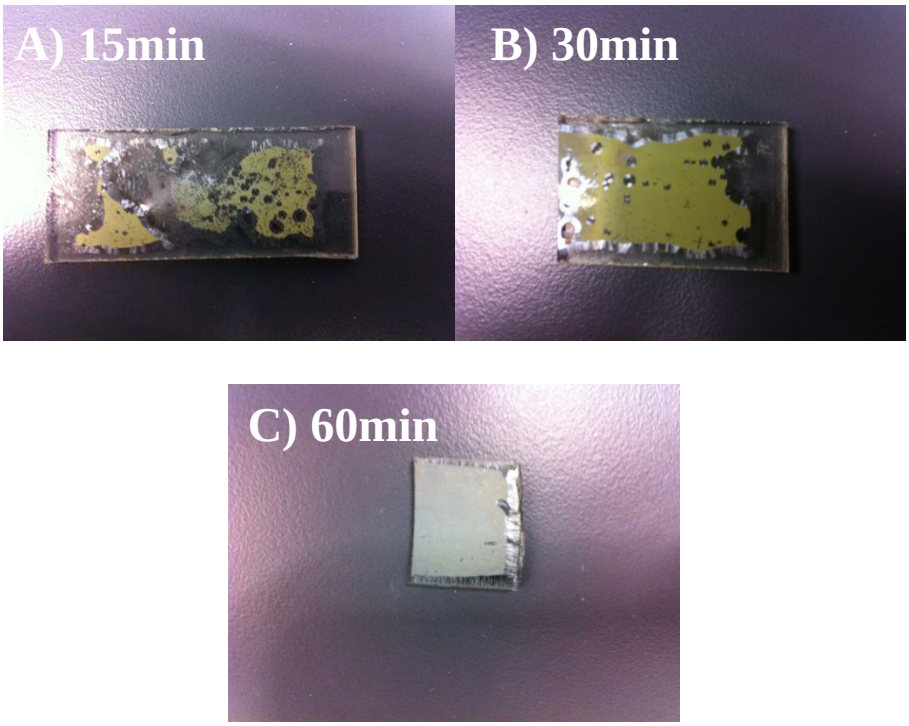

Figure 6.1: Samples grown on FTO for A) 15 min B) 30 min C) 60 min at 400°C and annealed for 3h at 600°C

6.2 Morphology

Analysis by scanning electron microscopy (SEM) was carried out on annealed samples to determine the effects of growth time on their morphological characteristics. Scanning electron microscopy analysis was performed using a Jeol JSM-6390LV system. All samples were gold coated to avoid surface charging.

Analysis of the annealed films showed that the surface was covered by distinct pellet-like structures as seen in figures 6.2. Lower growth times of 15 and 30 minutes suffered from incomplete surface coverage as seen in figure 6.1 with gaps being present in between the pellets as seen in figure 6.2. Upon increasing the growth times, the surface coverage became more complete. Similar surface structures to those mentioned previously were observed for 45 and 60 minute growths. Pellet-like structures were observed to be orientated in plane with the substrate surface. Overall thickness values, table 6, were similar to those previously reported by Field and Parkin.[4]

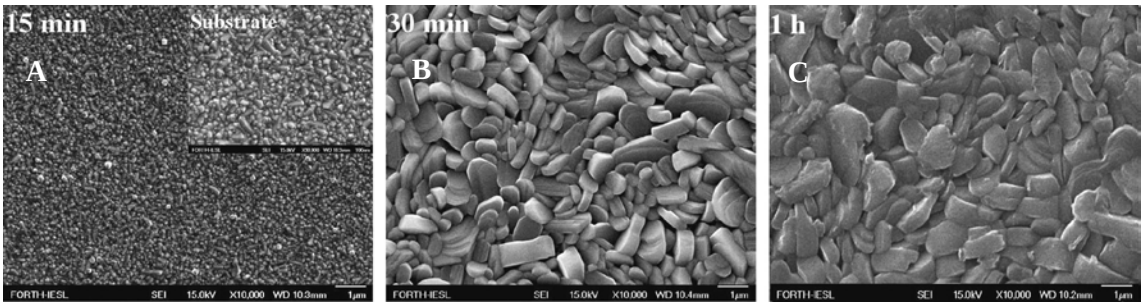

Figure 6.2: SEM of samples grown at 400°C for (A) 15 min (insert is plain FTO substrate) (B) 30 min (C) 1h. All annealed for 3h at 600°C. Large platelet structures formed on the surface of (A), (B) and (C). Note that at the lower growth durations incomplete surface coverage and gaps in the crystallite coverage were evident.

400 °C			
Time (min)	15	30	60
Thickness (nm)	328.3	580.6	1024.4

Table 6: Thickness values for samples grown for 15, 30 and 60 min at 400 °C

Annealed for 3h at 600 °C

6.3 Crystallography

Having examined the surface morphology an understanding of the types oxide which are present was also required. It was paramount that the films grown were V_2O_5 as the presence of sub-oxides could directly impact on the electrochemical properties of the films. Hence, X-ray diffraction analysis was carried out. Analysis of the coatings was carried out using a Siemens D5000 Diffractometer with the following operation parameters: 2θ = 10.0-50.0°, step size 0.05° and step time 3s. The major peaks are labelled in figures 6.3 and 6.3.1. XRD data from samples grown for the duration of 15 and 30 min is presented in figure 6.3.

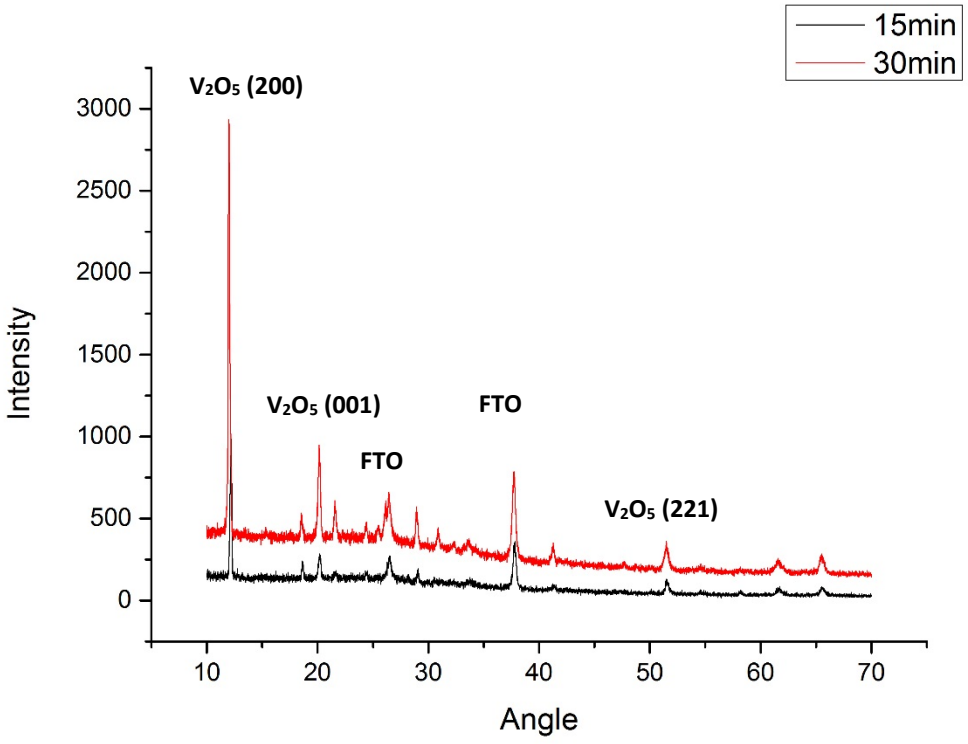

Figure 6.3: XRD of samples grown at 400°C for: (black)-15 min, (red)-30 min, annealed at 600°C for 3h

Films grown for 15 minutes were observed to contain multiple low intensity V_2O_5 peaks along with the peak corresponding to the (200) plane of V_2O_5 at 12.3^o as was seen in the above mentioned results. Peaks at 20.1^o, 21.5^o, 32.3^o, 33.6^o 41.2^o, 51,4^o and 61.6^o correspond to low intensity V_2O_5 peaks mentioned previously and are assigned to (001), (101), (301), (011), (002), (221) and (402) planes respectively corresponding to the reference code (89-0612). A peak at 31.1^o was also observed which was attributed to V_3O_7 and assigned to the (-312) plane corresponding to the reference code (20-1378). On increasing the growth time to 30 minutes a new peak at 32.4^o was also noticed, which was assigned to the (410) plane of V_3O_7. Peaks corresponding to the FTO substrate were also detected at 24.4^o, 25.4^o, 37, 8^o, 51.5^o, 65.5^o corresponding to (101), (110), (200), (220) and (301) planes respectively corresponding to reference code (77-0452).

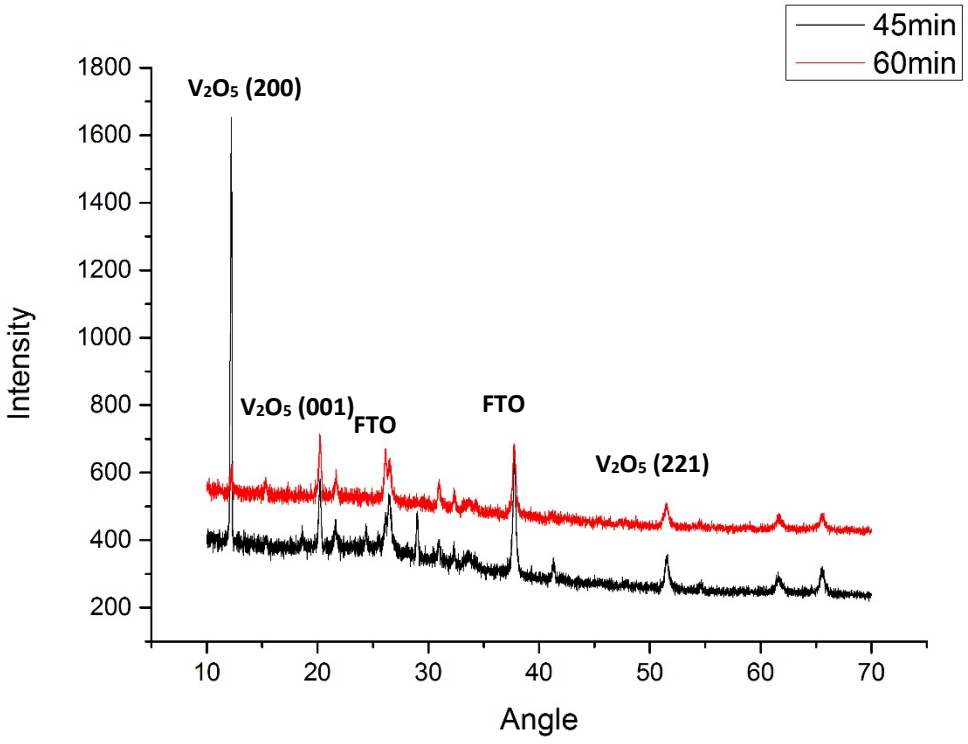

Figure 6.3.1: XRD of samples grown at 400°C for: (black)-45 min, (red)- 60 min, annealed at 600°C for 3h

XRD data from samples prepared using 45 and 60 minute growths are presented in figure 6.3.1. Films were grown at 400°C as before with the same annealing time and temperature. As in figure 6.3 similar peaks were observed, with the addition of a new low intensity peak at 26.1^{o} which was assigned to (110) V_2O_5 corresponding to reference code (41-1426). The increase of the growth time to 60 minutes led to a greater degree of orientation preference for the monoclinic β-V_2O_5 and allowed the rectification of the issue of patchiness and non-uniformity.

Separate analysis was carried out on the grown samples three months later and identical results to those presented above in figure 6.3.2 were found. A high intensity monoclinic β-V_2O_5 (200) peak[5] was observed as per initial analysis indicating formation of the desired orientation and good samples stability.

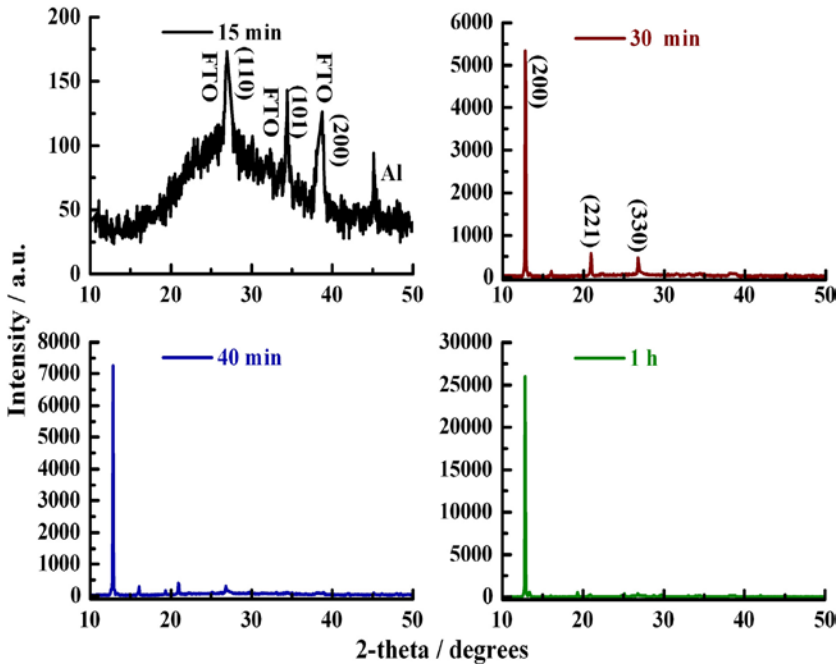

Figure 6.3.2: XRD of samples grown at 400°C for: (black)-15 min, (red)-30 min, (blue)-40 min, (green)-60 min. All samples annealed at 600°C for 3h (Aluminium peak due to substrate holder)

6.4 Electrochemical Characterization

Electrochemical characterization was carried out in a 1M, $LiClO_4$/propylene carbonate solution relative to a silver/silver chloride reference electrode. The scan rate was varied at 2, 5, 10, 20, 30, 40, 50, 75, 100, 150 and 200 mVs^{-1} through a voltage range of -1V to +1V over scans of 1 and 500 cycles. The area of the working electrode (in the form of the FTO substrate with the grown V_2O_5 film) was $1cm^2$. Li ion intercalation/deintercalation was studied using chronoamperometry at -1V and +1V for steps of 200s.

In this section the electrochromic and electrochemical properties of the grown films will be discussed. Vanadium pentoxide has been of interest to researchers as a potential cathode material for lithium ion batteries as well as for smart windows due to its unique structure and properties.

The electrochemical testing of the samples was carried out using a three-electrode electrochemical cell as seen in figure 6.4. The most promising samples were chosen and tested by means of electrochemical measurements and the results discussed and compared to literature values. The measurements were done by a collaborating group from the technological institute of Crete, operating in the center of materials technology and photonics. All of the electrochemical data for the analysis in this thesis was provided by this group. The measurements that were performed were: cyclic voltammetry, current density vs square root of the scan rate and chronoamperometry measurements. Cyclic voltammetry (CV) measurements were performed, with a scan rate of 10 mV/s over the voltage range of -1V to +1V over scans of 1 and 500 cycles. When a CV sweep is done a potential range is set and is gradually applied to the working electrode to slowly change the potential, once it reaches a maximum it then reverses the scan to return to the original potential. During the process the current resulting from the applied potential is measured and is plotted as current density vs applied potential as seen if figure 6.4.1.

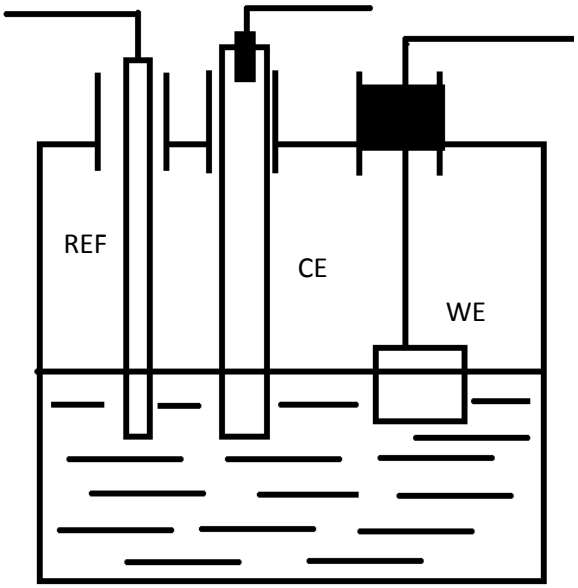

Figure 6.4: Diagram of a three electrode electrochemical cell containing the electrolyte, working, counter and reference electrodes.[6]

Samples exhibit three redox couples corresponding to phase transitions of $Li_xV_2O_5$ between the α, ε, δ, γ which are similar to those observed for α-V_2O_5[7]. These phase transitions correspond to colour changes from yellow to green to light blue[8]. The cathodic peaks for the 1h samples at 0.220V, -0.177V and -0.553V correspond to α/ε, ε/δ and δ/γ phase transitions respectively as seen in other works[9]. The anodic peaks for the 1h samples at -0.194V, 0.013V and 0.357V correspond to the reverse of the transitions mentioned above i.e. the γ/δ, δ/ε and ε/α phase transitions respectively. For samples grown for 40 minutes a peak shift is observed for the two very broad cathodic and anodic peaks which might correspond to α/ε, ε/δ and ε/α, δ/ε phase transitions. The broadness of the peaks is indicative of the poor stability of the sample due to the surface passivation and structural transformation. This happens due to the fact that the surface becomes amorphous upon cycling and undergoes increased structural disorder[9]. The process of intercalation/deintercalation can lead to mechanical stress either because of changes in the molar volume of the material or due to the distortion of the crystal lattice [10,11] Samples grown for the duration of 1h sample as seen in figure 6.4.1 show the best maximum current density values of 1.26 $mAcm^{-2}$ compared to 0.25 $mAcm^{-2}$ and 0.1 $mAcm^{-2}$ for 40 min and 30 min respectively. Such a difference is indicative of a greater amount of lithium ions being intercalated/deintercalated. As it is clearly seen the 1hour sample undergoes the same irreversible structural transformations to the γ-phase and ω-phase and surface passivation as with the other samples mentioned previously. The poor stability of these samples is illustrated in the inset of figure 6.4.1 showing the comparison between the 1st and 500th cycles for the 1hr sample. Capacity fading takes place as can be seen from the decrease of values from 1.26 $mAcm^{-2}$ to 0.27 $mAcm^{-2}$. Analysis of the 15 minute samples did not yield any electrochemical data due to the discontinuous nature of the film as seen in sections 6.11 and 6.2.

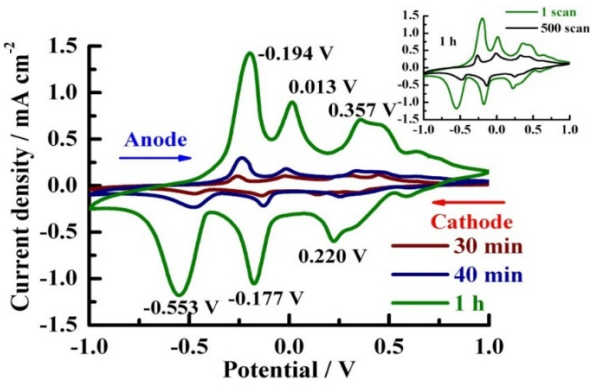

Figure 6.4.1: Cyclic Voltammogram of the first scan for samples grown at 400C° for 30, 40 and 60 min. Annealed for 3h at 600C°. Inset is CV of the 1st and 500th scan of the 60 min sample.

Figure 6.4.2 shown the relationship between the square root of scan rate and the current density for the anneal V_2O_5 samples. The 1h sample had a linear relationship between the current density and square root of the scan rate indicating that the electrochemical process is diffusion controlled[12]. The relationship is governed by the charge transfer at the electrode/electrolyte interface and by the rate-limiting step of Li^+ diffusion in the electrode.[12] The rate increase of the current density for the 1h sample was the highest and had a value of 0.7 mA/cm^{-2} at 10 mVs^{-1} which was comparable to Sn-doped V_2O_5 films grown by sol-gel[13]. As was proposed by Tong et al. the diffusion distance has a major impact on the electrochemical performance of the films and in the case of dense films is dependent on the thickness of the films.[6] A flat response was obtained for other samples indicating poor intercalation/deintercalation with very small current density values.

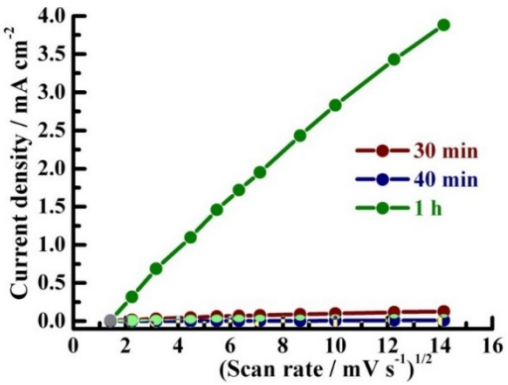

Figure 6.4.2: Plot of current density (mA/cm^2) versus square root of the scan rate varying between 2-200 (mVs^{-1})$^{1/2}$ for samples grown at 400C° for 30, 40 and 60 min, annealed for 3h at 600C°

Chronoamperometry measurements were carried out on the 30min, 40min and 1h samples as seen in figure 6.4.3. Again the sample grown for the duration of 1h demonstrated the best results, compared to the lower growth time samples, giving a time response of 12±1 and 10±1 for intercalation (colouration) and deintercalation (bleaching) respectively which is fast when compared literature values where V_2O_5 films were deposited by sol-gel (100s)[14] or r.f sputtering (150s)[15]. The 30 min sample for example showed results which were twice of the above mentioned, indicating a slower time response. On the other hand, the 500th scan of 1hr sample demonstrates significant current density reduction illustrating electrochemical instability due to non-reversible structural alterations which are brought about by phase changes to the γ and ω phases[16].

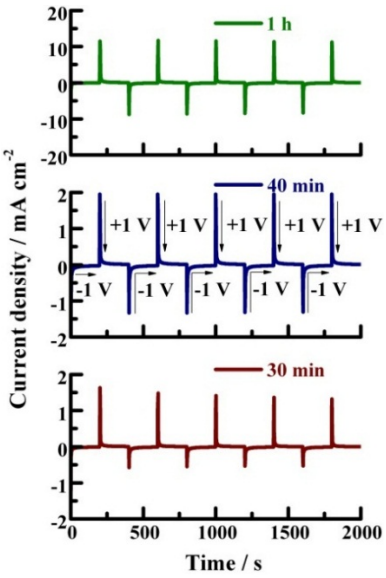

Figure 6.4.3: Chronoamperometric analysis at a potential step of -1V and +1V for a time step of 200s for samples grown at 400C° for 30, 40 and 60 min, annealed for 3h at 600C°

6.5 Electrochromic Characterization

Since a key application of vanadium oxide is an electrochromic coating on windows, the transparency and optical density of the films is a key factor which should be taken into account. Due to this reason, ex situ visible and NIR transmittance spectra were done. Transmittance spectra of annealed samples grown for 30, 35 and 60min in the coloured (-1V) and bleached (+1V) states are presented in figure 6.5. Percentage Transmittance (%T) values of the coloured and bleached states were recorded at 650 and 900nm and the differences in transmittance (ΔT) between the samples were compared. It was found that the highest values of (ΔT) were for the 1h sample, resulting in 27% and 17% transmittance at 650 and 900nm respectively. This was followed by 5% and 14% for the 40min sample and 3% and 9% for the 30min sample. The values for the 1h sample are comparable to V_2O_5 films randomly stacked with V_2O_5 nanowires which gave (ΔT) results of ~ 20%.[17]

For the estimation of optical density equation 4 was used:

$$\Delta OD_{\lambda} = \log(\frac{T_{b\lambda}}{T_{c\lambda}})$$ (Equation 4)

Where $T_{b\lambda}$ and $T_{c\lambda}$ are expressions of the bleached (+1V) and coloured (-1V) states respectively. The optical modulation for the 1h sample was found to be 0.3 at 650nm, this value is in close approximation to those reported in literature for dense films.[7] Even though the 1h samples showed the best results overall the transmittance was too low to be of use in electrochromic windows. This was due to the films needing to be thicker to ensure good films coverage and an improvement on that part will have to be made.

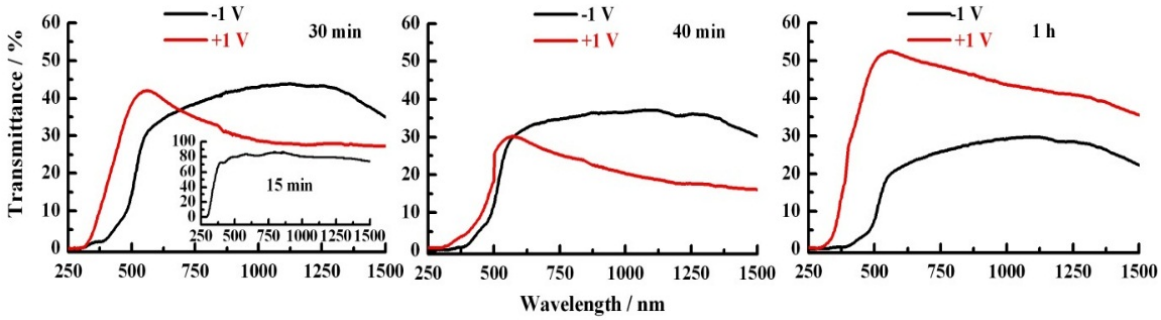

Figure 6.5: Transmittance spectra of annealed coatings grown for 30, 40 and 60 min in the coloured (-1V) and bleached states (+1V)

6.6 Summary

In this chapter a study on the growth of V_2O_5 films by AACVD was carried out, and optimal parameters for the growth of suitable V_2O_5 films by AACVD were determined. Film growth was carried out at temperature of 400°C, whereas the annealing step required a furnace temperature of 600°C to stimulate the formation of V_2O_5 phase films and to eliminate the majority of other sub-oxides. Growth times were varied between 15min to 60min and it was found that longer growth times gave thicker and more uniform films. Thinner films suffered from gaps and non-uniformity over the entire surface, whereas thicker films suffered from a lack of optical modulation. The surface of the thicker films consisted of pellet-like structures which were found by XRD to be

highly orientated (200) β-V_2O_5, which would ease the intercalation/deintercalation of lithium ions during electrochemical reactions.

Cyclic Voltammetry, current density vs scan rate and chronoamperometric measurements were performed on anneal samples. Cyclic voltammetric analysis showed three redox couples corresponding to transitions between $Li_xV_2O_5$ phases. The 60min samples had the best performance as a cathode material with maximum current density values of 1.26 $mAcm^{-2}$ compared to 0.25 $mAcm^{-2}$ and 0.1 $mAcm^{-2}$ for 40 min and 30 min respectively. The 1h sample also had a linear relationship between the current density and square root of the scan rate indicating more efficient charge transfer for the former. Unfortunately, the films suffered from significant current density reduction under electrochemical cycling indicating instability in the electrolyte; thus negating any realistic use as a cathode material. When considering the optical properties of the films it was found that the 60 min samples also had the best ΔT values of 27% and 17% at 650nm and 900 nm respectively.

Overall it was found that grown films showed good electrochemical performance with efficient phase transitions and high current density values albeit with poor stability. Future work will look at improving the film growth to enable continuous coating of thinner films for better electrochemical cycling stability.

References:

1) C. Piccirillo, R. Binions, I.P. Parkin, *Chem. Vap. Deposition*, **2007**, 13, 145–151.
2) R. N. Nenashev, N. E. Mordvinova, V. P. Zlomanov, V. I. Kuznetsov. *Inorg. Mater*., **2015**, *51*, 891–896
3) J. A. Beardslee, A. K. Mebust, A. S. Chaimowitz, C. R. Davis-VanAtta, H. Leonard, T. L. Moersch, M. Y. Afridi, C. J. Taylor. *Chem. Vap, Deposition*, **2010**, 16, 206-210.
4) M. N. Field, I. P. Parkin. *J. Mater. Chem*., **2000**, 10, 1863–1866.
5) C. W. Zou, X. D. Yan, D. A. Patterson, E. A. C. Emanuelsson, J. M. Bian, W. Gao. *CrystEngComm*., **2010**, 12, 691–693.
6) L. M. Kindsch, E. C. Alocija, *Sensors*, **2007**, 7, 1630-1642.
7) Z. Tong, J. Hao, K. Zhang, J. Zhao, B-L. Su, Y. Li. *J. Mater. Chem. C*, **2014**, 2, 3651-3658
8) M. Benmoussa, A. Outzourhit, A. Bennouna, E. Ameziane. *Thin Solid Films*, **2002**, 405, 11–16.
9) A. Vadivel Murugan, M. V. Reddy, G. Campet, K. Vijayamohanan, *J. Electroanal. Chem*., **2007**, 603, 287–296.
10) Y. S. Cohen, D. Aurbach, *Electrochem.commun*., **2004**, 6, 536–542.
11) M. Wohlfahrt-Mehrens, C. Vogler, J. Garche. *J. Power Sources*, **2004**, 127, 58–64.
12) M. B. Sahana, C.Sudakar, C. Thapa, G. Lawes, V. M. Naik, R. J. Baird, G. W. Auner, R. Naik, K. R. Padmanabhan. *Mater. Sci. Eng. B*, **2007**, 143, 42–50.
13) Y. Li, J. Yao, E. Uchaker, M. Zhang, J. Tian, X. Liu, G. Cao, *J. Phys. Chem. C*, **2013**, 117, 23507–23514
14) M. Benmoussa, A. Outzourhit, R. Jourdani, A. Nennouna, E. L. Ameziane. *Activ.Passiv.Elec.Comp*., **2003**, 26, 4, 245-256
15) M. Benmoussa, A. Outzourhit, A. Bennouna, E. L. Ameziane. *Thin Solid Films*, **2002**, 405, 11-16

16) D.McNulty, D. N. Buckley, C. O'Dwyer, *J. Power Source*, **2014**, 267, 831–873.
17) C. Xiong, A. E. Aliev, B. Gnade, K. J. Balkus Jr, *ACS Nano*, **2008**, 2, 2, 293–301.

Chapter 7: Evaluation of silver doped V_2O_5 films grown by CVD

7.1 Introduction

After finding suitable growth conditions for the AACVD method and performing electrochemical measurements on the resultant films it was deemed necessary to improve the electrochemical properties, in particular the stability. In this chapter we report on the addition of silver to the AACVD grown system in an effort to improve the electrochemical stability of the grown films. Silver was chosen as a dopant because it has previously been shown to significantly improve the intercalation rate, specific capacity and cycling performance by inserting into the V_2O_5 framework .[1-6]

7.1.1 Materials and film growth

The growth of silver doped V_2O_5 films was carried out on the AACVD system described in chapter 6. The vanadium precursor used was 98% vanadyl acetylacetonate ($VO(acac)_2$) (Sigma-Aldrich) the silver precursor was silver trifluoroacetate (AgO_2CCF_3) (Sigma-Aldrich) methanol was used as the solvent. A series of 0.1 mol/dm^{-3} solutions were made up with: 1, 2, 5, 10 and 15 weight percent silver content by mixing the two solutions in the required proportions. All films were grown on FTO substrates.

Samples were grown at temperature range of 300-450°C with various doping percentages for the duration of 1h, as with the nominally un-doped samples in chapter 6 all samples were annealed in air post growth at 600°C for three hours.

a

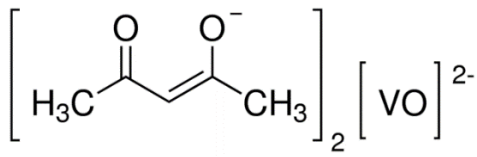

b

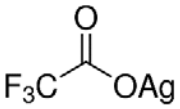

Figure 7: a) Vanadyl (IV) acetylacetonate precursor ($VO(acac)_2$) b) Silver TrifluoroAcetate precursor ($AgO(C_2F_3O)$)

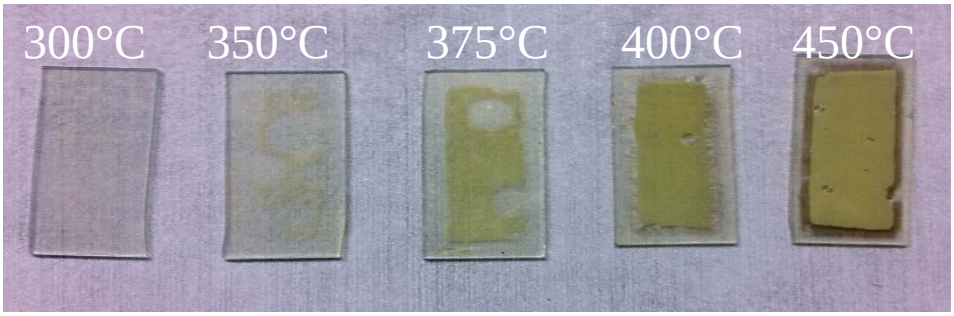

Figure 7.1: Set of samples grown for a temperature range of 300-450°C for the duration of 1h. Films have been annealed for 3h at 600°C. All of the films observed were grown with 15% silver doping. As can be seen from the picture the growth temperature directly impacts the film uniformity, coverage and thickness. Films grown at a lower temperature are patchy and non-uniform which improves at higher growth temperatures of 400 and 450°C

7.1.2 Characterization

Surface material characterization if not mentioned otherwise was carried out using the same apparatus and techniques as mentioned previously in chapter 6.1

7.2 Morphology

Figure 7.2 depicts SEM images of samples grown at 450°C for 1h at varying silver doping percentages of 0, 1, 2, 5, 10 and 15 weight percent. The films exhibit needle/rod-like structures at low silver loading (0, 1 and 2 weight percent silver) transitioning through a less distinct morphology to pellet like structures at 10 weight percent silver and back again at 15 weight percent. In figure 7.2.1 which depicts films grown at 400°C, a similar trend to samples grown at 450°C was observed. Although, unlike the former the transition of surface structures from needle-like to pellet like is less distinct and can consist of a mix of structures. Still, films grown with 15 weight percent silver doping had pellet-like structures dominating the surface. This difference was attributed to the presence of both α and β-V_2O_5 as per XRD shown in figure 7.3.1.

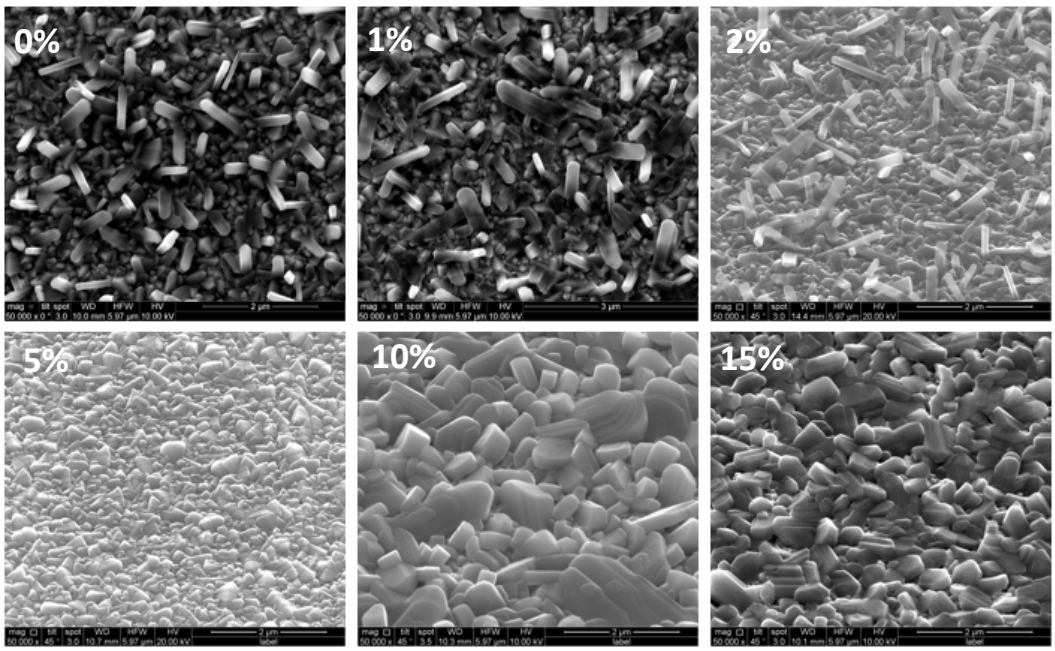

Figure 7.2: SEM images of: Samples with 0, 1, 2, 5, 10 and 15 weight percent silver doping which were grown at 450°C for 60 min and annealed for 3h at 600°C. From the images an observation could be made that upon increasing the amounts of silver doping a gradual change of needle-like to platelet-like surface structures could be observed. The on-set of change can even be seen for the 2 weight percent sample.

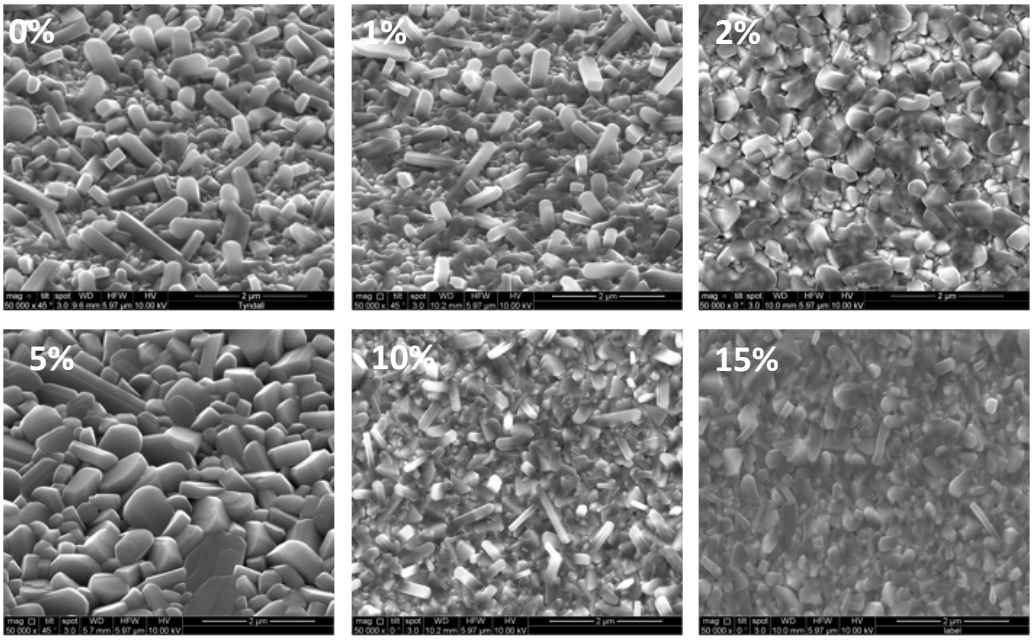

Figure 7.2.1: SEM images of: Samples with 0, 1, 2, 5, 10 and 15 weight percent silver doping which were grown at 400°C for 60 min and annealed for 3h at 600°C. From the images it can be seen that increasing amounts of silver doping change the surface structures from needle-like for 0, 1 and 2 weight percent to platelet-like structures for 5, 10 and 15. A mixture of needle-like and platelet-like structures could be observed for the 10 weight percent samples.

When comparing films with a constant 15 weight percent silver doping and varying deposition temperatures from 300-450°C it can be seen that there are differences in the morphology of the samples as seen in figure 7.2.2 and coverage as seen in figure 7.1 Samples grown at temperatures up to 400°C have very thin films which also had poor uniformity and coverage which would explain the morphology observed in figure 7.2.2. Higher growth temperatures of 400 and 450°C produced films which were thicker, more uniform and had their surface covered with large platelet-like crystallites. Based on the results observed in figures 7.1-7.2.2 an observation was made. It was concluded that growth temperatures have a direct effect on film deposition and coverage but it was the percentage of silver doping which had a stronger effect on the morphology of the surface.

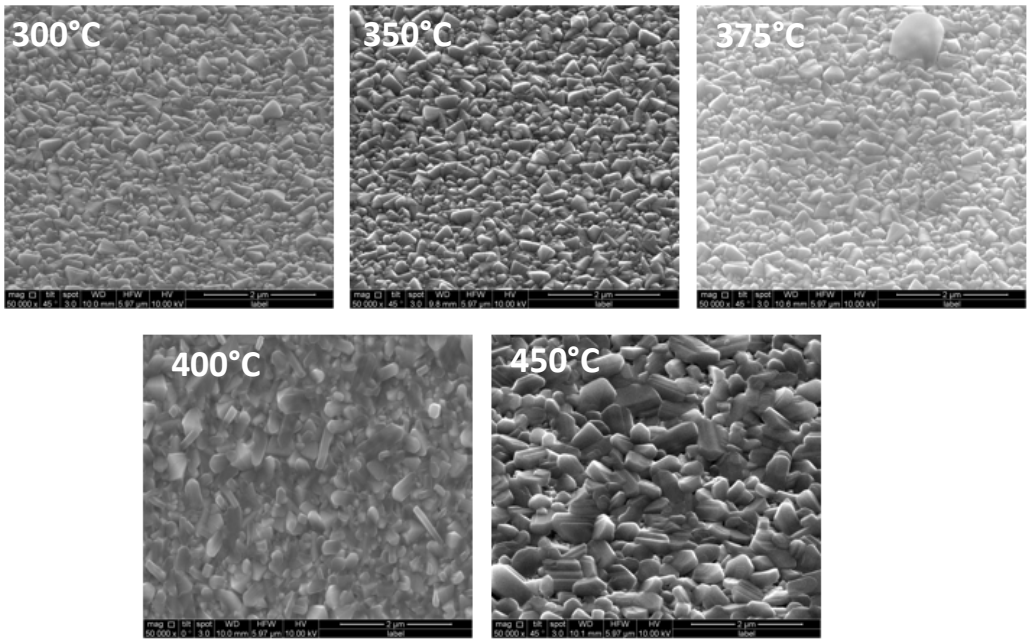

Figure 7.2.2: SEM images of 15% Ag doped samples grown at 300, 350, 375, 400 and 450°C for 60 min and annealed for 3h at 600°C. Lower growth temperatures have less distinct morphologies when compared to higher growth temperatures where the surface was covered by distinct pellet-like structures.

From the deposition time and the coating thickness, deposition rates were obtained. It was found that the deposition rate increased with increasing growth temperature with the exception of the 400°C sample, with values of 6.7, 5.8, 9.0 nm min^{-1} for 375, 400 and 450°C respectively as seen in table 7 and figure 7.2.3. It was proposed that such a decrease in the growth rate could be due to the precursor pre-reacting in the gas phase[7]. A certain degree of error could be present in the measurement hence the addition of error bars in figure 7.2.3 with standard deviation of data with a scaling factor of 1 was implemented.

As can be seen from the overview of the morphological properties of the films, it can be concluded that the amount of silver doping had a large impact on the morphology whereas the growth temperature at higher silver percentages had an impact on the growth rate, film uniformity and coverage but had no major impact on the surface morphology.

Growth Temperature (°C)	375	400	450	450	450
Percentage of Ag doping	0%	0%	5%	10%	15%
Thickness (nm)	402	348	540	480	450
Growth Rate ($nmmin^{-1}$)	6.7	5.8	9.0	8	7.5
Error ($nmmin^{-1}$)	0.3	0.5	0.2	0.2	1

Table 7: Comparison of growth temperature, thickness and deposition rates for un-doped films grown at temperatures of 375-400°C and silver doped films grown at 450°C with of 5 to 15%.

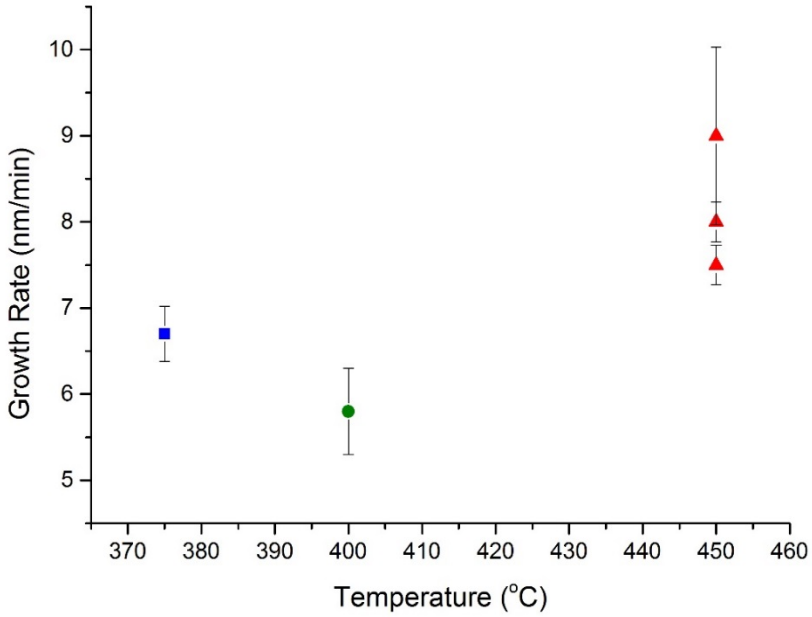

Figure 7.2.3: Graph of growth rate (nm min^{-1}) vs deposition temperature (°C) for films grown at 375, 400 and 450 °C and annealed for 3h at 600°C. Films grown at 375°C (Blue square) and 400°C (Green circle) were un-doped whereas 450°C (red triangle) had 5, 10 and 15 weight percent silver doping. The graph illustrated the reduction in growth rate for 400°C films due to pre-reaction in the gas phase and shows the decrease of growth rate for the 450°C with increasing silver doping percentage.

7.3 Crystallography

X-ray diffraction analysis had been carried out on all of the annealed silver-doped V_2O_5 samples.

X-ray diffraction patterns of silver-doped samples grown at 450°C for 1h and annealed for 3h at 600°C are presented in figure 7.3. These samples had varying percentages of silver doping from 0 to 15 weight percent. A common trend was seen throughout the dopant levels, two peaks at 12.3° and 20.2° with Miller indices (200) and (010) were continuously observed and were attributed to monoclinic β-V_2O_5 and orthorhombic α-V_2O_5 respectively[8,9]. Other V_2O_5 peaks could be observed in films with higher weight percentage silver doping as seen in the case of the 10 and 15 weight percentage films

which contained peaks around 41.3º and 26.1º with Miller indices (020) and (201). When comparing this to samples grown at 400°C as mentioned in figure 7.3.1. a similar trend was observed.

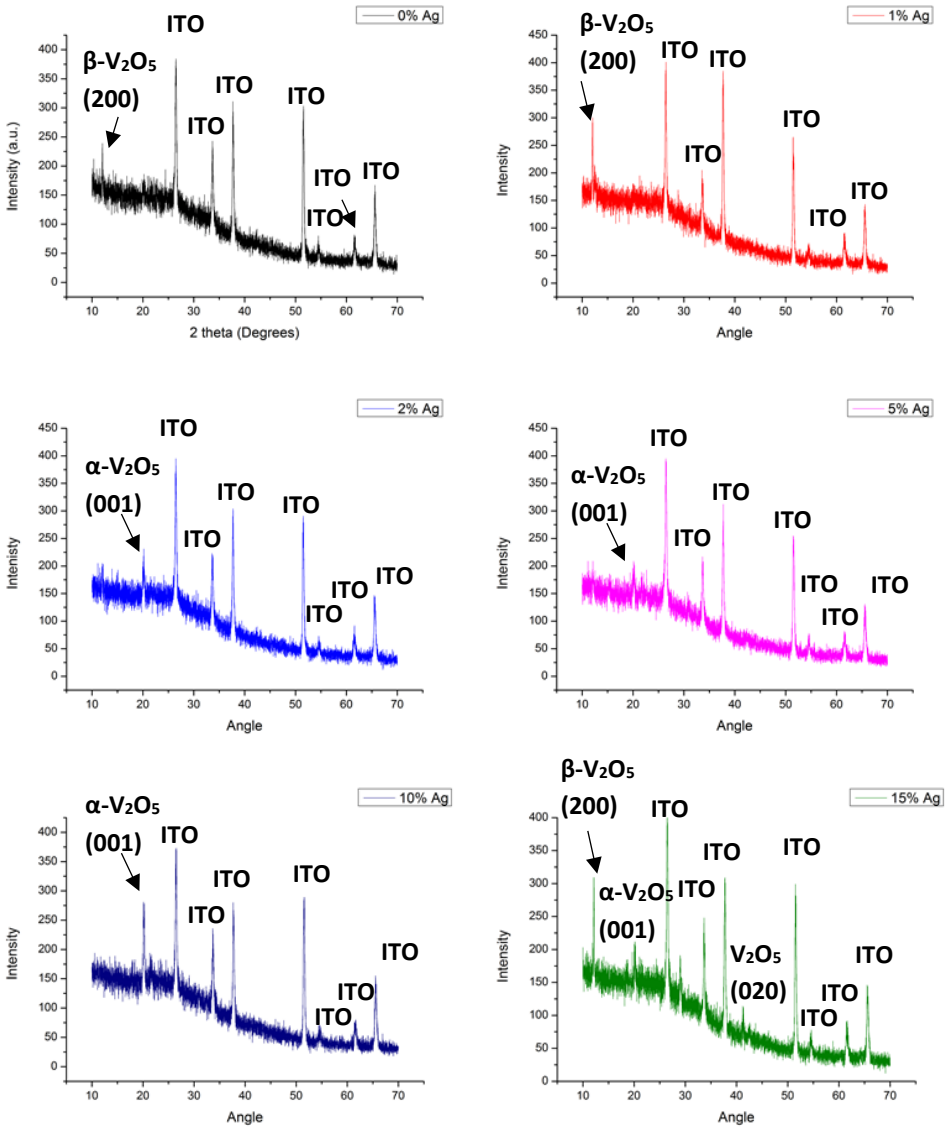

Figure 7.3: XRD of silver doped samples grown at 450°C for 1h: (black)-0% Ag, (red)-1% Ag, (blue)-2% Ag, (purple) - 5% Ag, (navy) - 10% Ag, (green) - 15% Ag, all samples were annealed at 600°C for 3h. The 15% Ag samples have both α and β V_2O_5

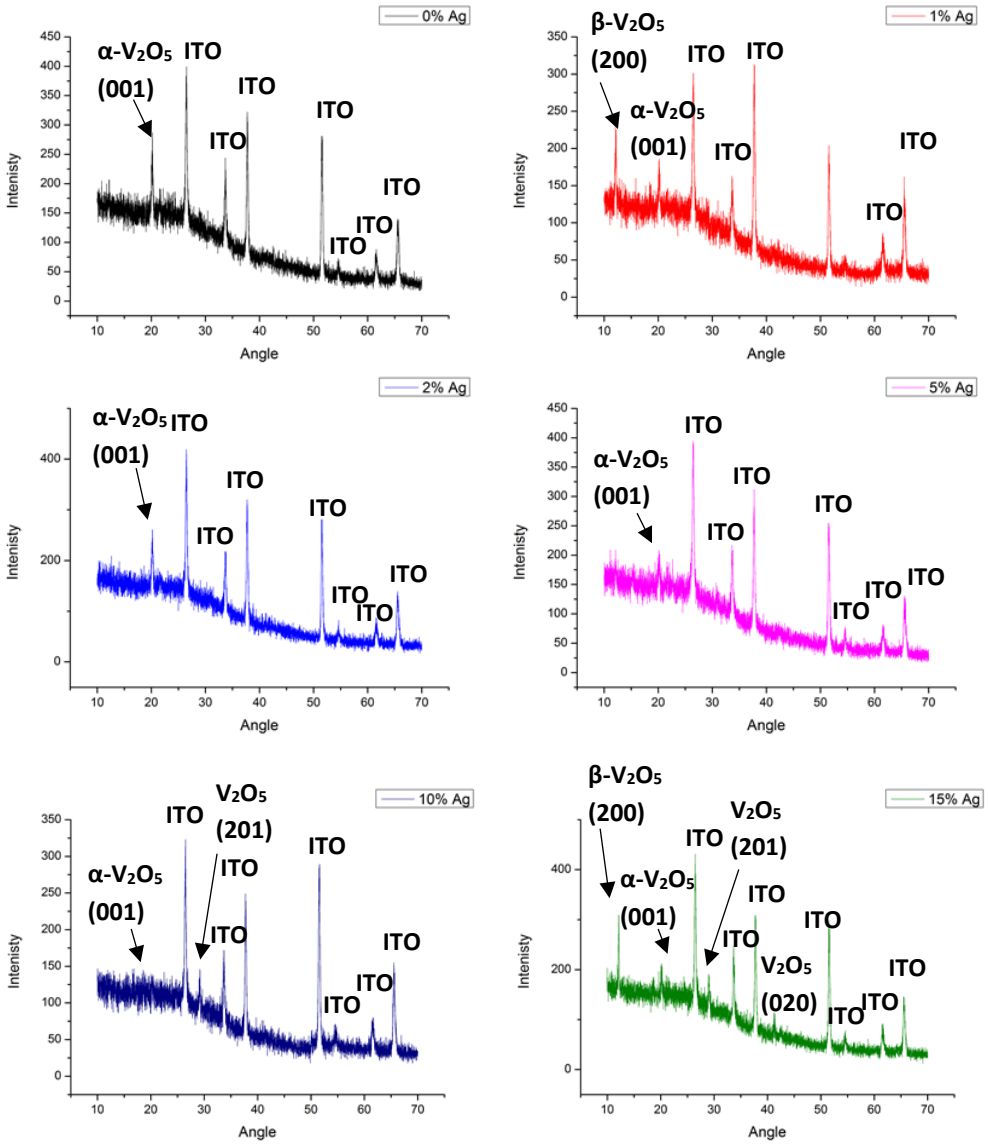

Figure 7.3.1: XRD of silver doped samples grown at 400°C for 1h: (Black)-0% Ag, (Red)-1% Ag, (Light blue)-2% Ag, (purple) - 5% Ag, (Dark blue) - 10% Ag, (Green) - 15% Ag. All samples were annealed at 600°C for 3h

Figure 7.3.2 compares 15 weight percentage silver-doped samples which were grown at temperatures ranging from 300-450°C. A strong preferred orientation along the (200) plane is observed and increased as growth temperature is increased. At lower growth temperatures of 300°C and 350°C we see an absence of all vanadium peaks for the former and the presence of only one (200) peak for the latter. The absence of any vanadium peaks in the 300°C samples could be explained by the fact that the crystallites

were very small and the XRD could not pick up any vanadium peaks. Substrate peaks were constant throughout all of the XRD's and are located at 26.5, 33.7, 37.8, 51.6, 54.6, 61.6 and 65.5 ^{o} with Miller indices (110), (101), (200), (211), (220), (310) and (301). When a comparison was made it was seen that at higher growth temperatures and higher silver concentrations there seemed to be a preference for the (200) β-V_2O_5. The presence of such high degree of crystallinity could be beneficial for electrochemical properties as will be emphasized in the electrochemical properties discussion.

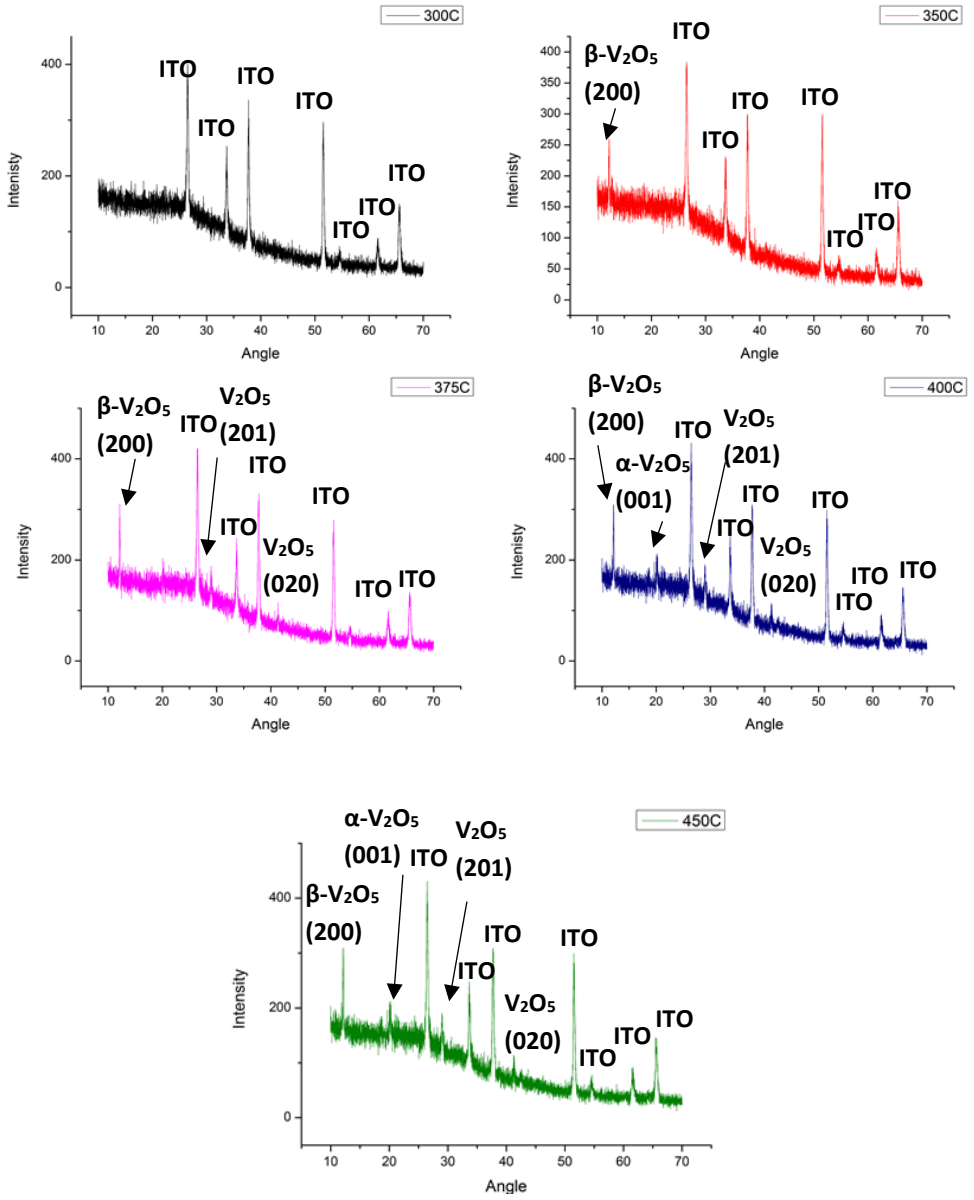

Figure 7.3.2: XRD of 15% silver doped samples grown for 1h at: (black)-300°C, (red)-350 °C, (purple)-375 °C, (navy) - 400 °C, (green)-450 °C, all annealed at 600°C for 3h.

7.4 Electrochemical properties of Ag doped V_2O_5 films

After discussing the morphological and structural properties of the silver-doped films grown at different temperatures and with different silver doping concentrations it is important to understand how these properties influence the electrochemical properties. For these reasons the properties of the films were tested by cyclic voltammetry (CV), current density vs time (I-t), potential vs time (V-t), potential vs discharge capacity (V-c) and electrochemical impedance measurements were carried out.

The majority of electrochemical testing was also carried out as previously mentioned in chapter 6 but several new methods of testing were introduced such as Chronopotentiometric testing and Electrochemical impedance spectroscopy which were also carried out by the collaborating group from the technological institute of Crete. Chronopotentiometric (CP) tests were conducted in the voltage range from +0.3 V to -0.5V with a constant specific current of 400 mAg^{-1}. Electrochemical impedance spectroscopy (EIS) was obtained at 0.4 V with an AC amplitude of 0.1 V over a frequency range of 10mHz-35 kHz. Nyquust plots were fitted and analysed using Z-view software. All electrochemical tests were carried out at room temperature (25°C)

Cyclic voltammograms as seen in figure 7.4 (a) and 7.4 (b), were obtained for samples grown at 400 and 450°C with 0, 5 and 15% Ag doping. As seen previously in chapter 6 samples exhibit two/three redox couples which are associated with phase transitions between the: α, ε, δ phases[10,11,12] which are caused by the insertion of Li ions into the V_2O_5 lattice. A broad peak at around -0.5V was assigned to lithium ion de-intercalation from the surface which occurs at a faster rate, compared to de-intercalation reactions taking place within the bulk material.[11]

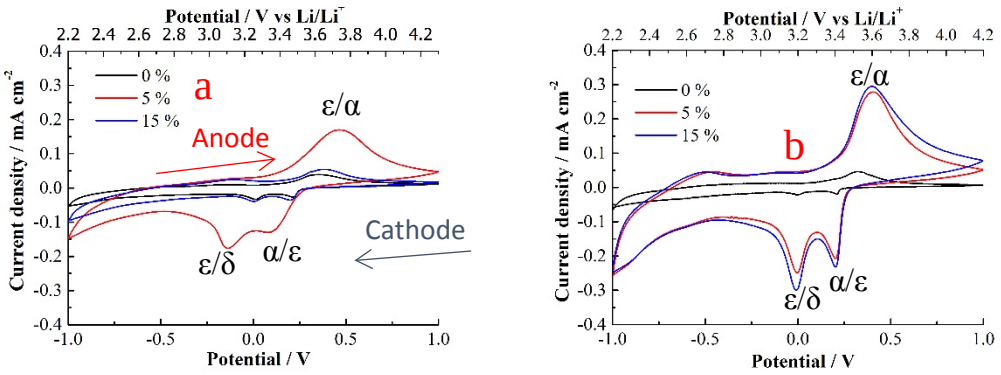

Figure 7.4 (a) and 7.4 (b)**:** 7.4 (a) Cyclic Voltammogram (i-v) curves of 1st cycle for 0, 5 and 15 weight percent Ag doped samples grown at 400°C for 60 min. 7.4 (b) Cyclic Voltammogram (i-v) curves of 1st cycle for 0, 5 and 15 weight percent Ag doped samples grown at 450°C 60 min. All annealed for 3h at 600°C.

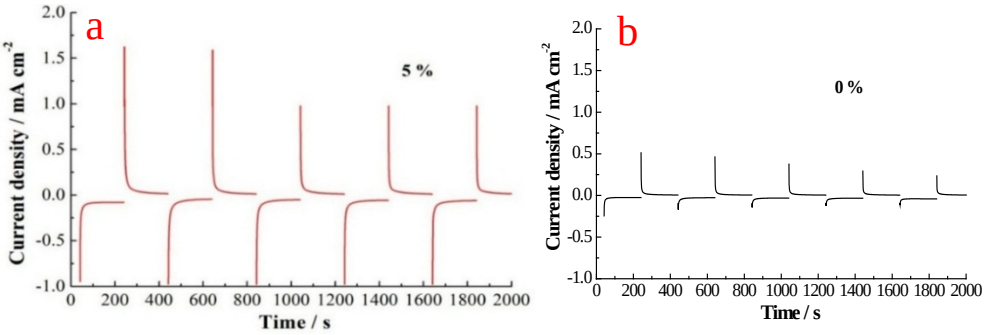

Figure 7.4.1**:** Current density vs. Time (i-t) curves of a) 0% and b) 5 weight percent Ag doped samples at 400°C 60min and annealed for 3h at 600°C. A difference between intercalation and de-intercalation charge is observed in the different step-like behaviour which is an indication of lithium ion retention and poor reversibility.

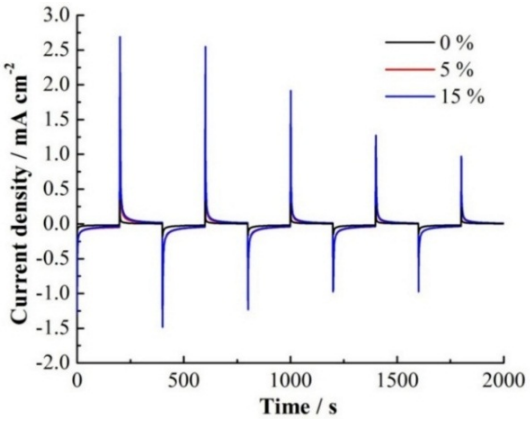

Figure 7.4.2**:** Current density vs. Time (i-t) curves of 0, 5 and 15% Ag doped grown at 450°C 60 min. Annealed for 3h at 600°C. A smaller difference between intercalation and deintercalation charge is observed indicating retention of lithium ions and decreased reversibility.

In figure 7.4 (a) the 400°C samples with varying degrees of silver doping exhibited only a single anodic peak at around 0.5 V and two cathodic peaks at 0.24V, 0.01V corresponding to phase transitions between the α/ε, ε/δ and ε/α phases respectively. The presence of only a single anodic peak for the 5% sample could be due to the rapid changing of phases or the presence of only a (200) β-V_2O_5 as seen in figure 7.3.1 in chapter 7.3 and as was observed by Murugan et al.[11] The 450°C samples observed in figure 7.4 (b) showed similar results but possessed larger current density values. When comparing the current densities, it can be clearly seen that the values increase with both the increasing growth temperature and, in the case of the 450°C sample, increasing % silver load. This was not the case for the 400°C samples which showed the best results for 5% Ag loading. Such a result could be attributed to larger and more distinct platelets on the surface out of all the 400°C films.

To measure the amount of lithium interchanged between the silver doped samples and the electrolyte, chronoamperometric measurements were carried out.

In figures 7.4.1 and 7.4.2 we can see a chronoamperometric (I-t) curves of the 400°C and 450°C samples with 0, 5 and 15 weight percent Ag doping. For the 0% sample grown at 400°C step like behaviour was observed, as seen previously in chapter 6, but

with very small current densities when compared to the doped analogues which can be seen in figures 7.4.1 (b) and 7.4.2. It was observed that for the un-doped samples the intercalated charge is lower than the deintercalated which serves as an indication of lithium ions remaining in the material and poor reversibility of the process. A similar trend to the un-doped is observed for the 5% silver-doped sample grown at 400°C as seen in figure 7.4.1 (b), but with a difference in initial current density values which significantly larger (1.7 mA/cm^2 compared to 0.5 mA/cm^2 respectively). The chronoamperometric curve for the 400°C samples only portrays the results for the 5% Ag doping due to the instability of the other 400°C samples in the electrolyte. and most significant results as compared to the other doping percentages. Figure 7.4.2 on the other hand looks at the 450°C samples. All tested samples were stable in the electrolyte hence all three doping weight percentages could be compared. Even though overlapping was present it was evident that a large difference in the current density could be observed. The 15 weight percent samples show a maximum current density of 2.7 $mAcm^{-2}$ in the first 500 seconds which then starts decreasing until it reaches a value of 0.9 $mAcm^{-2}$. These values are quite substantial when compared to the un-doped and 5 weight percent doped samples which display values which are significantly smaller. A step-like behaviour is also observed as seen in figure 7.4.1. (a) which again is an indication of an irreversible process.

Chronopotentiometric curves for both 450°C and 400°C can be observed in figure 7.4.3. The analysis was carried out under a constant specific current of 400 $mAhg^{-1}$ and a potential ranging from +0.3V to -0.5V versus a silver/silver chloride electrode. When looking at the 400°C samples with 0, 5 and 15 percentage silver doping it can be observed that they lack the staircase-like shape that is observed for the 450°C samples. This can be explained by less defined phase transitions associated with lithium ions and by the needle like structures which cover the surface as seen in figure 7.1.1. When this is compared to the samples grown at 450°C it can be seen that the staircase-like behaviour is observed for the 15% doped sample with two plateaus at +0.195V and -0.029V indicating the two phase transitions as observed in the CV in figure 7.4. This staircase-like behaviour is also in agreement with what is observed in figure 7.4.2. When comparing the maximum discharge capacity values for 450°C and 400°C samples the

maximum values observed were 275 $mAhg^{-1}$ for 15% silver doped samples and 10.5 $mAhg^{-1}$ for the 5% silver doped samples respectively. From this it can be concluded that films grown at 450°C with the highest silver doping undergo efficient lithium ion phase transitions with large discharge capacity values which make them efficient for battery applications.

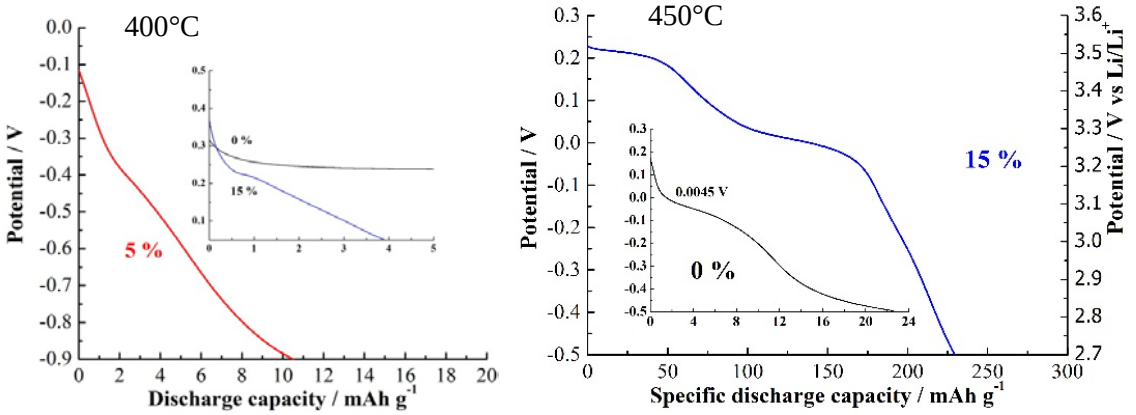

Figure 7.4.3**:** Potential vs. Discharge capacity (v-c) curves of 0, 5 and 15% Ag doped samples grown at 400°C and 450°C. Discharge capacity values were the highest for 450°C with values of 275mAh g^{-1}.

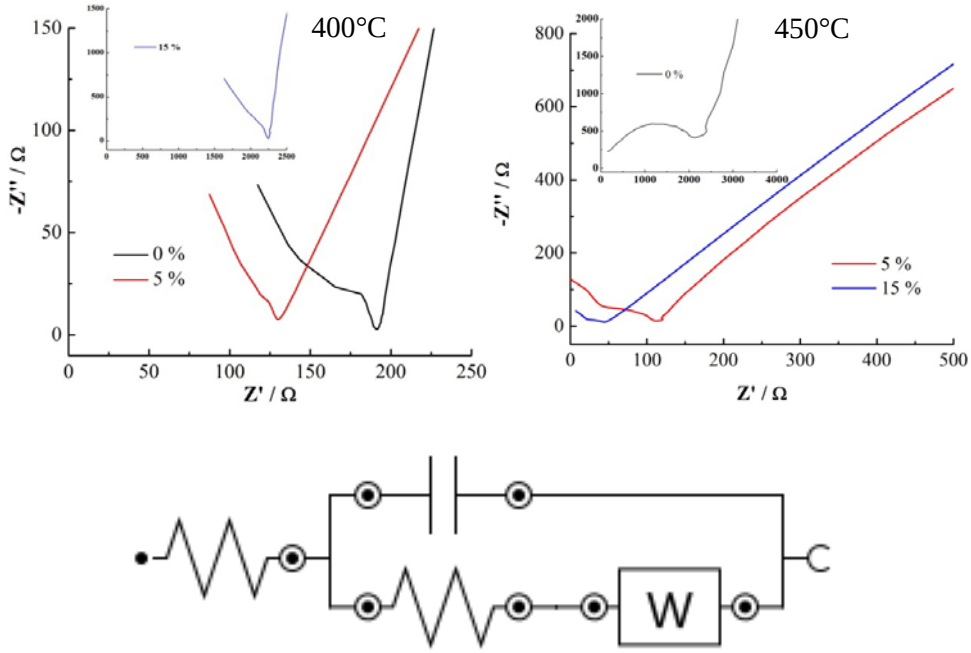

Figure 7.4.4 (a) Electrochemical Impedance measurements of 0,5 and 15% Ag doped samples grown at 400°C and 450°C. A smaller semi-circle is observed for the 15% 450°C films indicating a lower charge transfer resistance at the electrode/electrolyte interface which allows for efficient lithium ion intercalation 7.4.4 (b) Electric circuit used for fitting Nyquist plots in figure 7.4.4 (a) which consist of a constant phase element (CPE), Warburg impedance (W), Ohmic resistance of electrolyte and cell components (Re) and charge transfer resistance in the interface between cathode and electrolyte (Rct)

Lastly electrochemical impedance spectroscopy (EIS) was used to analyse the samples. It is a non-destructive technique which is used to study the electrode kinetics of cathode and anode materials[11]. The impedance spectra are presented in the form of Nyquist plots (Z' vs -Z'') are displayed in figure 7.4.4, where Z' is the real part of impedance and Z'' is the imaginary part. Impedance is the "complex resistance" and the impedance spectra provide information on several things, at high frequencies it shows surface film resistance, at middle frequencies it shows charge transfer resistance (R_{ct}) which arises at the cathode-electrolyte interface and the semicircle at low frequencies represents the bulk resistance which arises from the electronic resistivity of the active material and

ionic conductivity in the pores of the electrode filled with electrolyte.[13] The spectra is analysed by applying it to a similar electrical circuit as seen in figure 7.4.4(b) where Re is ohmic resistance of electrolyte and cell components, W is Warburg element is associated with the diffusion of lithium ions at all voltages, CPE is the constant phase element and accounts for the non-homogeneous nature of the composite electrode and the charge transfer resistance at the interface between electrode and electrolyte.[14,15] When considering the results for the 450°C and 400°C samples in figure 7.4.4(a) it should be noted that the diameter of the semicircle is directly related charge transfer resistance hence the smaller it is the smaller the resistance. It was found that the charge transfer resistance values for the 450°C samples were 30Ω, 70 Ω and 1700 Ω for 15%, 5% and 0% respectively. From this we can see that the lowest resistance was for the 15% silver doped sample which indicates more efficient transfer of lithium ions through the interface hence giving it better performance which is in good agreement with the trends that have been observed in this chapter. The 400°C had very high resistance values for the 0%, 5% and 15% which is indicative of very poor lithium intercalation capabilities.

7.5 Summary

Silver doped V_2O_5 films were grown for several purposes. To investigate if the silver doping would have an effect on film growth and electrical properties of the films. Film growth was carried out at temperatures ranging from 300°C to 450°C for the duration of 1h, with further annealing being carried out after the growth for the duration of 3h and 600°C as with the un-doped films in chapter 6.

When considering the morphology, it should be noted that both growth temperature and percentage of silver doping had an effect on film growth. For 400°C the increasing percentage of silver doping influenced the shape of the structures covering the surface turning them from needle-like to more pellet shaped at 15 weight percent of silver doping. A degree of variability was still present with a mixture of both being present below maximum doping. Upon increasing the growth temperature to 450°C a similar trend was observed but with a more defined change from needle-like to platelet structure

happening at 5 weight percent silver doping. When a comparison was made between films with the highest percentage of silver doping but with variable growth temperatures ranging from 300-450°C, an observation was made that all films had platelet structures covering the surface irrespective of the growth temperature. Such behaviour allows to conclude that the percentage of silver doping had a larger effect on the morphology of the surface than growth temperature.

X-ray diffraction studies found that 15% silver doped samples were primarily β-V_2O_5 (200) orientated irrespective of the growth temperature. At lower silver doping percentages, a mixture of α and β-V_2O_5 could be observed.

Electrochemical studies were carried out to understand the effectiveness grown films as battery materials. CV studies have found characteristic α/ε, ε/δ, δ/ε ε/α phase transitions corresponding to lithium ion intercalation as observed in chapter 6. It was also observed a combination of maximum silver doping of 15 weight percent and the highest growth temperature of 450°C offered best overall results. These films were most stable, with current density values of 0.3 $mAcm^{-2}$, moderate intercalation-deintercalation times of 16 and 23s respectively and discharge capacity values of 275 $mAhg^{-1}$. Characteristic staircase-like phase transitions were observed indicating good lithium ion intercalation combined with a low charge transfer resistance of 30Ω.

On the basis of the results it could be concluded that the implementation of silver doping does indeed influence film growth and electrochemical properties providing a material which could be successfully used as a cathode material.

References:

1) M. V. Reddy, G. V. Subba Rao, B. V. R. Chowdari, *Chem. Rev*., **2013**, 113, 5364–5457.
2) C. Xiong, A. E. Aliev, B. Gnade, K. J. Balkus Jr, *ACS Nano*, **2008**, 2, 2, 293–301.
3) F. Coustier, J. Hill, B. B. Owens, S. Passerini, W. H. Smyrl, *J. Electrochem. Soc*., **1999**, 146, 1355–1360.
4) A. Sakunthala, M. V. Reddy, S. Selvasekarapandian, B. V. R. Chowdari, P. C. Selvin, *Energy Environ. Sci*., **2011**, 4, 1712.
5) K. J. Takeuchi, A. C. Marschilok, S. M. Davis, R. A. Leising, E. S. Takeuchi, W. Dri, *Coord. Chem. Rev*., **2001**, 283, 219-221
6) Y-Q. Chu, Q-Z. Qin, *Chem.Mater*., **2002**, 14, 3152–3157.
7) E. Elangovan, K. Ramamurthi, *Thin Solid Films*, **2005**, 476, 231-236
8) D. Barreca, G. A. Battiston, F. Caccavalec, V. di Noto, R. Gerbasi. A. Gregori, G. A. Rizzi, A. Tiziani, E. Tondello, *J. Phys. IV France*, **1999**, 9, Pr8-529
9) A. A. Akl, *Appl. Surf. Sci*., **2007**, *253*, 7094–7099.
10) A. Pan, J.-G. Zhang, Z. Nie, G. Cao, B. W. Arey, G. Li, S. Liang, J. Liu, *J. Mater. Chem*., **2010**, 20, 9193.
11) A.Vadivel Murugan, M. V. Reddy, G. Campet, K. Vijayamohanan, *J. Electroanal. Chem*., **2007**, 603, 287–296.
12) D.Zhu, H. Liu, L. Lv, Y. Yao, W.Yang, *Scr. Mater*., **2008**, 59, 642–645.
13) M. V. Reddy, B. Pecquenard, P. Vinatier, A. Levasseur, *J. Power Sources*, **2007**, 163, 1040–1046.
14) N. Sharma, J. Plévert, G. V. Subba Rao, B. V. R. Chowdari, T. J. White. *Chem. Mater*., **2005**, 17, 4700–4710.
15) M. V. Reddy, S. Madhavi, G. V. Subba Rao, B. V. R. Chowdari, *J. Power Sources*, **2006**, 162, 1312–1321.

Chapter 8: Evaluation of V_2O_5 films grown by Pulsed Chemical Vapour Deposition

8.1 Chapter Overview:

As was mentioned in the summary of chapters 6 and 7 the need for atomic layer deposition was governed by the fact that the thickness of the films needed for uniform coverage was too high, which made the material not suitable for electrochromic use. Pulse chemical vapour deposition (CVD), or more correctly atomic layer deposition (ALD) outside of the ALD thermal window[1-3], was used for this purpose.

8.1.1 Material Growth:

The deposition of V_2O_5 films by pulsed chemical vapour deposition was carried out using a Cambridge Nanotech Ultratech Fiji F200LLC. Vanadium(IV) Tetrakis (DimethylAmide) $V^{(IV)}(NMe_2)_4$ (Strem US), as seen in figure 8, was used as the vanadium precursor. Oxygen-argon plasma, or for the thermal processs oxygen or water were used as the co-reagent. Oxygen was supplied by the in-house gas system and deionised water (18MΩ) from a bubbler. Indium doped tin oxide (ITO) glass slides with a surface resistivity of 30-60Ωsq^{-1} (Sigma-Aldrich) were used as substrates for the deposition. The substrates had 5x2cm dimensions and were used as received without any further treatment. Growth was carried out using both plasma and thermal pulsed chemical vapour deposition at the following temperatures: 150, 200, 250 and 300°C for 400 cycles. All of the films underwent a post annealing treatment for 1h at 400°C to help crystallize the surface.

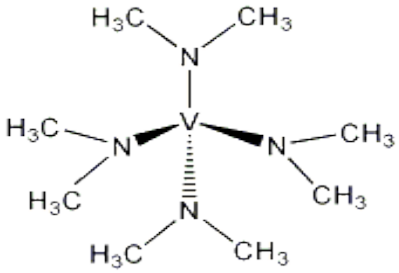

Figure 8: Tetrakis(dimethylamino) vanadium (TDMAV) precursor used for the growth of V_2O_5 films using pulsed chemical vapour deposition

8.1.2 Characterization

Surface material characterization if not mentioned otherwise was carried out using the same apparatus and techniques as mentioned previously in chapter 6.1

2.8.2 Morphology

Photographic images displaying films grown using both plasma and thermal pulsed chemical vapour deposition with no further annealing can be seen in figure 8.1 (a) and (b) respectively. The as-grown plasma films are yellow due to them being polycrystalline and the thermal water and thermal oxygen ALD films are dark due to residual carbon being present on the surfaceas seen in figure 8.1(a).

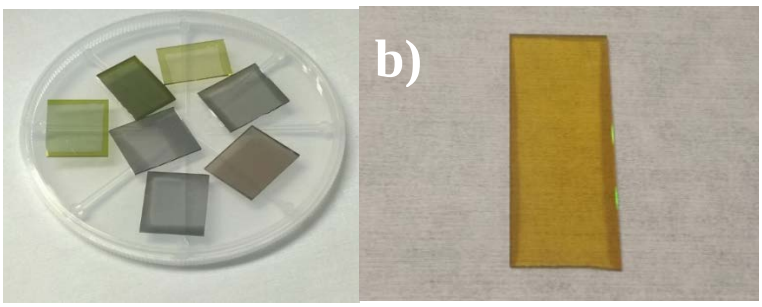

Figure 8.1: (a) As-grown pulsed CVD films grown on the Ultratech Cambridge Nanotech Fiji system using both plasma and thermal pulsed chemical vapour deposition. (b) Annealed 250 °C plasma sample showing a film with a deeper yellow colour. Note the dark edges on all films are an optical effect due to ALD growth on the underside of the substrate.

Representative plain-view SEM images are presented in figures 8.1.1-8.1.3. In all cases, conformal, crack-free films were obtained. Some differences in topography were observed depending on the co-reagent used. Films grown with oxygen-plasma had a rough surface containing particulate like features, as shown in figure 8.1.1 (a)-(b). All films grown with thermal methods (oxygen and water processes) exhibited flat plate like structures in the substrate plane, as shown in figure 8.1.2 (a)-(b) and 8.1.3 (a)-(b). The uniformity size and shape of the crystallites differed significantly from those seen in chapters 6 and 7, where we saw non-uniform, well defined pellet like features with a large thickness for un-doped CVD and a mix of rod and pellet like features for silver doped CVD. Average thickness values differed as well, with an average value for pulsed CVD samples being three to four times less than those seen for CVD as seen in table 8 in this chapter and in chapters 6.2 and 7.2.

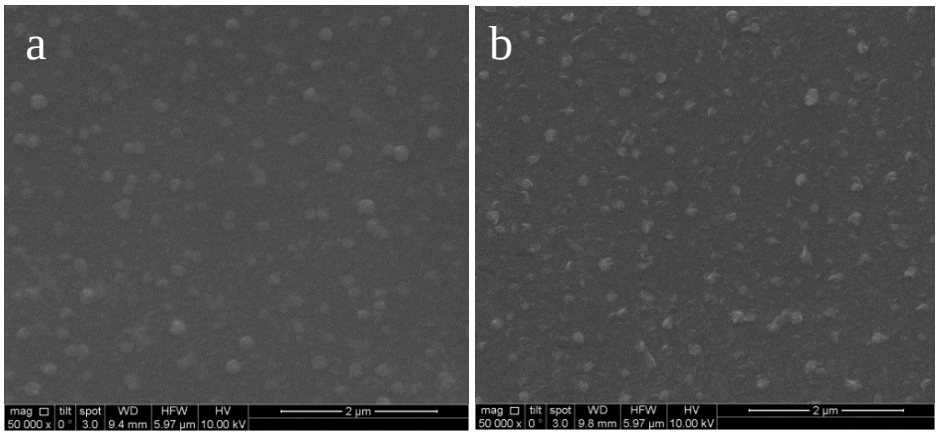

Figure 8.1.1. Representative SEM's of Plasma ALD films grown at 250 °C for 400 cycles with a) no further annealing b) with further annealing at 400^{o}C for 1h. As-grown plasma films were polycrystalline as can be seen in figure 8.1.1 (a). Upon annealing the films for 1h an increase in the crystallinity can be observed as seen in 8.1.1 (b).

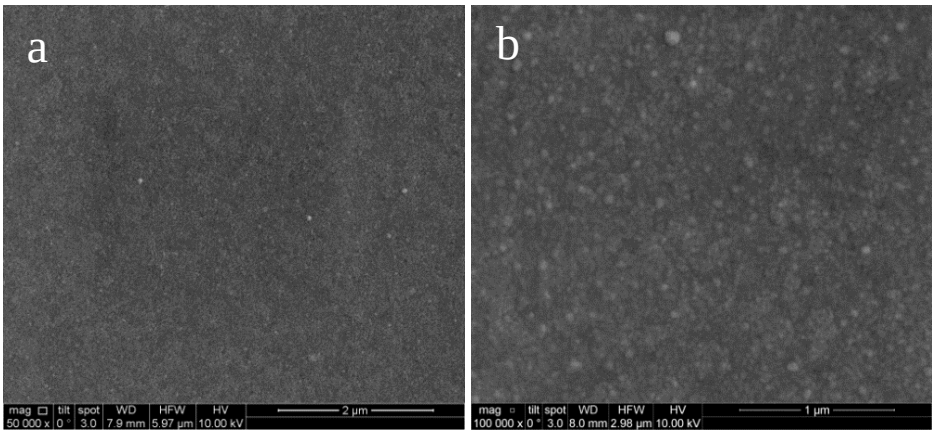

Figure 8.1.2. Representative SEM's of thermal water (a) and thermal oxygen (b) as-grown ALD films grown for 400 cycles at 250 °C. As-grown films were amorphous and did not possess any noticeable crystal structures on the surface of the films.

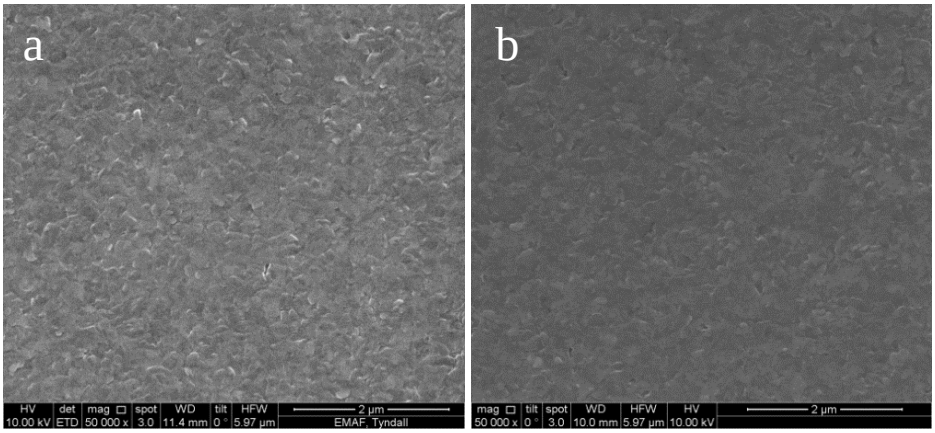

Figure 8.1.3. Representative SEM's of thermal water (a) and thermal oxygen (b) annealed ALD films. Films were grown for 400 cycles at 250 °C and annealed for 1h at 400 °C. Looking at the images it can be seen that annealing induces the formation of platelet like structures.

The 'growth per cycle' (GPC) was calculated for both the plasma and thermal grown films as seen in figure 8.2. This was done by measuring resultant film thickness from SEM cross sections and dividing it by the number of growth cycles, which in the case of these depositions was 400. For all oxygen sources the GPC increased with increasing growth temperature due to an increasing CVD component. For the plasma films the GPC increased with increasing temperature. The values for the growth were 2.4, 2.7, 4.3 and 6.7 Å/cycle at 150, 200, 250 and 300°C respectively. For thermally grown films an

increase in growth rate with temperature was observed for both water and oxygen, with values ranging from 1.8 and 3.7 Å/cycle for the water films and 3.0 and 4.1 Å/cycle for the oxygen films. The measured thickness data are presented in table 8.

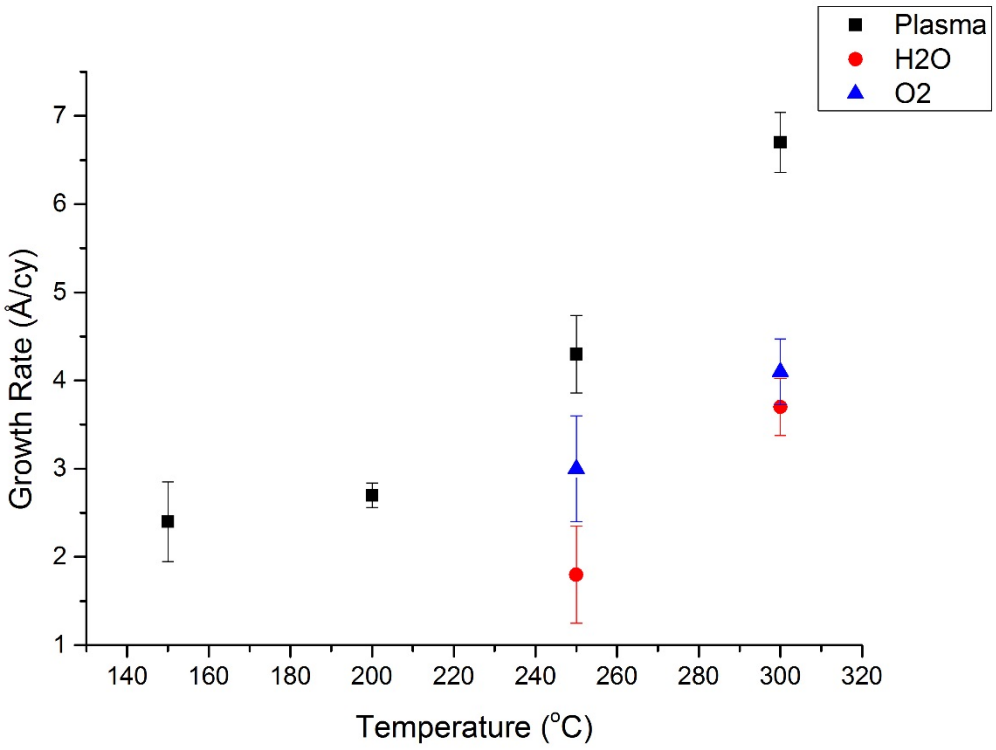

Figure 8.2 Temperature vs growth rate of Plasma, O_2 and H_2O based ALD of V_2O_5. Thin films were grown for 400 cycles at temperatures ranging from 150-300 °C. As expected an increase in the growth rate with increasing growth temperature is observed for both plasma and thermal ALD films above the gas phase decomposition temperature of TDMAV due to an increasing influence of CVD pathways.

Plasma Annealed				
Temperature (°C)	150	200	250	300
Thickness (nm)	97	109	173	268
Error (Å/cycle)	0.45	0.14	0.44	0.34
Thermal Annealed	**Thermal Water**	**Thermal Water**	**Thermal Oxygen**	**Thermal Oxygen**
Temperature (°C)	250	300	250	300
Thickness (nm)	72	146	120	165
Error (Å/cycle)	0.55	0.325	0.6	0.375

Table 8. Thickness values for plasma and thermal oxygen/water ALD samples grown at 150-300 °C for 400 cycles.

8.3 Crystallography

Figure 8.3 (a) displays the X-ray diffraction pattern for the as-grown plasma films. Films were grown with oxygen/argon plasma at temperatures ranging from 150-300°C with no anneal being undertaken. The 2Θ peaks at 12.78° and 20.43° correspond to the monoclinic β[4] and orthorhombic α-phases of V_2O_5[5] respectively. Similar results can be observed in chapters 6.3 and 7.3. The peaks 21.33° and 43.5° were assigned to V_4O_9 (010) and V_4O_9 (400) respectively, with that at 30.11° corresponding to the ITO substrate. The most intense diffraction peak in films grown at 250°C was assigned to V_4O_9 (010), whereas films grown at 150°C have only the substrate peak present. Post annealing in air for 1hour at 400°C resulted in a shift in orientation and an increase in peak intensity as seen in figure 8.3 (b). The intense feature at 20.15° was assigned to V_2O_5 (001) which has greater chemical stability than V_4O_9 observed in the un-annealed samples. Similar results can be found in the literature[6,7,8,9]. Similarly, the feature at 43.5° assigned to V_4O_9 (010) was observed to decrease in intensity along with evolving to V_2O_5 (002). This was also reported by Akl et al.[5]. Minor low intensity features were attributed to sub-oxide V_3O_7 orientations (-111) and (406) at 24.5° and 35.5°

respectively. The increased peak intensities can be explained by the increased grain size and film thickness at higher temperatures

The X-ray diffraction patterns for the as grown thermal films with oxygen or water as co-reagents, at temperatures of 250°C and 300°C, are presented in figure 8.3.1 (a). It can be clearly seen that the majority of the films were amorphous with peaks only seen at 30.11° corresponding to the ITO substrate. Only the 300°C thermal-oxygen film has an additional small intensity peak at 35.22° corresponding to VO_2 (311). Following the annealing step, a peak at 20.43°, assigned to orthorhombic α-V_2O_5 (001) was observed as well as low intensity V_2O_5 (002) peaks at 43.5°, presented in figure 8.3.1 (b). Samples grown at 300°C with the water thermal process had the highest intensity V_2O_5 (001) and V_2O_5 (002) peaks. The previously assigned low intensity (-111) V_3O_7 feature was also observed at 24.5° in the thermally grown films. This is similar to results published by Musschoot[10] and Rubloff[11], in which films grown with plasma or ozone co-reagents were polycrystalline (001) oriented V_2O_5 as-grown, which they attributed to a combustion-like growth mechanism. In the work presented here, V_4O_9 (010) was obtained in as-grown films, most likely due to the different vanadium source used. After annealing all films were polycrystalline and primarily α-V_2O_5 , with very low concentrations of other vanadium oxides present. The results observed are in good agreement to what was observed in the morphology of the samples as determined by SEM.

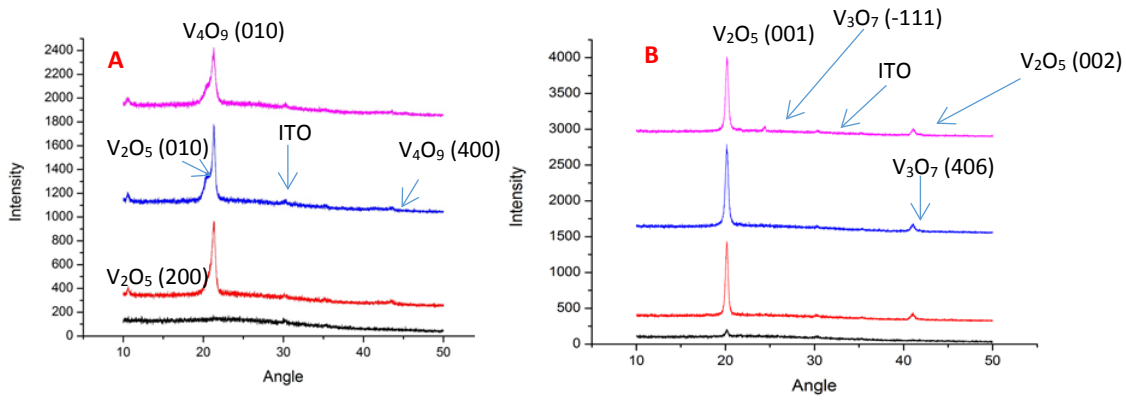

Figure.8.3 XRD patterns of A) As-grown Plasma films B) Films annealed for 1h at 400°C

Grown at: 1) Black-150°C, 2) Red- 200°C, 3) Blue- 250°C, 4) Purple- 300°C

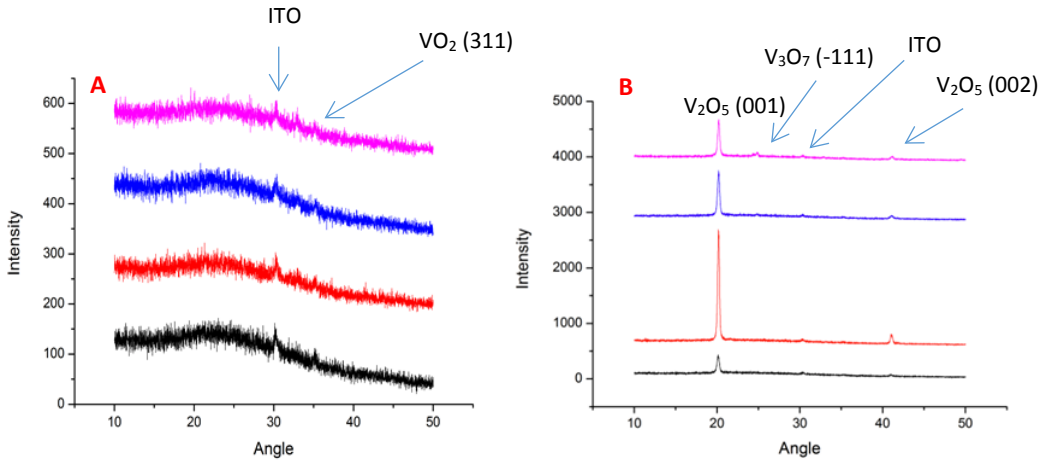

Figure.8.3.1. XRD patterns of A) As-grown Thermal films B) Films annealed for 1h at 400°C

Grown at: 1) Black-Water at 250 °C 2) Red- Water at 300 °C, 3) Blue-Oxygen at 250 °C, 4) Purple- Oxygen at 300°C

8.4 X-ray photoelectron measurements of un-doped V_2O_5 films

X-ray photoelectron spectroscopy measurements were carried out using a Phi Quantera II XPS microprobe.

XPS spectra for thermal and plasma grown pulsed-CVD films deposited at 250 and 300°C are presented in figure 8.4 (a). Spectra are labelled as follows: S1 – oxygen plasma 300°C; S3 – thermal oxygen 250°C and S4 – thermal water 250°C. It was found that all films analysed compared favourably with the V_2O_5 standard as can be seen in figure 8.4 (b). These films have OH groups and H_2O adsorbed on the surface, when compared to the V_2O_5 standard (the range 531-532 eV marked by *). This could be due to the films being exposed to air for a long period of time before measurements were made. V2p prominent XPS transitions at 517.0 eV, for the plasma and thermal samples, display the 5+ oxidation state of vanadium, in good agreement with other XPS studies of V_2O_5[12]. Binding energies and atomic concentrations are displayed in table 8.1. From which it can be seen that the relative atomic oxygen content is roughly constant for both the plasma and thermal samples at around 70%. When samples grown at 250°C are compared, the plasma-grown film was found to have the lowest nitrogen content (relative atomic concentration = 3.4) relative to the thermal-oxygen (5.6) and thermal water (9.0) samples which came from the precursor. This is most likely due to the differences in growth mechanism for these samples. As described by Musschoot[10] in a plasma process a combustion-like growth mechanism dominates, which may have resulted in more efficient decomposition of the vanadium source than a simple thermal decomposition process, as took place during the growth of the other samples. Of the thermally grown samples, a thermal-oxygen process would be more effective than a thermal-water process at decomposing tetrakis(dimethylamino)vanadium, which is reflected in the lower nitrogen content of the thermal-oxygen grown film.

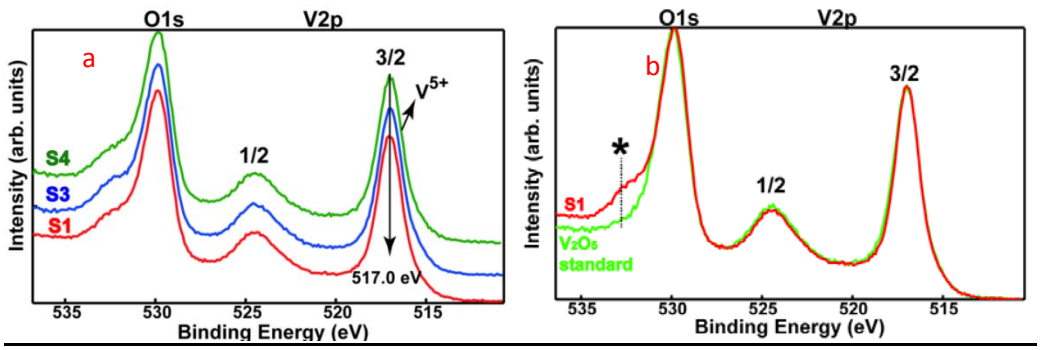

Figure 8.4. (a) O1s and V2p superimposed photoelectron lines for:

1) Red (S1)-Plasma at 300 °C, 2) Blue (S3)- Thermal water at 250 °C, 3) Green (S4)- Thermal oxygen at 250 °C (b) for Plasma at 300 °C and V_2O_5 standard

Sample	Binding energy, eV			Atomic relative concentration		
	O1s	N1s	V2p3/2	O	N	V
Plasma at 300 °C (S1)	529.9 (O^{2-}) - 69.9% 531.3 (OHads) - 18.7% 532.7 (H_2O) - 11.4%	399.8 (amine) – 72.4% 401.4 (quaternary)- 27.6%	517.0	70.5	6.6	22.9
Plasma at 250 °C (S2)	530.1 (O^{2-}) -76.4% 531.6 (OHads) – 20.2% 533.0 (H_2O) - 3.4%	399.7 (amine) – 91.7% 401.2 (quaternary)- 8.3%	517.0	69.9	3.4	26.7
Thermal Water at 250 °C (S3)	529.9 (O^{2-}) – 65.9% 531.3 (OHads) – 19.6% 532.7 (H_2O) – 14.5%	399.8 (amine) – 77.0% 401.4 (quaternary)- 23.0%	517.0	71.3	5.6	23.1
Thermal Oxygen at 250 °C (S4)	529.9 (O^{2-}) - 69.2% 531.3 (OHads) – 20.3% 532.8 (H_2O) – 11.5%	399.7 (amine) – 83.6% 401.4 (quaternary)- 16.4%	517.0	69.9	9.0	22.1

Table 8.1. The element relative concentrations after quantification for the S1-Plasma at 300 °C, S2-Plasma at 250 °C, S3- Thermal Oxygen at 250 °C, S4- Thermal Water at 250°C

8.5 Electrochemical Characterization

Samples were characterized electrochemically using a three-electrode system with Ag/AgCl and Pt as the reference and counter electrodes in a 1M $LiClO_4$/propylene carbonate electrolyte[9]. The scan rate was 10 mV s^{-1} through the voltage range of -1 V to +1 V over scans of 1 and 500 cycles. The area of the working electrode (the ITO on glass substrate with the V_2O_5 coating) was 1 cm^2. The lithium ion intercalation and de-intercalation processes were also studied using chronoamperometry at -1 V and +1 V for a step of 200 s.

I-V curves obtained from pulsed-CVD plasma and thermal samples grown at 250°C and 300°C with post-annealing in air for 1 hour are compared in figure 8.5. As can been seen in figure 8.5 (a) the position and shape of the cathodic and anodic peaks differ depending on the growth temperature of the samples. Positions for anodic/cathodic peaks and current density values are presented in table 8.2. Two sets of peaks were observed corresponding to the α/ε, ε/δ, and δ/ ε, ε/α phase transitions[13,14]. Another anodic peak located at the negative potential region at potential values of -0.39 and -0.3V for the respective temperatures was assigned to lithium ion de-intercalation from the surface which occurs at a faster rate, compared to de-intercalation reactions taking place within the bulk material.[15] Previous studies have shown that peak current density appears to be dependent on many factors such as: surface morphology and surface area[16], film thickness[8], particle size[17], density and porosity of films[18], amount of lithium being intercalated[19] as well as structural changes[20,21,22,23] It was reported that the Li^+ electron paths become longer as the thickness and size of platelets on the surface of the film increase[16], such is the case for increasing film thickness as well.[8,9,24,25] Peak current density values for pulsed-CVD samples were approximately 0.36 and 0.35 $mAcm^{-2}$ – i.e. maximum current density was achieved for 250 and 300°C samples respectively, as per table 8.2.

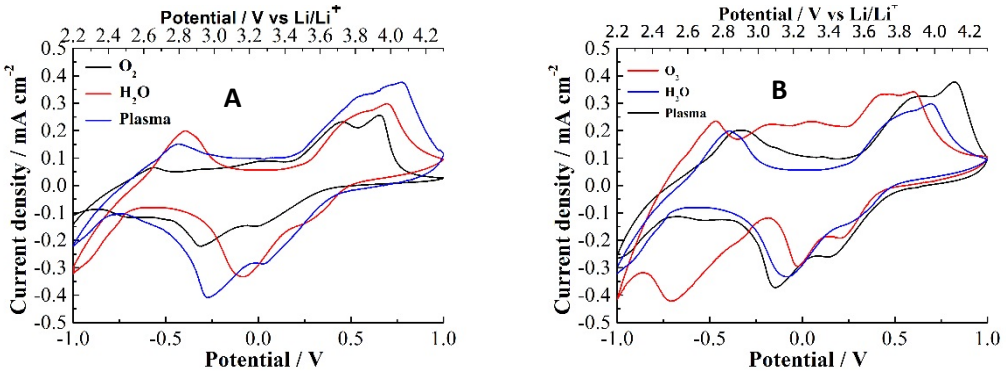

Figure 8.5: Cyclic Voltammogram of Plasma and Thermal ALD samples grown at (A) 250°C and (B) 300°C for 400 cycles. Annealed for 1h at 400°C

Growth Type/ Temperature (°C)	Peak Positions (V)		Current density
	Anodic	Cathodic	(mAcm^{-2})
(Plasma) -250°C	-0.4, 0.57, 0.8	0.05, -0.28	0.36
(O2 Thermal) -250°C	-0.6, 0.45, 0.7	0.01, -0.3	0.25
(H2O Thermal) -250°C	-0.35, 0.71	-0.1	0.28
(Plasma) -300°C	-0.36, 0.6, 0.8	0.2, -0.15	0.35
(O2 Thermal) -300°C	-0.45,0.45 0.6125	0.23, -0.02, -0.7	0.325
(H2O Thermal) -300°C	-0.36, 0.7	-0.1	0.27

Table 8.2. Peak positions and maximum Current Densities from I-V curves from post annealed V_2O_5 samples

As seen before for the higher temperature plasma films the 250°C sample has similar peak positions and maximum current density values. Thermal oxygen samples on the

other hand exhibit three anodic peaks (-0.6, 0.45, 0.7 V) and two cathodic peaks (0.01, -0, 3V) with a current density value of 0.25 $mAcm^{-2}$. Thermal water samples only have two anodic peaks at (-0.35, 0.71V) and one broad cathodic peak (-0.1V), with a current density value = 0.28 $mAcm^{-2}$. Thermal samples display similar phase transitions corresponding to the α/ε, ε/δ, and δ/ ε, ε/α phases along with a one anodic peak due to lithium removal from the vanadium oxide surface, as mentioned previously.

Fig.8.5 (b) is similar to 8.5 (a) with respect to the number of peaks and their positions. Again, three anodic peaks (-0.36, 0.6, 0.8V) and two cathodic peaks (0.2, -0.15V) were seen in plasma samples, three anodic peaks (-0.45, 0.45, 0.6125 V) and three cathodic peaks (0.23, -0.02, -0.7) in thermal oxygen as well as two anodic peaks (-0.36, 0.7V) and one cathodic peak (-0.1V) in thermal water. The thermal oxygen sample grown at 300°C had a very steep and broad cathode peak at -0.75V whose shape and position corresponds to the δ/γ phase transition as seen in the work done by Pan.et al[17].The difference in the peak position for the corresponding anode peak at -0.45V, therefore corresponds to γ/δ phase formation. Thermal water samples show a similar trend in the peak shape, position and current density values to those seen in figure 8.5 (a), which could indicate similar properties of the film. With respect to maximum current density, films grown using a plasma pulsed-CVD process were superior when compared to the thermal-water and thermal-oxygen with maximum values of 0.36 $mAcm^{-2}$ recorded, compared to 0.27 and 0.33 $mAcm^{-2}$ for thermal-water and thermal-oxygen.

For samples grown at 250°C, plasma samples had greatest charge density for both de-intercalation and intercalation with values of 65 $mCcm^{-2}$ and 55 $mCcm^{-2}$ respectively, whereas thermal water and oxygen samples show charge densities of around 15-20 $mCcm^{-2}$, as shown in figure 8.5.2. Plasma films also had the longest time for the lithium ion de-intercalation/ intercalation, with values of 65s/190s compared 22/25s for thermal water and 18/16s for thermal oxygen. Taking into consideration the difference in thickness, crystal coverage, pellet size and the differing amounts of lithium intercalated, such differences are expected.

Data from samples grown at 300°C which is presented in figure 8.5 (b), follows a different trend from previous results. The largest charge density was observed for

thermal water samples with values around 57/57mCcm^{-2} compared to 39/35 mCcm^{-2} and 19/16 mCcm^{-2} for plasma and thermal oxygen samples respectively. The intercalation times followed a similar trend with values of 65s/168s, 51s/155s and 23s/151s. Considering the thickness, crystallite size, peak shape and size in the C-V curve, the thermal water sample would not have been expected to have the largest charge density. These properties are most likely due to microstructural factors, similar to those reported by Østreng et al.[8] in which highly orientated (001) platelets were found to enhance electrical properties. A finding that is in agreement with the XRD analysis previously discussed and shown in figure 8.3.1 which shows that the thermal water films grown at 300°C exhibited the greatest V_2O_5 (001) peak intensity and SEM images of the same sample revealing platelet structures.

Cycling stability is important for the ability to continuously charge/re-charge a battery material without the loss of charge storage properties, hence the more cycles the material remains stable the better it is[11].Cycling stability data for 250°C plasma samples is recorded during 500 cycles for plasma films is presented in figure 8.5.1. When looking at the curves it can be seen that at the very start a maximum current density value of 0.36 mAcm^{-2} is observed the first scan. However, after 100 scans there is evidence of irreversible LiV_2O_5 phase formation which leads to a reduction of current density values. Further cycling resulted in a reduction in maximum current density to 0.15 mAcm^{-2}.

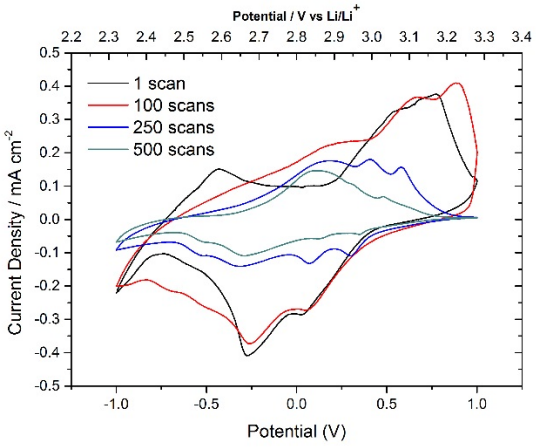

Figure 8.5.1: Cycle stability graph at 1-500 cycles for annealed Plasma samples grown at 250°C

When the material thickness is considered using SEM measurements Discharge capacity measurements performed on samples grown at 250°C did not follow the same general trend. Materials grown at 250°C using a thermal water-process had a discharge capacity of 70µAh/µm.cm^{-2}, while materials grown at 250°C using oxygen plasma had a discharge capacity of 44.45 µAh/µm.cm^{-2}.

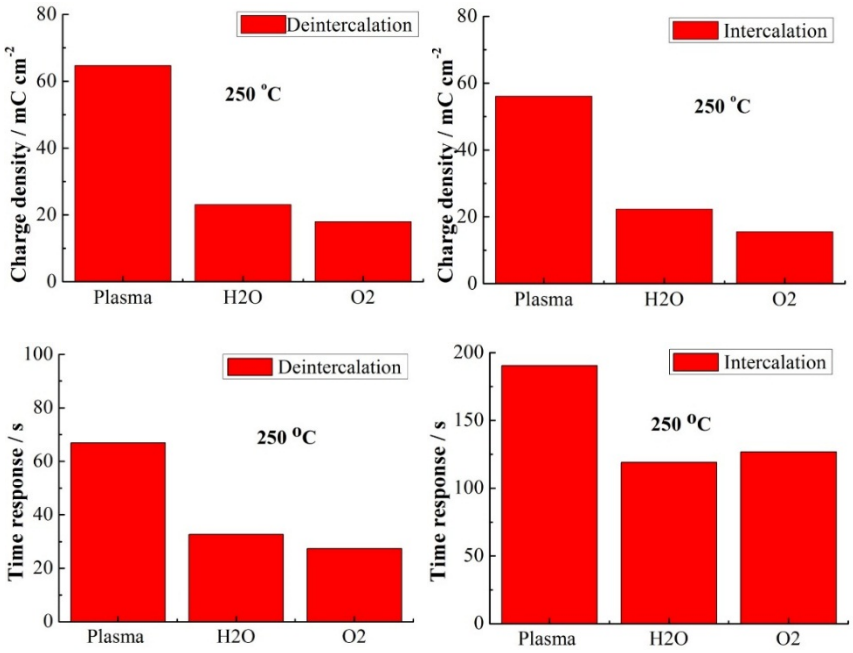

Figure 8.5.2: Charge density vs. Time response bar graphs of Plasma and Thermal ALD samples grown at 250°C for 400 cycles. Annealed for 1h at 400°C

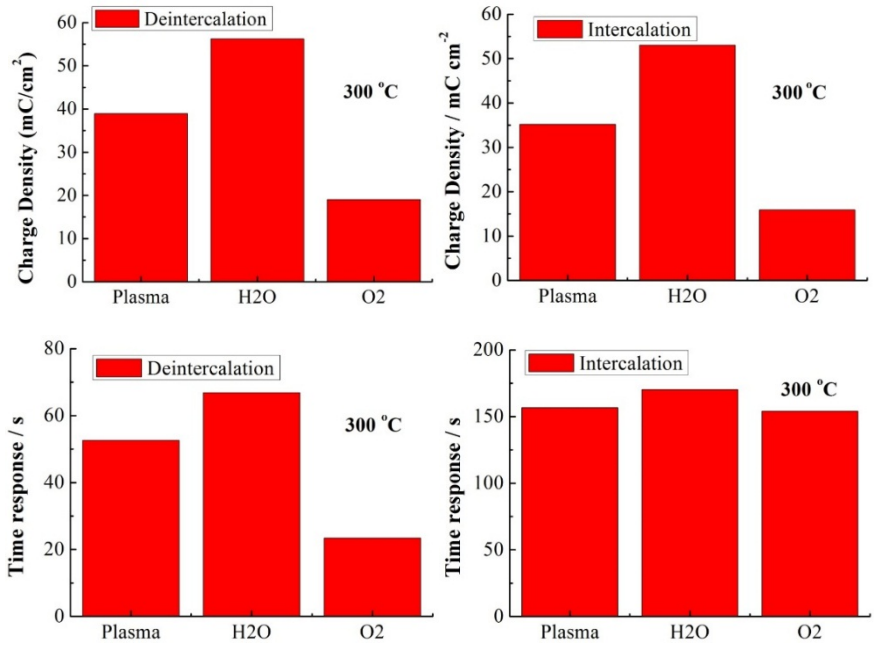

Figure 8.5.3: Charge density vs. Time response bar graphs of Plasma and Thermal ALD samples grown at 300C° for 400 cycles.

8.6 Electrochromic Evaluation:

Lithium ion intercalation into V_2O_5 is an electrochromic reaction[18]. The difference in transmittance between bleached and coloured states (ΔT) values for pulsed-CVD samples grown at 250 and 300°C and annealed in air for 1 hour are presented in figure 8.6. The greatest ΔT in the visible region at 650 nm was observed for plasma grown samples at 250°C which had ΔT = 65%, compared to ΔT = 33% for plasma samples grown at 300°C. For thermal-water films grown at 250°C ΔT at 650nm = 13%, compared to ΔT = 39% for thermal-oxygen films. At 300°C for thermal-water films ΔT = 60%, compared to 30% for thermal-oxygen films. Also, it should be noted that samples grown using a plasma process at 250°C exhibit the greatest transparency while in the bleached state, which is desired for electrochromic window applications. When these results were compared to AACVD grown films which had a ΔT =27% and ΔT =17% at 650nm and 900nm respectively it is clear that a substantial improvement had been made.

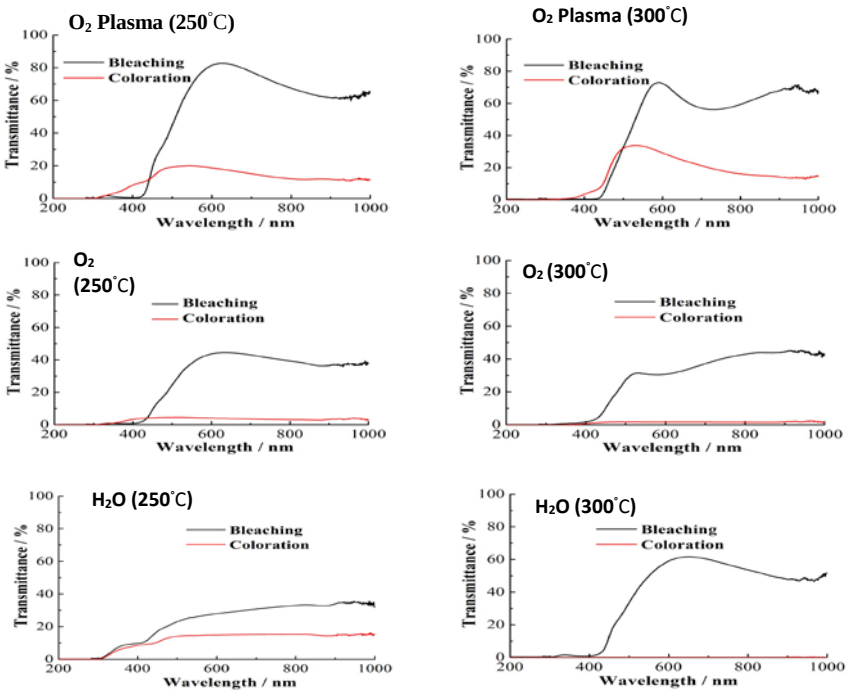

Figure 8.6: % transmittance of Plasma and thermal films grown at 250 °C and 300 °C annealed for 400°C for 1h

8.7 Summary

In Chapter 8 pulsed-CVD of vanadium oxide performed in an ALD deposition tool resulted in growth of uniform, crack free, robust films. Morphological analysis has shown that plasma films have more defined crystal structures which were of a larger size compared to thermal samples. Processes using an argon-oxygen plasma as co-reagent resulted in the growth of polycrystalline V_4O_9. Post annealing for 1hour at 400°C resulted in the desired orthorhombic α -V_2O_5. Thermal processes using oxygen or water as co-reagent resulted in the growth of amorphous films. However, post annealing in air for 1hour at 400°C also resulted in V_2O_5. While crystallinity and the extent of (001) preferred orientation influenced film properties, the nitrogen content of films appears to be a significant factor, as at the optimal growth temperature of 250°C films grown using a plasma process contained least residual nitrogen from the vanadium precursor. This is attributed to the occurrence of a combustion-like mechanism in plasma processes, unlike

the standard thermal-decomposition mechanism occurring in the thermal-oxygen and thermal-water processes.

Electrochemical analysis was performed in order to study lithium intercalation-deintercalation in these materials. The best results were obtained from samples grown at 250°C using a plasma process, post annealed for 1hour at 400°C. These materials had current density = 0.36 $mAcm^{-2}$; charge density = 55 $mCcm^{-2}$ and also the best electrochromic response, $\Delta T = 65\%$ with greatest optical transparency in the bleached state. However, although cycling stability was reasonable at low cycling numbers after 500 cycles the current density of the materials was reduced to approximately 40% of its starting value. When a comparison is made to films grown by AACVD it can be seen that an obvious improvement is made on the film thickness, uniformity, electrochemical and electrochromic properties. When comparing the electrochermical properties of the films it should be noted that those grown by pulsed CVD were very stable over the course of 500 cycles whereas the AACVD grown films were only stable for the first cycle. When looking at the current densities values for plasma film grown by pusled CVD (0.36 $mAcm^{-2}$), 15 weight percent silver-doped films (0.3 $mAcm^{-2}$) and un-doped films (1.26 $mAcm^{-2}$) the cycling stability should be as mentioned taken into consideration. Having done that it is apparent that electrochemical properties were improved. In regards to electrochromic performance it was found that the pulsed CVD films also improved on the electrochromic response with $\Delta T = 65\%$ compared to 27% for un-doped AACVD films. Hence, considering all of the mentioned improvements it can be said with a degree of certainty that the goals mentioned in chapter 6 and 7 were achieved.

In chapter 9 doping methods are examined to further improve the stability of the pulsed CVD films to ensure even more efficient performance.

References:

1) H. B. Profijt, S. E. Potts, M. C. M. van de Sanden, W. M. M. Kessels, *J. Vac. Sci. Technol. A*, **2011**, 29, 50801.
2) D. J. H. Emslie, P. Chadha, J. S. Price, *Coord. Chem. Rev*., **2013**, 257, 3282–3296.
3) C.-H. Kim, I.-C. Rho, S.-H. Kim, I.-K. Han, H.-S. Kang, S.-W. Ryu, H.-J. Kim, *J. Electrochem. Soc*., **2009**, *156*, H685.
4) C. W. Zou, X. D. Yan, D. A. Patterson, E. A. C. Emanuelsson, J. M. Bian, W. Gao, *CrystEngComm*., **2010**, 12, 691–693.
5) A. A. Akl, *Appl. Surf. Sci*., **2007**, *253*, 7094–7099.
6) J. Musschoot, D. Deduytsche, R. L. Van Meirhaeghe, C. Detaverniera, *ECS Trans*., **2009**, *25*, 29–37.
7) X. Rui, Z. Lu, H. Yu, D. Yang, H. H. Hng, T. M. Lim, Q. Yan. *Nanoscale*, **2013**, *5*, 556–560.
8) E. Østreng, K. B. Gandrud, Y.Hu, O. Nilsen, H. Fjellvåg, *J. Mater. Chem. A*, **2014**, *2*, 15044–15051.
9) D. Vernardou, P. Paterakis, H. Drosos, E. Spanakis, I. M. Povey, M. E. Pemble, E. Koudoumas, N. Katsarakis, *Sol. Energy Mater. Sol. Cells*, **2011**, *95*, 2842–2847.
10) J. Musschoot, D. Deduytsche, H. Poelman, J. Haemers, R. L. Van Meirhaeghe, S. Van den Berghe, C.Detavernier, *J. Electrochem. Soc*., **2009**, 156, 122.
11) G. Rubloff, *Chem. Mater*, **2012**, 1255–1261.
12) J. Mendialdua, R. Casanova, Y.Barbaux. *J. Electron Spectros. Relat. Phenomena*, **1995**, 71, 249–261.
13) D. Wei, M. R. J. Scherer, C. Bower, P. Andrew, T. Ryhänen, U. Steiner, *Nano Lett*., **2012**, 12, 1857-1862
14) Y. Liu, M. Clark, Q. Zhang, D. Yu, D. Liu, J. Liu, G.Cao, *Adv. Energy Mater*, **2011**, 1, 194–202.
15) A.Vadivel Murugan, M. V. Reddy, G. Campet, K. Vijayamohanan, *J. Electroanal. Chem*., **2007**, 603, 287–296.
16) K. Lee, Y. Wang, G. Cao, *J. Phys. Chem*., **2005**, 109, 16700–16704.

17) A. Pan, J.-G. Zhang, Z. Nie, G. Cao, B. W. Arey, G. Li, S. Liang, J. Liu, *J. Mater. Chem*., **2010**, 20, 9193.
18) L. Yang, D. Ge, J. Zhao, Y. Ding, X. Kong, Y. Li, *Sol. Energy Mater. Sol. Cells*, **2012**, 100, 251–257.
19) C. Leger, S. Bach, P. Soudan, J.-P. Pereira-Ramos, *J. Electrochem. Soc*., **2005**, 152, A236.
20) N. A. Chernova, M. Roppolo, A. C. Dillon, M. S.Whittingham, *J. Mater. Chem*., **2009**, 19, 2526.
21) C. Delmas, S. Brèthes, M. Mènètrier, *J. Power Sources*, **1991**, 34, 113–118.
22) C. K. Chan, H. Peng, R. D. Twesten, K.Jarausch, *Nano Lett*., **2007**, 7, 490–495.
23) C. Delmas, H. Cognac-Auradou, J. M. Cocciantelli, M. Mènètrier, J. P. Doumerc, *Solid State Ionics*, **1994**, 69, 257–264.
24) D. McNulty, D. N. Buckley, C.O'Dwyer, *J. Power Sources*, **2014**, 267, 831–873.
25) K. Le Van, H. Groult, A. Mantoux, L. Perrigaud, F. Lantelme, R. Lindström, R. Badour-Hadjean, S. Zanna, D. Lincot, *J. Power Sources*, **2006**, 160, 592–601.

Chapter 9: Evaluation of silver-doped V_2O_5 films grown by ALD

9.1 Introduction

As reported in chapter 8, the electrochemical performance of V_2O_5 grown by pulsed CVD needed improvement to make it viable for device applications. The of aim of this experiment was to dope V_2O_5 grown by thermal and oxygen-plasma ALD with silver in order to achieve enhanced electrochemical properties, and thereby identify a suitable material for potential application in lithium battery applications. It should be noted that doping cathode materials with a conductive metal had been shown to significantly improve the intercalation rate, specific capacity and cycling performance[1,2,3,4]

The experimental set-up was the same as in the chapter 8. A new silver precursor 2,2,6,6 Tetramethyl-3,5-heptanedionato silver (I) ($AgC_{11}H_{19}O_2$) was introduced and acted as the dopant metal. Since 250°C was determined to be the optimal growth temperature in chapter 8 it was decided that all films both plasma and thermal would be grown at this temperature. The only things that varied were the co-reagent and energy source (plasma or thermal) and the silver doping percentages which were nominally 0%, 5% and 10% using the metal ratio in an ALD supercycle. A post-annealing step was also used in the same manner as in chapter 8. After film growth and annealing the morphological, structural, electrochemical and electrochromic analysis were carried out. A comparison between the silver doped and un-doped films was then made.

9.1.1 Material Growth:

The growth of V_2O_5 films by ALD was carried out on the Ultratech Cambridge-Nanotech Fiji F200LLC system as was done previously in chapter 8. Tertrakis (dimethylamino) vanadium (IV) ($V(NMe_2)_4$) (a) and 2,2,6,6 Tetramethyl-3,5-heptanedionato silver (I) ($AgC_{11}H_{19}O_2$) (b) (Strem US) as seen in figure 9, were used as

precursors for the growth. Oxygen/Argon gasses were supplied from the in-house gas system and water was supplied from a bubbler. Deposition was carried out on Indium doped tin oxide glass slides with a surface resistivity of 30-60Ωsq^{-1} (Sigma-Aldrich). The substrates had 5x2cm dimensions and were used as received without any further treatment. Growth was carried out using both plasma and thermal water ALD at 250°C for 400 cycles. All of the films except the plasma ALD films (which were polycrystalline) were amorphous as grown and required a post-annealing treatment. The anneal was carried out in air for 1h at 400°C.

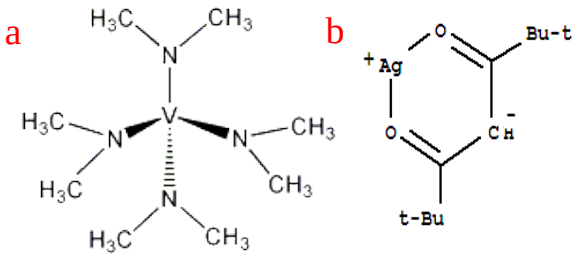

Figure 9: Precursors used for the growth of V_2O_5 films using ALD: a) Tetrakis(dimethylamino) vanadium (TDMAV) b) 2, 2,6,6 Tetramethyl-3,5-heptanedionato silver (I) ($AgC_{11}H_{19}O_2$)

9.1.2 Characterization:

Surface material characterization if not mentioned otherwise was carried out using the same apparatus and techniques as mentioned previously in chapter 6.1

Results and Discussion:

9.2 Morphology

Photographic images displaying annealed films grown using plasma ALD with 5% silver doped can be seen in figure 9.1(a). The annealed thermal water ALD films with the same percentage doping can be seen in figure 9.1 (b). The 10% silver doped films grown at the same conditions were not shown as they are indistinguishable by eye to these mentioned above. As seen before in chapter 8, as-grown plasma films were yellow

due to them being polycrystalline and the thermal water ALD films were dark due to residual carbon on the surface. When comparing 9.1(a) and 9.1(b) it can be seen that no considerable differences between film quality and uniformity could observed hence a very thorough study of morphological, structural and electrochemical properties were required to determine the differences and specific characteristics of the films.

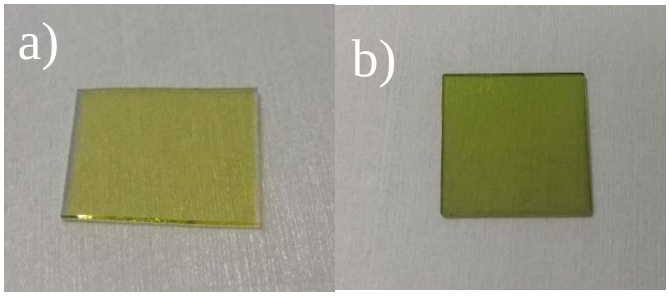

Figure 9.1: Pictures of a) Annealed 5% silver doped plasma ALD films. b) Annealed 5% silver doped thermal water ALD films. Films are indistinguishable by eye the annealed un-doped ALD films in chapter 8, figure 8.1.

Plan view SEM images of 5% and 10% plasma and thermal water films are displayed in figure 9.1.1. Films were conformal and uniform over the entire substrate surface with no significant features that could be used to distinguish between the films. Cross section transmission electron microscopy was performed to determine film thickness. Images are presented in figures 9.1.2 – 9.1.4; thickness values are presented in table 9.

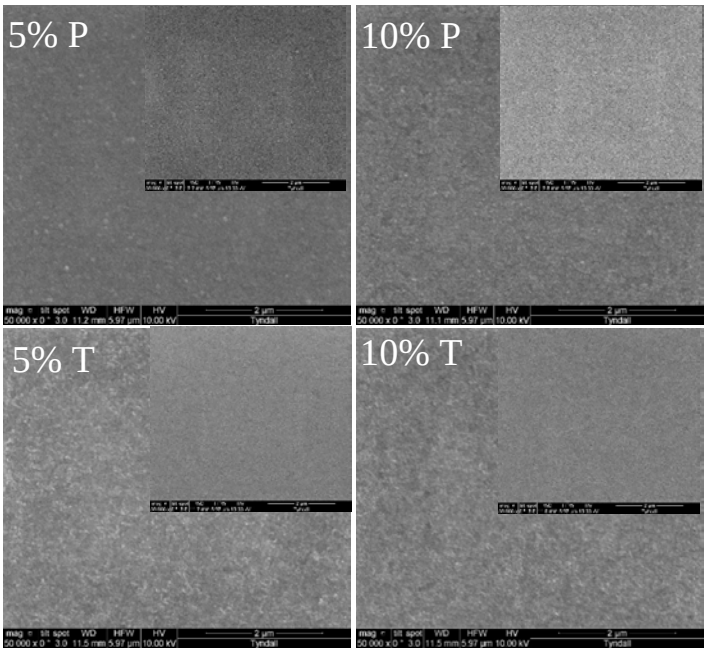

Figure 9.1.1. Representative SEM for 5% Plasma ALD films grown for 400 cycles with further annealing at 400 °C for 1h (Insert is un-annealed sample). The surface is seen to be covered with crystallites for the annealed samples and is amorphous and devout of any features for the insert. The 5% and 10% Thermal and 10% Plasma ALD films had similar SEM's with no noticeable features that would allow to distinguish from one another.

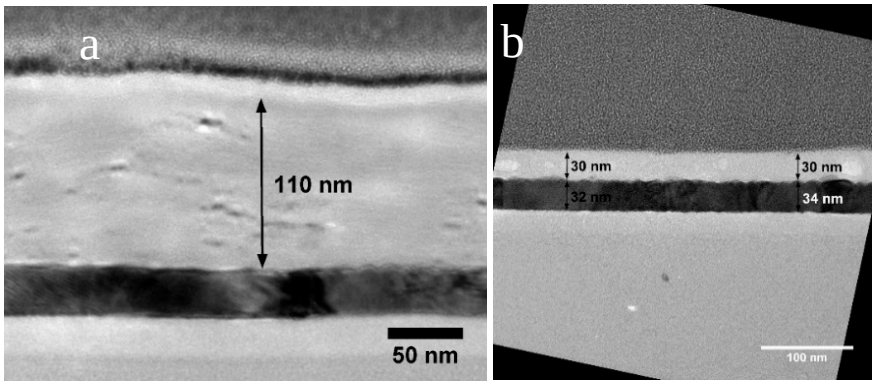

Figure 9.1.2. TEM images of un-doped (a) Plasma and (b) Thermal H_2O ALD films grown at 250°C for 400 cycles. With further annealing at 400 °C for 1h. A thickness of 110 nm could be observed for the Plasma ALD films and a thickness of 30 nm could be observed for the thermal water ALD films.

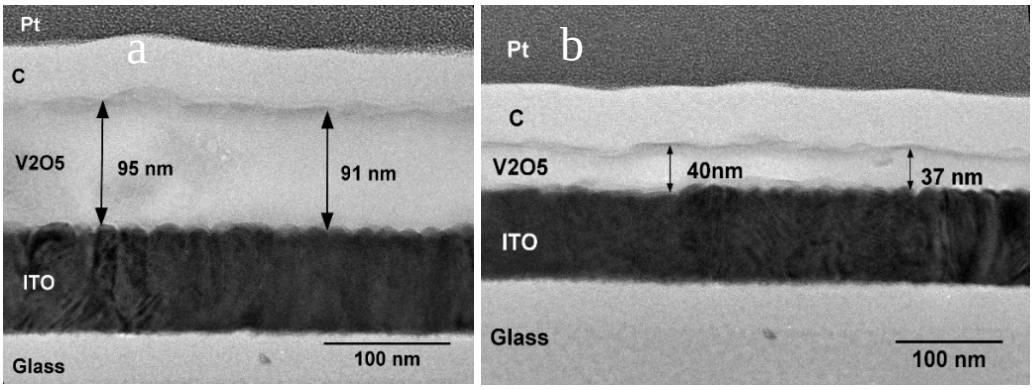

Figure 9.1.3: TEM images of 5% and 10% silver doped plasma ALD samples grown at 250°C for 400 cycles and annealed for 1h at 400°C. As can be seen the film thickness decreases with increasing percentage of silver doping with average values of around 93 nm for the 5% and 38.5 nm for 10%.

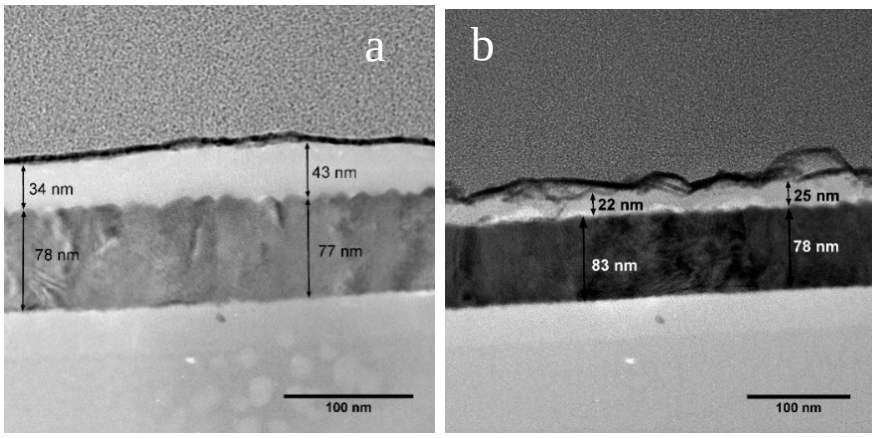

Figure 9.1.4. TEM images of 5% and 10% Thermal H_2O ALD films grown at 250°C for 400 cycles. With further annealing at 400 °C for 1h. The trend for reduction of thickness with increasing percentages of silver doping is continued with the thermal ALD samples with average values of 28.4 and 24.6 nm for 5% and 10% silver doping respectively.

The 'growth per cycle' (GPC) based on the thickness of annealed samples was calculated. GPC values for the silver doped plasma grown thin films were 2.8, 2.3 and 1.0 Å/cycle for 0%, 5% and 10% respectively. For thermally grown films the values were 0.8, 1.0 and 0.6 Å/cycle for 0%, 5% and 10% silver respectively. For thermal films a slight increase in growth rate was observed, with initial addition of silver. On increasing % silver content from 5% to 10%, the growth rate decreased to 0.6 Å/cycle.

Plasma grown films on the other hand show a significant reduction in growth rate with increasing silver content. These data are presented graphically in figure 9.2 and in table 9.

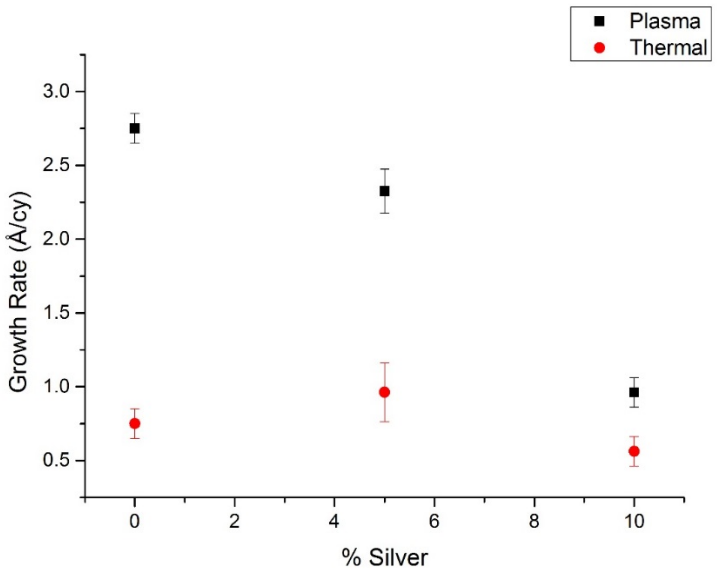

Figure 9.2. Graph of growth rate vs percentage of silver doping of 0%, 5% and 10% silver doped Plasma and thermal H_2O ALD grown films. Thin films were grown for 400 cycles. A post annealing step was carried out for 1h at 400°C. The growth rate for plasma ALD films decreases rapidly with increasing silver doping. A slight increase in the growth rate is observed for the 5% thermal water ALD films which subsequently decreases upon further silver loading.

% Silver	0%	5%	10%	
Thickness (nm)	110	93	38.5	**Plasma ALD**
Thickness (nm)	30	38.5	22.5	**Thermal ALD**
Error (Å/cycle)	0.1	0.15	0.1	**Plasma ALD**
Error (Å/cycle)	0.1	0.2	0.1	**Thermal ALD**

Table 9: Thicknesses of Plasma and Thermal annealed films as presented in figures 4-6

9.3 Crystallography

X-ray diffraction patterns for 5 and 10% silver doped samples, grown with oxygen plasma (both as-grown and with a post annealing step done at 400°C for 1hour) are presented in figure 9.3. Four peaks were observed for both as-grown and annealed samples. The peak at 20.15° (2Θ) was assigned to (001) α-V_2O_5[5] whereas the peaks at 30.22° 35.25° and 50.69° were assigned to the ITO substrate. In general, x-ray diffraction peak intensity increased on annealing, with 5% silver doped films having a higher intensity V_2O_5 peak than the 10% silver doped films. These results are similar to those observed in the literature[6] in which silver-doped films were polycrystalline as-grown and a post-annealing step was required to induce film crystallinity.

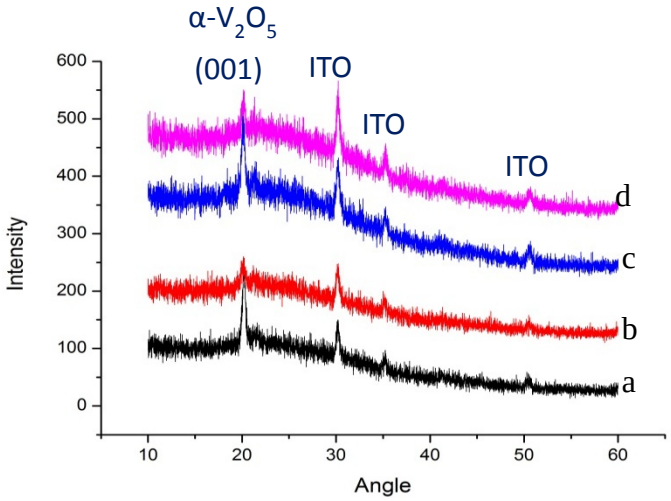

Figure 9.3: XRD of annealed and un-annealed 5 and 10% silver doped plasma films. Films were annealed for 1h at 400°C. a) 5% un-annealed b) 10% un-annealed c) 5% annealed d) 10% annealed. High intensity α-V_2O_5 (001) peaks are observed along with substrate peaks.

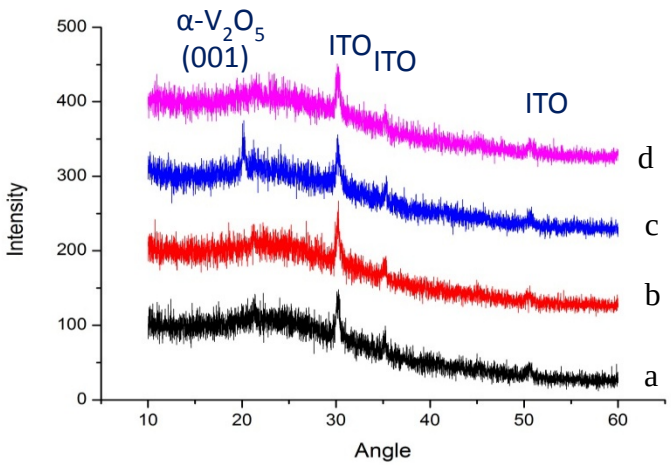

Figure 9.3.1: XRD of annealed and un-annealed 5 and 10% silver doped thermal films. Films were annealed for 1h at 400°C. a) 5% un-annealed b) 10% un-annealed c) 5% annealed d) 10% annealed. Lower intensity α-V_2O_5 (001) peaks are observed along with substrate peaks.

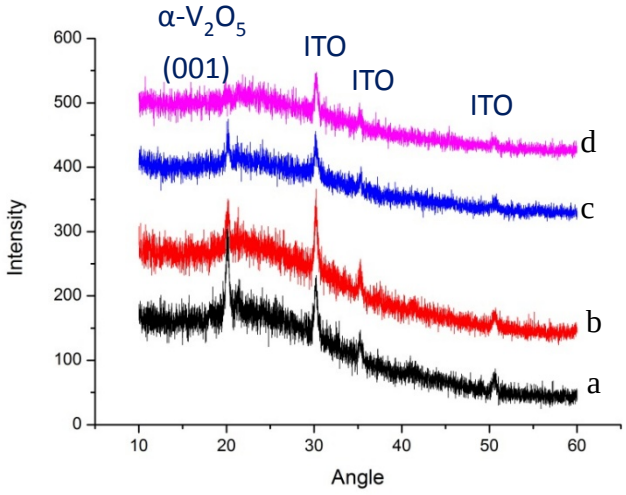

Figure 9.3.2: XRD of annealed 5 and 10% silver doped plasma and thermal films. Films were annealed for 1h at 400°C. a) 5% annealed Plasma ALD films b) 10% annealed Plasma ALD c) 5% annealed thermal water ALD films d) 10% annealed thermal water ALD films. As seen before α-V_2O_5 (001) peaks are observed along with substrate peaks.

X-ray diffraction patterns for films grown by thermal ALD, with are presented in figure 9.3.1 and a comparison of annealed thermal and plasma grown films are presented, for ease of comparison, in figure 9.3.2. Films prepared by thermal ALD were amorphous 'as-grown' and a post annealing step was therefore required to induce crystallization. A low intensity V_2O_5 peak was observed in the diffraction pattern of the 5% silver doped film, with no such peak observed for the 10%. Crystallite size calculations were attempted using the Scherrer method but the XRD scans was not of sufficient signal to noise to to elucidate crystallite size.

The most intense (001) α-V_2O_5 diffraction was observed in XRD patterns of 5% silver doped films grown using an oxygen-plasm process and annealed at 400°C in air for one hour.

9.4 Raman of Ag-doped V_2O_5 films

Raman spectroscopy was performed in a Nicolet Almega XRmicro-Raman system using a 514nm laser line at an incident intensity of 10mW μm-2, i.e. low enough to prevent any structural change to either the coating or the under-line substrate

Raman spectra for 5% and 10% silver doped plasma and thermal films growth for 400 cycles at 250°C which underwent a post-anneal treatment are presented in figure 9.4 (A) and (B). An un-doped plasma sample grown at 150°C using the same methods as described in chapter 8 was inserted for comparative purposes.

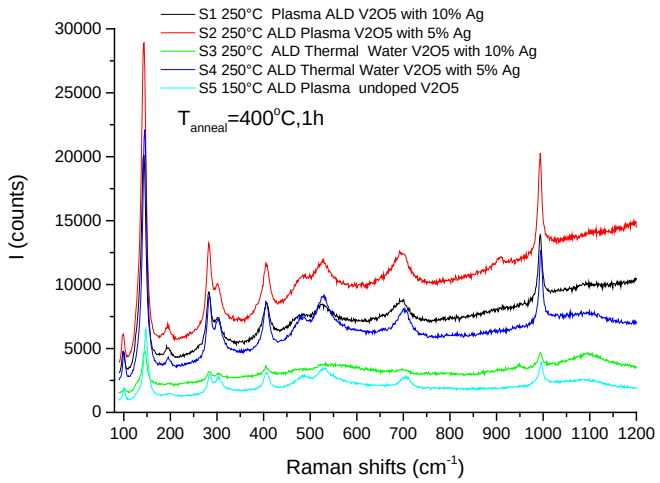

Figure 9.4 (A): Raman spectra of annealed films grown at 250 °C: Black- 10% Ag Plasma, Red- 5% Ag Plasma, Green- 10% Thermal Water, Blue- 5% Ag Thermal Water, Navy- un-doped plasma film grown at 150 °C

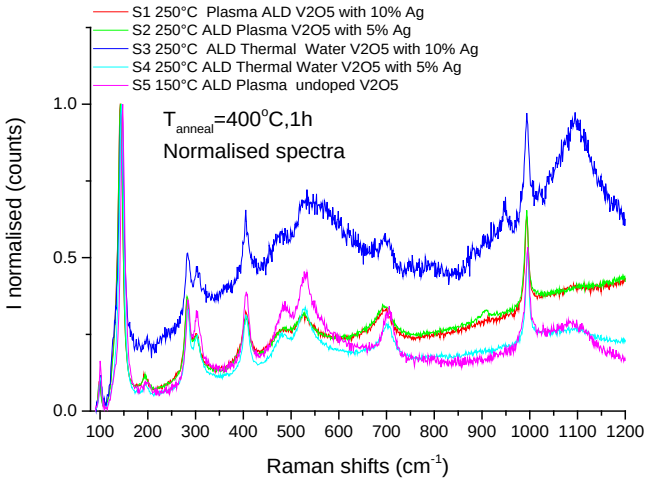

Figure 9.4 (B): Normalised Raman spectra of annealed films grown at 250 °C: Black- 10% Ag Plasma, Red- 5% Ag Plasma, Green- 10% Thermal Water, Blue- 5% Ag Thermal Water, Navy- un-doped plasma film grown at 150 °C

Raman high frequency vibration modes characteristic of V_2O_5 can be seen at 144 cm^{-1} and 995 cm^{-1}. These vibration modes correspond to the vibrations of the V=O atoms and –O-V-O-O-V bonds respectively and are indicative of a layered V_2O_5 structure.[6,7] Other

vibrations at 700, 526, 480, 403, 302, 282, 195 and 105 cm^{-1} were also observed and were similar to those observed in other studies.[8,9]. The intensity trends of the Raman spectra follow a similar trend to the intensity of x-ray diffraction patterns for plasma and thermal films seen in figures 9.3-9.3.2. A slight peak shift was also observed compared to the reference un-doped V_2O_5 sample. No silver vibration peak was observed which suggests that the dopant is not uniformly distributed in the bulk and remaining as a laminate or not present; uniform dopant distribution is typically observed when using other material deposition techniques such as sol-gel or PLD. [6,10]

9.5 X-ray photoelectron spectroscopy of Ag-doped V_2O_5 films

XPS spectra for 5 % and 10% silver doped thermal and plasma grown ALD films are presented in figure 9.5(a) and 9.5(b). Films analysed were a close match to the V_2O_5 standard, as shown in figure 9.5 (b). Prominent V2p XPS transitions at 517.0 eV, corresponding to vanadium 5+ oxidation state, were observed for both plasma and thermal samples, and have been widely discussed in studies of V_2O_5[11].

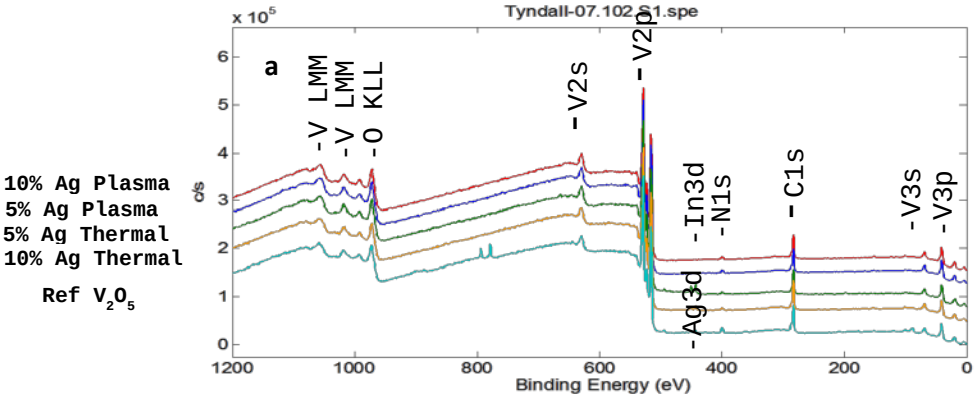

Figure 9.5 (a) V2p superimposed photoelectron lines for:

1) Red- 10% Ag doped Plasma, 2) Blue- 5% Ag doped Plasma, 3) Green- 10% Ag doped Thermal 4) Orange- 5% Ag doped Thermal and V_2O_5 standard.

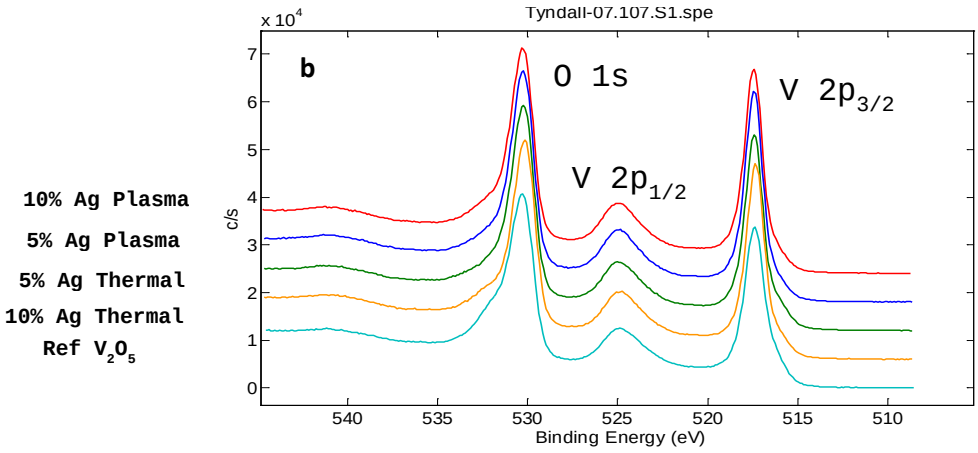

Figure 9.5 (b) O1s and V2p superimposed photoelectron lines for:

1) Red- 10% Ag doped Plasma, 2) Blue- 5% Ag doped Plasma, 3) Green- 10% Ag doped Thermal 4) Orange- 5% Ag doped Thermal and V_2O_5 standard.

Atomic concentrations are presented in table 9.1. The oxygen content is similar in both the plasma and thermal samples, ranging from 51.8 – 54.1 atomic %. The 5% plasma samples showed an increasing content of vanadium of 20.4% compared to 19.9% in the 10% silver doped plasma samples. Thermal water samples show even lower values of 19.4% and 19.2%. Relatively high percentages of carbon were detected; as no surface pre-treatment was carried out prior to analysis, a significant contributor to these values would be atmospheric carbon contamination. The amount of silver was below detection levels, which could indicate that it is not uniformly distributed in the V_2O_5 films or that it might not be present at all.

Atomic Concentration %

Sample ID	S1	S2	S3	S4	Ref V_2O_5
V $2p_{3/2}$	19.9	20.4	19.4	19.2	17.0
O 1s	53.4	54.1	53.5	51.8	50.6
C 1s	23.6	22.6	23.3	26.3	26.9
N 1s	1.9	1.8	1.6	1.3	3.4
Ag $3d_{5/2}$	<0.1	<0.1	<0.1	<0.1	<0.1
Cl 2p	<0.1	0.1	0.4	<0.1	<0.1
Si 2p	<0.1	0.9	1.0	1.2	1.3
In $3d_{5/2}$	<0.1	<0.1	0.7	0.2	0.1
Sn $3d_{5/2}$	<0.1	<0.1	0.1	<0.1	<0.1

Table 9.1: The element relative concentrations after quantification for the samples

S1-10% plasma, S2-5% plasma, S3-10% thermal, S4-5% Thermal

9.6 Electrochemical Characterization

The same method of testing that was done in chapter 8 was used to test silver doped ALD samples as well. Even though the same α/ε, ε/δ, and δ/ ε, ε/α phase transitions were observed as in chapter 8, it should be noted that the percentage of silver introduced during film growth in this chapter, had a significant effect on the curve shape and current density values, as observed in the voltammograms in figures 9.6 (a) and 9.6 (b). When a comparison is made of the 0%, 5% and 10% silver doped plasma films in figure 9.6 (a), a trend is observed, where there are three anodic and two cathodic peaks present. The peak positions for anodic and cathodic peaks are presented in table 9.2 Anodic peaks for all three percentages of silver doping, located in the negative potential regions at: -0.43V, -0.4V and -0.32V, correspond to the deintercalation of lithium ions from the surface, which happens at a faster rate than the bulk, this could be due to the different speeds at which redox reactions of vanadium near the electrode-electrolyte interface and at the grain boundaries takes place, when compared to the bulk vanadium. If a

comparison of current densities is made between the oxygen plasma samples, the 5% silver doped samples possess the largest current density of 1 $mAcm^{-2}$compared to 0.52 $mAcm^{-2}$ for 10% silver doped and 0.36 $mAcm^{-2}$ for 0% silver doped as seen in table 9.2.

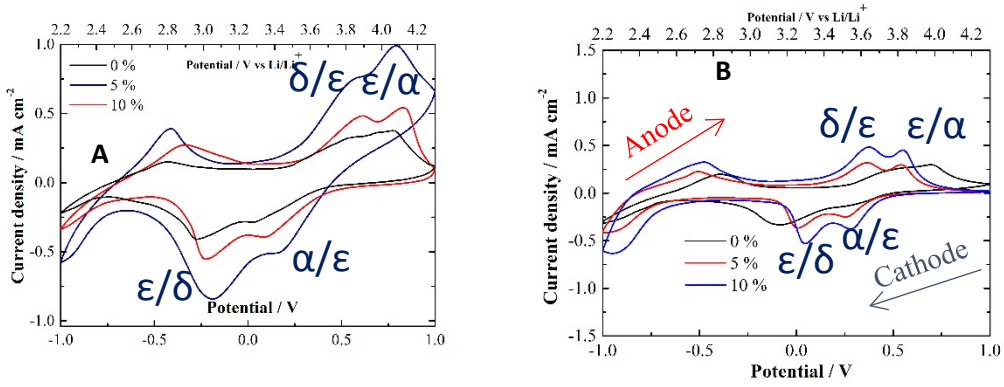

Figure 9.6 (A) and 9.6 (B): 9.6 (A) Cyclic Voltammogram of: (Black)-0%, (Blue)-5%, (Red)-10% silver doped Plasma 9.6 (B): (Black)-0%, (Blue)-5%, (Red)-10% silver doped Thermal water ALD samples grown at 250C° for 400 cycles. Annealed for 1h at 400°C

CV curves obtained from thermal water samples are presented in figure 9.6 (b). A different trend was observed here. The best current density values were observed for 10% silver doped films with a value of 0.48 $mAcm^{-2}$compared to 0.27 $mAcm^{-2}$ for 5% samples and 0.25 $mAcm^{-2}$ for 0% samples as seen in table 9.2. It can be seen that the presence of the silver precursor in the growth process results in increased current density values.

% Silver Doping	Peak Positions (V) (Anodic)	Peak Positions (V) (Cathodic)	Max Current density ($mAcm^{-2}$)	Max Current Density ($mAcm^{-2}$) (500^{th} cycle)	Discharge Capacity ($\mu Ah/\mu m.cm^{-2}$)
0% Plasma	-0.43,0.57,0.76	0.05, -0.3	0.36	0.15	47
5% Plasma	-0.4,0.575,0.8	0.2,-0.195	1.0	0.85	67
10% Plasma	-0.32,0.625,0.85	0.1,-0.22	0.52	0.31	142
0% Thermal H_2O	-0.4,0.74	-0.1	0.25	0.125	70
5% Thermal H_2O	-0.51,0.37,0.575	0.25,0.01	0.27	0.15	91
10% Thermal H_2O	-0.475,0.375,0.58	0.275,0.9	0.48	0.22	186

Table 9.2. Peak positions, Max Current Densities (1-500 cycles) and Discharge capacities of ALD plasma grown films and of ALD thermal water grown films.

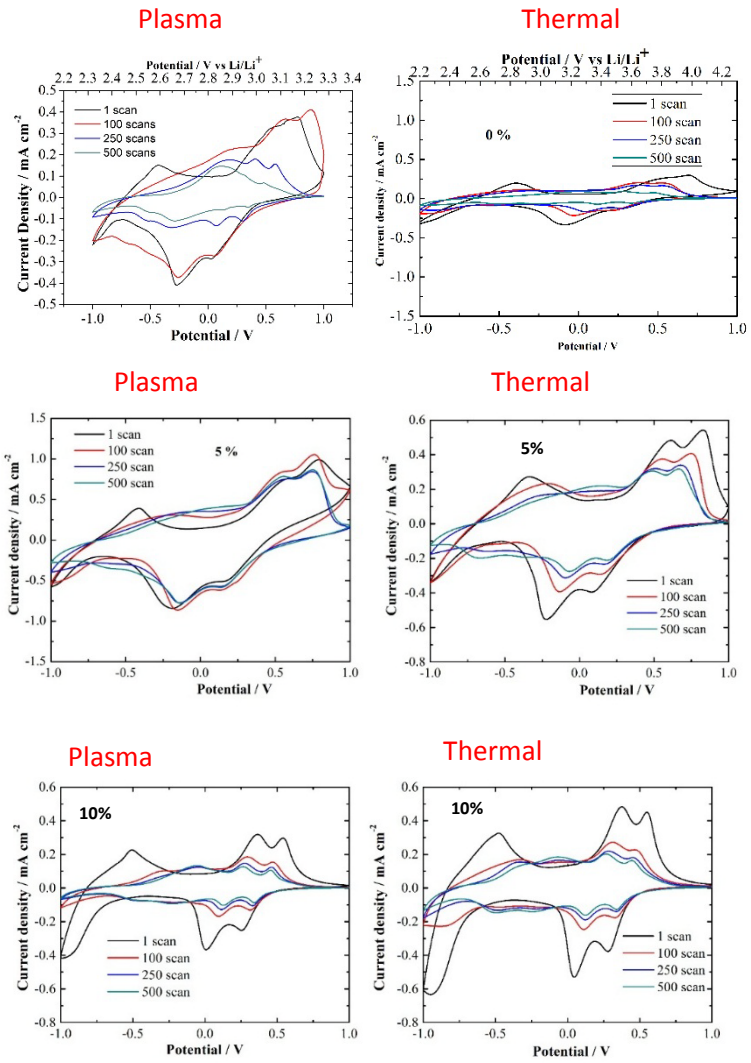

Figure 9.6.1: Cyclic Voltammograms of 0, 5 and 10% silver doped Plasma and Thermal ALD samples grown at 250C° for 400 cycles. Annealed for 1h at 400°C

Cycling stability data recorded during 500 cycles for all materials are presented in figure 9.6.1 and in table 9.2. When CV curves from un-doped plasma and thermal water samples are compared, it is clear that plasma grown samples exhibit increased current density in the first scan (0.36 $mAcm^{-2}$). However, after 100 scans there is evidence of irreversible LiV_2O_5 phase formation. Further cycling resulted in a reduction in maximum current density to 0.15 $mAcm^{-2}$, this is in good agreement to what was seen in chapter 8. Un-doped thermal samples had a lower maximum current density for the first scan (0.25

$mAcm^{-2}$). Performance then decreased with repeated cycling to approximately the same current density as the plasma grown material to 0.125 $mAcm^{-2}$.

Doping with 5% silver resulted in increased maximum current density. In the case of thermally grown material, the increase was minor, to 0.27 $mAcm^{-2}$, however a significant increase to 1.0 $mAcm^{-2}$ was observed for films grown with oxygen plasma. Films grown with oxygen plasma exhibited excellent cycling stability, with a current density of 0.85 $mAcm^{-2}$ recorded after 500 cycles. Thermal water films on the other hand, after 500 cycles had a current density of 0.15 $mAcm^{-2}$.

Increasing the dopant level to 10% silver resulted in a decrease in maximum current density. Oxygen plasma films exhibited a maximum current density of 0.52 $mAcm^{-2}$ for the first cycle whereas thermal water films had a lower values of 0.48 $mAcm^{-2}$. Features typical of irreversible Li-V_2O_5 were observed in both voltammograms between -0.8 and -1.0V[12]. Consequently, there was considerable deterioration in performance with repeated cycling. Films grown with oxygen plasma had a current density of 0.31 $mAcm^{-2}$ recorded after 500 cycles. After 500 cycles thermally grown films had a current density of 0.22 $mAcm^{-2}$.

In summary, 5% silver doped V_2O_5 grown by ALD with oxygen-plasma as a co-reagent, annealed in air for one hour at 400°C resulted in the best material in this study. Maximum current density for it was 1.0 $mAcm^{-2}$ for the first cycle. These materials exhibited excellent cycling stability, retaining a current density of 0.85 $mAcm^{-2}$ after 500 cycles. Chronoamperometric measurements, presented in figures 9.6.2 and 9.6.3, are in agreement as the 5% silver doped material exhibits the greatest current density without a decrease in performance due to switching.

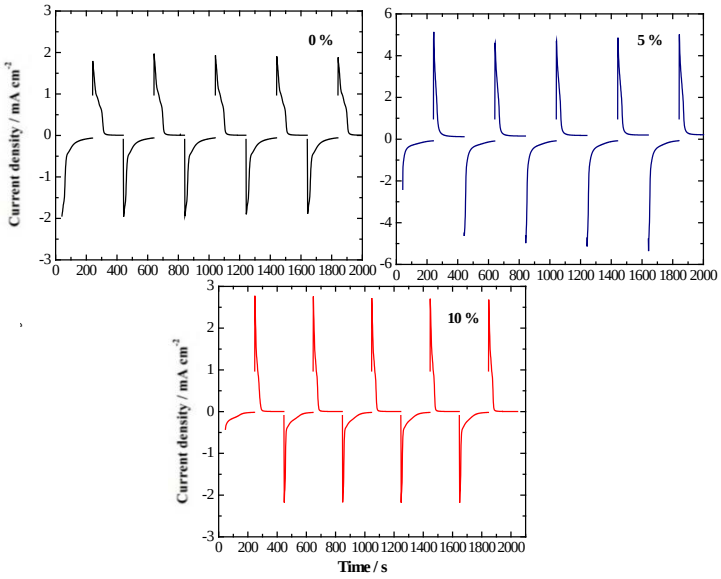

Figure 9.6.2: Chronoamperometric response recorded at -1V and +1V for an interval of plasma ALD films grown at 250 °C with silver doping of 1) Black- 0%, 2) Blue-5%, 3) Red- 10% , annealed for 1h at 400 °C

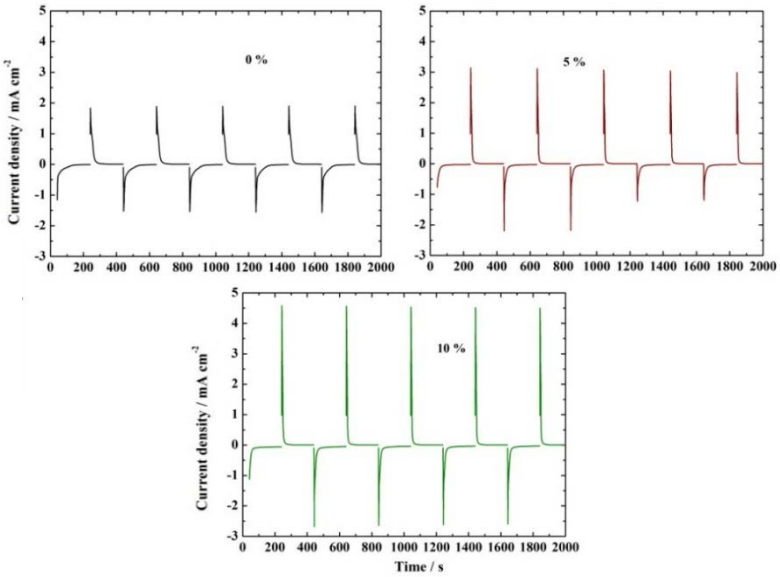

Figure 9.6.3: Chronoamperometric response recorded at -1V and +1V for an interval of 200s of thermal ALD films grown at 250 °C with silver doping of 1) Black- 0%, 2) Red- 5%, 3) Green- 10%, annealed for 1h at 400 °C

Discharge capacity measurements performed on samples followed a different trend. Data is presented in table 9.2. Materials grown using the thermal-water process had

discharge capacities of 70, 91 and 186 μAh/μm.cm^{-2}, for 0, 5 and 10% silver doped samples respectively. Materials grown using an oxygen-plasma process had discharge capacities of 47, 67 and 142 μAh/μm.cm^{-2}, for 0, 5 and 10% silver doped samples respectively. Within each sample set, discharge capacity increased with increasing concentration of silver dopant employed during the growth process as to be expected. Thermally grown samples were found to have greater discharge capacities than their oxygen-plasma grown counterparts.

9.7 Electrochromic Characterization

As mentioned previously, lithium ion insertion into V_2O_5 is usually accompanied by a colour change and is thus defined as an electrochromic reaction. The difference in percentage transmittance between the bleached and the coloured states (ΔT) was measured for plasma and thermal silver doped samples. Figure 9.7 (A) compares the ΔT values of 0%, 5% and 10% silver doped plasma films, it is evident that the insertion of silver during the growth strongly inhibits the transmittance of the films in the visible region centred at 650nm. The insertion of silver changes the way films grow and affects the morphology of the samples, thus even though a better electrical results is seen for the silver doped films a poorer electrochromic response is observed. A similar, yet more severe case was observed for the thermal water samples in figure 9.7 (B).

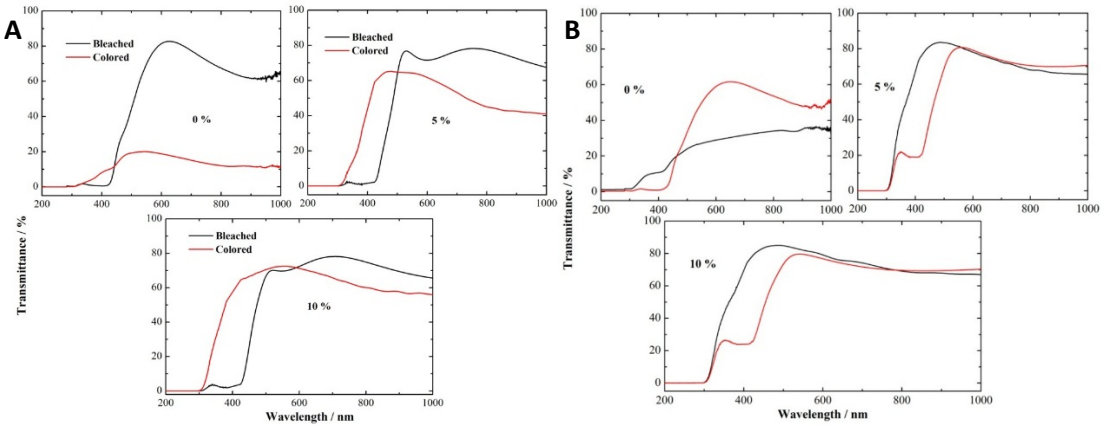

Figure 9.7: % Transmittance of: (A) of Oxygen-plasma films with 0%, 5% and 10% doping (B) % Transmittance of Thermal Water films with 0%, 5% and 10% doping. Annealed for 400°C for 1h. (Black-Bleached), (Red-Coloured)

For the 0% silver doping thermal samples the ΔT was only observed over a very short wavelength range of approximately 320-420nm unlike the plasma samples which are observed in the visible region of 600-800nm. The 0% silver doped thermal samples also showed poor electrical properties in terms of current density, discharge capacity and the overall amount of lithium ions intercalated/deintercalated. The 5% and 10% silver doped thermal water samples showed poor ΔT values as well, in this case it was not only due to poorer electrochemical properties but also due film thickness, as in the case of the 10% silver doped samples which did not even have any vanadium peaks in the x-ray diffraction patterns in figure 9.3.2. It should be noted however that upon silver doping there appears to be a shift in the wavelength for plasma films making them more similar to thermal water films in their electrochromic behaviour. Taking this into consideration it is evident that these films could not be used for electrochromic applications and that un-doped V_2O_5 films in chapter 8 would be more suitable for this.

9.8 Summary

Conformal, crack-free silver doped V_2O_5 films were successfully grown using oxygen-plasma and thermal water processes. A reduction in growth rate (GPC) was observed for both cases with increasing silver content. Thermal-water grown films were amorphous 'as-grown' and were polycrystalline V_2O_5 after annealing. Oxygen-plasma grown films were polycrystalline V_2O_5 'as-grown', but still required annealing to optimise film properties. Raman and XPS spectra matched a V_2O_5 standard . Silver was not present in detectable quantities in XPS spectra recorded. It is possible that not all the silver pulsed into the ALD reaction chamber was incorporated into the V_2O_5 films and that the silver content is therefore below detectable limits. Although silver does clearly influence the film growth, there are several possibilities why it was not detected. It is possible that silver could be lost during the anneal step or quite probably not even incorporate into the film during grown. It is however also known that silver is highly mobile within the Li-V_2O_5 material system and is intercalated between V_2O_5 layers in a similar manner as lithium[13] and consequently is often difficult to characterise quantitatively. However, thant silver doping clearly enhanced the electrical properties of films grown as shown by cyclic voltammetry and chronoamperometry, (the discharge capacity of materials grown by thermal and plasma processes was seen to increase with increasing silver dopant concentration) suggests that silver is present in V_2O_5 films in proportion to the quantity pulsed into the ALD reactor during the growth process. The improvement of electrochemical properties is especially evident when results are compared to those in chapter 8. Thermally grown materials had greater discharge capacities than their oxygen-plasma grown equivalents and that discharge capacities increased with increasing silver concentration. However oxygen-plasma grown materials, in particular 5% silver doped V_2O_5, exhibited greater current density and cycling stability values. Similar behaviour was not exhibited by films grown using a thermal-water process. Electrochromic properties of the films were found to be diminished with the addition of silver. Both oxygen plasma and thermal water samples proved to be inneficient electrochromic materials when compaared to the un-doped plasma samples from chapter 8.

Therefore, of the materials studied it was concluded that nominally 5% silver doped V_2O_5 films grown using oxygen plasma and annealed at 400ºC for 1 hour were best suited for use as a working electrode in lithium ion battery applications but not for electrochromic applications.

References:

1) A. Gies, B. Pecquenard, A. Benayad, H. Martinez, D. Gonbeau, H. Fuess, A. Levasseur, *Thin Solid Films*, **2008**, 516, 7271–7281.
2) F. Coustier, J. Hill, B. B. Owens, S. Passerini, W. H. Smyrl, *J. Electrochem. Soc*., **1999**, 146, 1355–1360.
3) M. V Reddy, G. V. S Rao, B. V. R. Chowdari, *Chem. Rev.,* **2013**, 5364–5457.
4) K. J. Takeuchi, A. C. Marschilok, S. M. Davis, R. A. Leising, E. S. Takeuchi, W. Dri, *Coord. Chem. Rev*, **2001**, 219, 283–310.
5) A. A. Akl, *Appl. Surf. Sci*., **2007**, *253*, 7094–7099.
6) Y. Iida, Y. Kanno, *J. Mat. Proc. Techn*., **2009**, 209, 2421–2427.
7) L.Abello, E.Husson, *Spectrochim. Acta*, **1983,** Vol 39A, No.7, 641-651
8) K. Le Van, H. Groult, A. Mantoux, L. Perrigaud, F. Lantelme, R. Lindström, R. Badour-Hadjean, S. Zanna, D. Lincot, *J. Power Sources*, **2006**, 160, 592–601.
9) C. Navone, M. Smirnov, *Chem. Mater*, **2008**, 20, 1916–1923.
10) A. Pan, J.-G. Zhang, Z. Nie, G. Cao, B. W. Arey, G. Li, S. Liang, J. Liu, *J. Mater. Chem*., **2010**, 20, 9193.
11) J. Mendialdua, R. Casanova, Y. Barbaux, *J. Elect. Spectr. Relat. Phen*., **1995**, 71, 249–261.
12) J. M. Cocciantelli, M. Menetrier, C. Delams, J. P. Doumerc, M. Pouchard, M. Brouselly, J. Labat, *Solid State Ionics*, **1995**, 2738, 143–150.
13) R. S. Diggikar, V. M. Dhavale, D. B. Shinde, N. S. Kanbargi, M. V. Kulkarni, B. B. Kale, *RSC Adv*., **2012**, 2, 3231.

Chapter 10: Summary and Future work

The work done in this thesis focused on the growth of vanadium pentoxide films for the use in electrochromic and battery applications.

For CVD a temperature of 400°C, growth time of 60 minutes and post-annealing were found to be optimal for film deposition and showed promising results with current densities = 1.26 $mAcm^{-2}$, charge densities = 30 $mCcm^{-2}$ and ΔT of 27% and 17% at 650 and 900nm respectively. Some drawbacks were encountered such as: film non-uniformity, poor control over film growth, poor cycling stability and lower than required transmittance.

In an effort to improve the electrochemical properties the doping of films with silver was implemented. Film growth time was kept constant whereas growth temperature and amounts silver doping were varied. Overall, it was found that films grown at 450°C with 15 weight percent silver doping had best electrochemical results with current densities = 0.3 $mAcm^{-2}$, improved cycling stability, moderate intercalation/deintercalation times of 16/23s and high discharge capacity values of 230 $mAhg^{-1}$. Even though an improvement in electrochemical properties was observed the non-uniformity of films, poor control over film growth and low transmittance were still not resolved.

The move towards a more controlled growth technique was made. Atomic layer deposition outside of the "ALD window" was used for the growth of V_2O_5 films in a more controlled manner and was used very effectively to improve all of the previously mentioned shortcomings. Films were grown for 400 cycles using both a plasma and thermal methods at a range of temperatures with the most suitable found to be at 250°C. Films were found to grow outside of the "ALD window" and have a significant CVD factor hence the growth was referred to as Pulsed-CVD rather than ALD. Oxygen-plasma films had a current density = 0.38 $mAcm^{-2}$; charge density = 55 $mCcm^{-2}$ and also the best electrochromic response of ΔT = 65%, with greatest optical transparency in the bleached state. However, even though cycling stability was reasonable at low cycling

numbers after 500 cycles the current density of the materials was reduced to approximately 40% of its starting value.

Lastly, in a further effort to improve electrochemical properties the implementation of silver doping was carried out. Films were grown to similar growth conditions to those of the Pulsed-CVD with varying percentages of silver. The implementation of silver altered both the surface morphology and the electrochemical properties. Films had a lower deposition rate and demonstrated enhanced electrochemical properties. Oxygen-plasma grown materials, in particular 5% silver doped V_2O_5, exhibited greatest current density of 1 $mAcm^{-2}$ and cycling stability values over a range of 500 cycles.

Silver doped films grown by ALD were found to be best suited for use as a working electrode in lithium ion battery applications but were found to be non suitable for electrochromic applications due to a wavelength shift in the activated state. Pulsed-CVD grown films were found to combine both promising electrochemical and electrochromic properties which would make them more usable for electrochromic window applications.

10.1 Suggestions for future work

Any further work carried out should look into further studying the growth of silver doped films by further experimenting with silver doping concentrations and conducting in-depth studies on its effects on the growth mechanism.

Other dopant metals should be looked into with the possibility of even further improvement of electrochemical properties combined with enhanced electrochromic properties.

The construction of working prototypes of both a V_2O_5-lithium ion battery and an electrochromic window.

Collaboration with other groups developing lithium ion batteries in an effort to utilize and combine the unique properties of V_2O_5 films with other materials and systems.